Computational Methods in Applied Sciences

Paulo Rui Fernandes
Paulo Jorge da Silva Bartolo *Editors*

New Developments in Tissue Engineering and Regeneration

ECCOMAS
European Community on Computational Methods in Applied Sciences

Springer

Computational Methods in Applied Sciences

Volume 51

This series publishes monographs and carefully edited books inspired by the thematic conferences of ECCOMAS, the European Committee on Computational Methods in Applied Sciences. As a consequence, these volumes cover the fields of Mathematical and Computational Methods and Modelling and their applications to major areas such as Fluid Dynamics, Structural Mechanics, Semiconductor Modelling, Electromagnetics and CAD/CAM. Multidisciplinary applications of these fields to critical societal and technological problems encountered in sectors like Aerospace, Car and Ship Industry, Electronics, Energy, Finance, Chemistry, Medicine, Biosciences, Environmental sciences are of particular interest. The intent is to exchange information and to promote the transfer between the research community and industry consistent with the development and applications of computational methods in science and technology.

Book proposals are welcome at
Eugenio Oñate International Center for Numerical
Methods in Engineering (CIMNE)
Technical University of Catalunya (UPC) Edificio C-1, Campus Norte UPC Gran Capitán, s/n08034 Barcelona, Spain
onate@cimne.upc.eduwww.cimne.com
or contact the publisher, Mrs Nathalie Jacobs, nathalie.jacobs@springer.com

Indexed in SCOPUS, Google Scholar and SpringerLink.

More information about this series at http://www.springer.com/series/6899

Paulo Rui Fernandes · Paulo Jorge da Silva Bartolo
Editors

New Developments in Tissue Engineering and Regeneration

Springer

Editors
Paulo Rui Fernandes
IDMEC-IST
Lisboa, Portugal

Paulo Jorge da Silva Bartolo
School of Mechanical, Aerospace and Civil Engineering
The University of Manchester
Manchester, UK

ISSN 1871-3033
Computational Methods in Applied Sciences
ISBN 978-3-030-15370-0 ISBN 978-3-030-15372-4 (eBook)
https://doi.org/10.1007/978-3-030-15372-4

Library of Congress Control Number: 2019934530

This Springer imprint is published by the registered company Springer Nature Switzerland AG
The registered company address is: Gewerbestrasse 11, 6330 Cham, Switzerland

Preface

This book, *New Developments in Tissue Engineering and Regeneration*, is in line with the previous ones from the same editors, *Advances on Modeling in Tissue Engineering* (2011) and *Tissue Engineering: computer modeling, biofabrication and cell behavior* (2014), and it represents a new contribution for the field of Tissue Engineering with a focus on the development of mathematical and computational methods that are quite relevant to understand human tissues as well to model, design, and fabricate optimized and smart scaffolds.

The present book encompasses contributions from recognized researchers in the field, who were keynote speakers in the Fourth International Conference on Tissue Engineering, held in Lisbon in 2015, and covering different aspects of Tissue Engineering.

The book is strongly connected with the conference series of ECCOMAS Thematic Conferences on Tissue Engineering, an event that brings together a considerable number of researchers from all over the world, representing several fields of study related to Tissue Engineering.

The editors are deeply grateful to all the contributing authors. We would also like to thank the European Community on Computational Methods in Applied Sciences (ECCOMAS), the Portuguese Association of Theoretical Applied and Computational Mechanics (APMTAC), and the Portuguese Foundation for Science and Technology (FCT) for supporting the Conference.

Lisboa, Portugal — Paulo Rui Fernandes
Manchester, UK — Paulo Jorge da Silva Bartolo

Contents

Computational Modelling of Wound Healing Insights to Develop New Treatments

M. J. Gómez-Benito, C. Valero, J. M. García-Aznar and E. Javierre

Abstract About 1% of the population will suffer a severe wound during their life. Thus, it is really important to develop new techniques in order to properly treat these injuries due to the high socioeconomically impact they suppose. Skin substitutes and pressure based therapies are currently the most promising techniques to heal these injuries. Nevertheless, we are still far from finding a definitive skin substitute for the treatment of all chronic wounds. As a first step in developing new tissue engineering tools and treatment techniques for wound healing, *in silico* models could help in understanding the mechanisms and factors implicated in wound healing. Here, we review mathematical models of wound healing. These models include different tissue and cell types involved in healing, as well as biochemical and mechanical factors which determine this process. Special attention is paid to the contraction mechanism of cells as an answer to the tissue mechanical state. Other cell processes such as differentiation and proliferation are also included in the models together with extracellular matrix production. The results obtained show the dependency of the success of wound healing on tissue composition and the importance of the different biomechanical and biochemical factors. This could help to individuate the adequate concentration of growth factors to accelerate healing and also the best mechanical properties of the new skin substitute depending on the wound location in the body and

M. J. Gómez-Benito (✉) · C. Valero · J. M. García-Aznar
Multiscale in Mechanical and Biological Engineering (M2BE), Aragón Institute of Engineering Research (I3A), University of Zaragoza, Zaragoza, Spain
e-mail: gomezmj@unizar.es

C. Valero
e-mail: claraval@unizar.es

J. M. García-Aznar
e-mail: jmgaraz@unizar.es

E. Javierre
Centro Universitario de la Defensa, Academia General Militar; Instituto Universitario de investigación en Matemáticas y Aplicaciones (IUMA), Zaragoza, Spain
e-mail: etelvina@unizar.es

P. R. Fernandes and P. J. da Silva Bartolo (eds.), *New Developments in Tissue Engineering and Regeneration*, Computational Methods in Applied Sciences 51,
https://doi.org/10.1007/978-3-030-15372-4_1

its size and shape. Thus, the feedback loop of computational models, experimental works and tissue engineering could help to identify the key features in the design of new treatments to heal severe wounds.

Keywords Wound healing · Mechanobiology · Wound contraction · Skin substitutes

1 Introduction

Skin is the largest organ of the human body. It represents the natural interface between the body and the environment, acting not only as a physical barrier but also as a regulator of water loss. It is part of the immune system, avoiding the entrance of strange particles and pathogens. When skin is injured, it heals through a complex cascade of events aimed at restoring skin integrity. Normally, wounds heal without additional complications in the time curse of a few weeks (to recover the main functionalities of skin). However, when the healing path is altered (by many pathological conditions affecting this process), severe or chronic wounds appear. These severe wounds include pathological scars in which there is an overexpression of collagen (hypertropic scars and keloids), contractures in which there is not enough scar formation, large area wounds such as burns, and chronic wounds such as pressure ulcer. The treatment of these severe wounds represent a high socioeconomical cost. For example, it has been reported that in the year 2000, the treatment of pressure ulcers reached the 4% of the United Kingdom National Health System expenditure [2]. In the same country, in the year 2011, the average cost of a pressure ulcer ranged from £1,214 to £14,108, attending to the severity of the case [9]. It is also important to notice that these injuries also cause considerable pain to the patient, can add months to the hospital stays [9], and in the worst scenarios dramatically reduce the quality of life of the patients. Thus, it is really important from a societal, clinical and economic perspectives to put our efforts in the prevention and reduction of the number of severe wounds and improve, in the range of our possibilities, their treatment.

Serious injuries to the skin do not heal autonomously, and usually they require coverage to repair and restore skin function or other external treatments such as negative pressure wound therapy. Skin replacement is normally done by autologous skin graft of a patient; healthy skin is separated from the donor site and transplanted into the recipient area. However, availability of sufficient healthy skin can limit this treatment, as well as the additional health risks associated with it such as the deformation of the donor-site [39]. Allogenetic, xenogenetic, syngeneic and cadaver skin grafts are also used; nevertheless, they present also problems of availability and add the problem of rejection.

Due to the above mentioned limitations of skin grafts, engineering skin substitutes emerge as a growing area in both clinics and engineering research. However, currently, no skin substitute has provided an outcome similar to an autograft [39]. Some of the problems with existing skin substitutes are the reduced vascularization

and scaring of the graft margins. Moreover, their structure remains to be relatively simple (normal single layer or bilayered), and their three dimensional architecture and mechanical properties are still far from those of skin. This is in part due to the processes employed to fabricate them, being technologically extremely difficult to replicate the way healthy skin appears during embryogenesis and fetal development [54]. In order to improve these treatments it is really important to know the mechanical behavior of healthy skin and the wound, and how they influence the cell mechanosensing capacity. Therefore, the next step in tissue engineering shall be the design of new skin substitutes able to replicate skin and wound mechanical and functional characteristics.

Other treatments for chronic wound include the application of external stimulation. For example, negative pressure wound therapy (NPWT) has been used to promote healing of severe injuries, and it is widely extended in chronic wounds [22]. This treatment is based on the positive effect of mechanical stimulation in the healing of tissues. The positive effect of tension strains has been observed to regenerate other biological tissues such as bone in the distraction osteogenesis process in which the rapid vascularization is a key factor in the development of new bone [47]. Oxygen-based therapies have been explored for the treatment of chronic wound in diabetic patients. In this respect Hyperbaric Oxygen Therapies (HBOT) seek the promotion of healing by the stimuli of the angiogenesis process [12], although the inherent negative effects of this therapy need to be further examined.

Unfortunately, we are still far from developing a definite treatment to heal severe wounds. The traditional approach to develop new therapies has been based on the use of animal models. However, animal experimentation is expensive in economical, social and temporal terms. Also, there is no animal model of skin which completely mimics all the characteristic of human skin [31]. On the other hand, the use of *in silico* models offers a wide (and cheap) spectrum for analyses. Consequently, it is called to play a prominent role in the design of new treatments, due to its intrinsic capacity to isolate single factors [18].

2 Healthy Skin

Skin represents a 6% of the total body weight [56], it has a variable thickness depending on the body location from around 1.5 mm in the sclap to 4 mm in the back. It is a highly organized structure consisting of three main layers: the epidermis, the dermis and the hypodermis.

The most external layer of the skin is the **epidermis** which is continually renewing. It is approximately 75–150 μm in thickness. The epidermis is also divided into five layers. The stratum corneum is the outermost layer of the epidermis which provides a permeability barrier and is mainly composed by a mixture of lipids and an acid mantle important to prevent infections. The other four layers which compose the epidermis are the stratum lucidum, the stratum granulosum, the sratum spinosum and the stratum germinativum which are a second-line epidermal barrier between the

outside and inside of the body [1]. The main epidermal cell types are keratinocytes which represent around 90–95% of the present cells. Keratinocytes are antinflamatory mediators which are part of the immune system. Other cells types in the epidermis include melanocytes responsible of skin pigmentation and protecting against damage of UVR radiation, Langerhans cells which maintain immune homeostasis in skin and represent around 5% of the epidermal cells [50] and Merkel cells mechanosensory cells which participate in touch reception [34].

The epidermis and the dermis are tightly connected through the **basement membrane**. This membrane represent a critical interface which allows cell communication and regulates different cellular activities such as differentiation and apoptosis. It has a structural role, maintains the architecture of the tissues and also provides anchorage for cells migration, macromolecules transit and temporal storage of these macromolecules [36]. The basement membrane is mainly composed by collagen type IV, laminin, proteoglycan and tentactin [6].

The **dermis** is the second skin layer, it is a dense fibroelastic connective tissue of around 1–4 mm thickness. It can also be divided into two layers: the outer one is the papillary dermis which contains disorganized collagen fibers; and the inner one is the reticular dermis, which is formed by organized fibers. The papillary dermis is thinner that the reticular one. The dermis contains much less cells than the epidermis and it is in charge of housing skin's appendages (eccrine and apocrine sweet glands, pilo-sebaceous follicles), nerves, vascular and lymphatic vessels and receptors [56]. The predominant cell population of the dermis is the fibroblast which produces and degrades the extracellular matrix and also contracts it. Other cell populations in the dermis are dendritic dermal cells, macrophages and mast cells which are multifunctional cells of the immune system. The dermis gives structural support and mechanical strength to the skin, and it is also responsible of the nutritional supply. The extracellular matrix of the dermis is composed by different fibers: collagen and elastic fibers [58]. Collagen provides tensile properties to the dermis, being collagen type I the most abundant, however there are also other collagen types (III, V). In addition, elastic fibers gives elasticity to the dermis, which include elastin, fibrillin and microfibrilar components. Finally, the extrafibrilar matrix components of the dermis are proteoglycans which maintain water and ion balance, glycoproteins, water and hyaluronic acid [58].

The third layer, the **hypodermis** (or subcutaneous fat) is composed of loose fatty connective tissue. It serves to fasten the skin to the underlying tissue, it represents an energy reserve for the body and it is also a thermoregulator. The main cell population of the hypodermis is adipocyte.

The collagen fibers of skin are not isotropically oriented [26]. In fact, Langer was the first to observe that the skin is an anisotropic material in the 19th century [26]. He punctured the skin with a circular device and observed that the circular wounds became elliptical in shape when relaxed. Joining the major axes of the ellipses he drew the tension lines of the skin which were named **Langer's lines**. These lines are normally oriented in the direction of the underlying muscles. Later on, the orientation of Langer lines was identified as the preferential orientation of collagen fibers in skin [8, 48], and also it was observed that wounds in the direction of Langer's lines tend

to heal quicker than the ones perpendicular to these lines. Moreover, skin is naturally prestressed [15] which add complexity to its behavior.

The complex multilayered architecture and composition of the skin together with the Langer's lines makes the skin a complex material from a mechanical point of view. Also the variable layer composition and thickness which depends on the individual, body site and age make even more difficult the adoption of a single constitutive model for the healthy skin. Different mechanical models have been adopted to characterize this intrincated mechanical behavior considering its viscoelasticity [27], hyperelasticity [3] and anisotropy [43]. However, the models ranged from the simplest ones which assume the skin as a monolayered linear elastic material, to the most complex which consider skin anisotropy and its multilayered nature [14]. The constitutive model adapted when considering its anisotropy is the same as in other fibered soft tissues [17]. Other characteristics such as the viscoelasticity associated to its multiphasic nature has also be taken into account. Most of the models used for healthy skin are monolayered models; however, recently multilayered models which considered the different behavior of the layer have also be introduced to simulate healthy skin [14].

3 Wound Healing

Wound healing is a dynamical complex organized process which aims at restoring the injured skin. It involves the interplay of different cellular species, extracellular matrix components, biochemical factors such as growth factors and cytokines together with the mechanical environment. The cell-cell and the cell-extracellular matrix interactions are also really important for the success of this process. Wound healing is divided into three phases which are overlapped in time: hemostasis phase, re-epithelization phase and maturation or remodeling phase.

The injury disrupts the tissue and provokes haemorrhage. The first response of the organism to the injury is the formation of a blood clot to reduce blood loss, this is the coagulation or **hemostasis phase**. Mechanical properties of this blood clot are really important for the whole wound healing process, it will serve as a provisional matrix for cell migration. In this phase, platelets play a pivotal role (Table 1) since they reduce blood loss and also release platelet-derived growth factor (PDGF) which will stimulate fibroblast proliferation and chemotaxis [16]. **Inflammation** starts around one hour after the injury, neutrophils migrate to the wound site and remove debris tissue, death cells and bacteria.

In the **proliferative phase** the blood clot is gradually replace by granulation tissue and new blood vessels are developed in the angiogenesis process. Fibroblast and endothelial cells proliferate and migrate to the wound site around three days after the fracture. Endothelial cells start to form new capillarities from existing ones. Fibroblast secrete collagen type I, glycosaminoglycans and proteoglycans which are the main components of the extracellular matrix. This early collagen secretion results in an initial rapid increase in wound strength. Epithelial cells migrate to

Table 1 List of cellular species involved in wound healing

Name	Function	Location	Healing stage/ process	Others
Adipose cells/ Adipocytes	Store energy as fat	Hypodermis		Synthesize several hormones
Endothelial cells	Form new capillaries during angiogenesis	Blood vessels	Epithelialization	Motile cells that migrate to the wound site during the epithelialization stage
Fibroblasts	Synthesize collagen type III Generate contraction forces	Dermis Hypodermis	Epithelialization Contraction	Motile cells that migrate to the wound site during the epithelialization stage
Keratinocytes	Main constituent of the epidermis Form a barrier against environmental damage Modulates the immune system producing anti-inflammatory mediators	Epidermis	Epithelialization	Motile cells that migrate to the wound site during the epithelialization stage
Macrophages	Phagocytosis Eliminate bacteria and dead cells at injured sites	Dermis Hypodermis	Inflammation	Derived from blood monocytes Enter the damaged site through the endothelium of blood vessels Chemotactically attracted to the wound site by cytokines released from damaged cells Part of the immune system
Myofibroblasts	Synthesize collagen type III Generate contraction forces Secrete factors that induce angiogenesis	Dermis	Epithelialization Contraction Angiogenesis	Differentiated fibroblasts Non-motile
Neutrophils	Eliminate bacteria and dead cells at injured sites	Bloodstream	Inflammation	Attracted by inflammation factors Part of the immune system
Platelets	Prevent bleeding forming a plug where there is vascular endothelial damage Blood coagulation	Dermis	Hemostasis	Release PDGF

the wound site and secrete different growth factors such as transforming growth factors α and β (TGF-α, TGF-β) which stimulate wound contraction. Fibroblast and myofibroblast contract the wound reducing its size. Myofibroblasts disappear

after this phase by apoptosis. Nevertheless, the activity of myofibroblasts persists in pathological healing, such as in hypertrophic scars and contractures [21].

Finally, the **remodeling phase** takes place, which could last for years. The collagen type I deposited during the proliferative phase is replaced by collagen type III. This new deposited collagen is reorganized along the Langer's. Once the remodeling phase is concluded, the tensile strength of the scar is about 70% of the tensile strength of the healthy skin about six weeks after injury, which is close to the maximal tensile strength the scar can achieve 75–80% of the healthy skin [29].

All these processes are guided both by biological and mechanical stimulus. The main cellular species involved in healing are summarized in Table 1.

4 Severe Wound Treatments

Different treatments are used when a wound present problems while healing. If the wound is large, it is normally covered by a skin substitute. Even though the autologous skin graft is the preferred technique from a biological point of view, it presents problems of availability and different side effects. Thus, currently the tendency is towards artificial grafts. When the wound is profound, the skin substitute is combined with different pressure therapies in order to accelerate and improve healing.

Skin Scaffolds

Skin substitutes have arisen as a promising technique to treat wounds in which coverage of large areas of skin is required. Indeed, skin substitute engineering is a growing area of research; skin substitutes are widely used in clinics nowadays. In fact, different commercial skin grafts are routinely used in the clinical practice [38].

Artificial skin substitutes provide an immediate protective barrier for the wound. They prevent dehydratation, the entrance of strange particles in the wound (microorganisms and toxins); they also provide an immediate matrix for cell adhesion and revascularization of the wound. As wound healing progresses the scaffolds are integrated in the wound, through the cell migration and vascularization into the skin graft. Sometimes the scaffold is seeded with different cells or growth factor to favor its integration.

Skin substitutes could be classified as dermal, epidermal or dermo-epidermal [53] depending of the area to cover. They could be also biodegradable or non-biodegradable [53]. Regarding their mechanical and structural properties, first skin substitutes (now in the market) were designed to replace healthy skin, they try to mimic the properties of this healthy skin. Nevertheless, there is not a scaffold which provide results comparable to biological skin [38]. Different problems arise in the outcome of wound healing such as poor angiogenesis and scaring of the wound mar-

gins. This is due to the fact that the architecture and composition of the skin scaffolds is much simpler than the one of the healthy skin; for example, skin scaffolds lack of skin appendages (hair follicles, sweat and sebaceous glands) [19] which modify its mechanical properties. These appendages represent discontinuities in the tissues which change skin permeability.

Now the trends go towards skin substitutes which promote wound healing rather than the ones which try to replace skin. Thus, the properties of new scaffolds try to mimic the ones of the wound to allow the different phases of wound healing to happen. Moreover, different cells populations and growth factors are integrated in the new generation scaffolds [66]. Special attention is been paid to the morphology and architecture of the scaffolds at different scales. Since it has been observed that to properly promote regeneration it is really important not only mimic the micro-scale morphology of the ECM of the wound but also its nano-scale morphology [66]. For example a key aspect to promote cell growth is the pore size at different scales. The new research developed to understand cell-cell and cell-ECM interactions [11], have emphasized the need to preserve the properties of the ECM of a normal wound. In this sense, it is also important the use of mixing material better than single materials [10].

Pressure Wound Therapies

Negative pressure wound therapies (NPWT) use a suction device to apply a subatmospheric pressure to the wound, which has been previously filled with a porous foam and sealed with an adhesive. Different interface materials and suction devices have been used since this treatment was first proposed by Morykwas et al. [41].

This treatment is based in mechanotrasduction principles, that is the cells are able to sense the mechanical stimulus and translate it into different biochemical and mechanical signal. This principle was first used to induce regeneration and formation of bone by Ilizarov and Soybelman [23], who first applied traction force in order to generate new bone through distraction osteogenesis. Here, tensile strains are also induced in the wound borders. This deformation stimulates angiogenesis, migration, proliferation and extracellular matrix production. Moreover, the suction removes excess of fluids in the wound. The pressure is applied till the wound is filled by granulation tissue or the wound is prepared for surgery. The level of microdeformation induced in the interface of the wound with the foam dressing depends not only on the applied pressure but also on the foam pore size. In fact, the pore size of the foam is directly related with the amount of granulation tissue formation [20].

The pressure is applied continuously or intermittently. Better results are observed when it is applied intermittently, nevertheless it requieres more care of the patient and it also results in discomfort for the patient [22].

5 Computational Models of Wound Healing

As already mentioned, the healing of a wound involves the coordinated interaction of a wide range of chemical factors and cellular species. Numerous models have tackled the different phases of the healing process, frequently from a continuum point of view. This path was initiated in the early nineties by Sherratt and Murray [51] and Tranquillo and Murray [57], since then it has experienced an increasing attention. First wound healing models were dedicated to the biochemical aspects of the process, mainly focusing on the relation between cellular species and the growth factors that guide the cellular evolution during healing. Sherratt and Murray [51] developed one of the first wound healing models in which they studied the evolution of epidermal cells and a mitosis-regulating growth factor. This model evolved to more complex ones [44, 57] through the inclusion of more cellular species such as fibroblasts and myofibroblasts and the concentration of collagen ECM in the skin. Moreover, these models added the mechanical properties of the skin in order to evaluate the ECM displacement that the skin suffers during wound healing. Most wound healing models that include mechanics are focused on the contraction stage during wound healing [25, 42, 44, 57, 60–65] and one of their main objectives is to quantify the size reduction that the wound suffers during healing. Nevertheless, other models pay attention to other phenomena that occurs during wound healing such as angiogenesis [12, 13, 24, 33, 35, 45, 46, 49, 59, 63, 64]. Most of the angiogenesis works include the oxygen as a main factor in their models together with the influence of angiogenic growth factors.

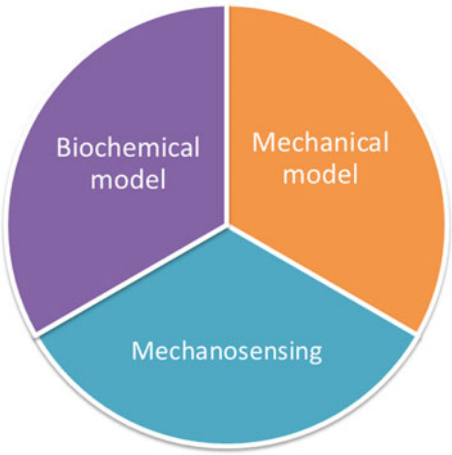

Fig. 1 Scheme of the mechanobiological models. They consist of three main blocks: the biochemical evolution of tissues, the constitutive model of the tissues in which mechanical stimulus is determined and the mechanosensing mechanism of the cells in which the two first block are connected

When the mechanical behavior of skin is included in wound healing models one of the most important aspects is the constitutive material model used to reproduce skin properties. In most wound healing models skin is considered to behave as a viscoelastic material [25, 35, 42, 44, 57, 63–65]. However, it is known that the real behavior of the skin is more complex and in the last years more realistic constitutive material models have been considered. Valero et al. [59, 60] included isotropic hyperelastic skin properties to simulate angiogenesis during wound healing and later added the anisotropic component [62]. In that work, Valero et al. [62] included the effect of fiber anisotropy in three dimensions to reproduce the real collagen fiber network of the skin. Collagen fibers are oriented according to two preferred directions and thus skin behavior is not the same along every direction.

Most of the previous models study wound healing under normal conditions, without assistance. Nevertheless, some models simulate the evolution of wound healing under different therapies that improve or accelerate healing. Lott-Crumpler and Chaudhry [32] analyzed different suture patterns in wounds with complex shapes to find the best resulting stress distribution. Buganza Tepole et al. [7] also used stress analysis to predict healing during the application of skin flaps in reconstructive surgery. Flegg et al. [12, 13] studied the effect of hyperbaric oxygen therapy in wound healing paying attention to the angiogenesis process. They studied the appearance of capillary tips and the evolution of blood vessels according to the oxygen supply.

General Framework of Continuum Wound Healing Models

The pioneering models, and the more recent ones, are built upon a set of coupled diffusion-convection-reaction equations, one for each species in the model. The considered species represent the averaged values of their biological counterpart, such as endothelial cells, fibroblasts or myofibroblast densities (i.e. number of cells per unit of volume), extracellular matrix fibers such as collagen (in its different types), fibrin and cytokines and growth factor concentrations (i.e. mass per unit of volume) such as VEGF, TFG-β. The system of equations to be solved is frequently non-linear (to cope with the intricate communication between cells, cell-receptors and mechano-biological cues) and strongly coupled (to cope with the cascade of events that lead the activity of a certain cellular species triggered by precursor factors). The governing equations ruling these models are formulated attending to the conservation of cellular and chemical species and the conservation of tissue momentum, together with the mechanosensing mechanism of the cell (Fig. 1). This mechanosensing of the cells is represented through their capacity to sense their mechanical environment and translate it to regulate the forces that they exert on the tissue and also to regulate other biological processes such us differentiation and extracellular matrix production. The use of non-coupled models between biochemical and mechanical processes allow to deal with the different time scales at which biochemical and mechanical event occurs at the wound site.

Thus, if we consider a system with n cellular or chemical species c_i (with $i = 1, \ldots, n$), the conservation of the first one, c_1, can be formulated in general terms as

$$\frac{\partial c_1}{\partial t} + \nabla \cdot \mathbf{J}_1(t, \mathbf{x}, c_1, \ldots, c_n, \mathbf{u}) = f_1(t, \mathbf{x}, c_1, \ldots, c_n, \mathbf{u}, \boldsymbol{\sigma}) \tag{1}$$

where t denotes the temporal variable, $\mathbf{x}$ the spatial coordinate, $\mathbf{J}_1$ denotes the net flux of species c_1 and f_1 denotes the net production of species c_1. In this general framework, the flux term $\mathbf{J}_1$ may account for factors such as random migration, biased migration (chemotaxis, haptotaxis and/or durotaxis) and the passive drag of species due to the deformation of the host tissue. This can be mathematically formulated as

$$\begin{aligned}\mathbf{J}_1(t, \mathbf{x}, c_1, \ldots, c_n, \mathbf{u}, \boldsymbol{\sigma}) = &- D_1 \nabla c_1 + \frac{a_{12}}{(A_{12} + c_2)^2} c_1 \nabla c_2 + a_{13} c_1 \nabla c_3 \\ &+ a_{1,cell} \nabla \cdot \boldsymbol{\sigma}_{cell} + c_1 \frac{\partial \mathbf{u}}{\partial t},\end{aligned} \tag{2}$$

where the first term of Eq. (2) accounts for the random migration (or diffusion) of c_1, the second and third terms account for the biased migration upwards a chemotactic factor c_2 (chemotaxis) and a ECM fiber density c_3 (haptotaxis), the fourth term accounts for the biased migration towards stiffer or strained regions (durotaxis/tensotaxis), and the last term accounts for the passive drag of substance c_1 due to the extracellular matrix deformation (represented here by the displacement field $\mathbf{u}$ and the subsequent velocity field $\frac{\partial \mathbf{u}}{\partial t}$). The chemotactic sensitivity function $\frac{a_{12}}{(A_{12}+c_2)^2}$ is taken from Olsen et al. [44] based on Michaelis-Menten reaction kinetics between the chemotactic factor and the receptors at the cell surface [52]. The haptotactic term, $a_{13} c_1 \nabla c_3$, is taken from Tao and Winkler [55], whereas the durotaxis term, $a_{1,cell} \nabla \cdot \boldsymbol{\sigma}_{cell}$, is taken from Moreo et al. [40]. Note as well that the durotaxis term, $a_{1,cell} \nabla \cdot \boldsymbol{\sigma}_{cell}$, includes implicitly the cell density, c_1, through the definition of the cell induced stress, $\boldsymbol{\sigma}_{cell}$, as shall be detailed below. In both cases the sensitivity coefficient (a_{13} and $a_{1,cell}$) is considered constant.

Similarly, the net production of species c_1 can present an expression of the form:

$$\begin{aligned}f_1(t, x, c_1, \ldots, c_n, \mathbf{u}, \boldsymbol{\sigma}) = &\left(r_1 + \frac{r_{12,max} c_2}{C_{12} + c_2}\right) c_1 \left(1 - \frac{c_1}{K_1}\right) - \frac{k_{14} c_2}{K_{14} + c_2} \theta^+ c_1 \\ &+ k_{41} c_4.\end{aligned} \tag{3}$$

This net production expression takes into account the proliferation of species c_1 and the differentiation of species c_1 into species c_4, both mechanisms upregulated by the mitotic factor c_2 (through a saturation-like kinetics of the form $\frac{K_{14} c_2}{K_{14}+c_2}$, where K_{14} denotes the maximum stimulus prompt by the cytokine c_2 and K_{14} regulates the influence of cytokine). Moreover, the differentiation from c_1 to c_4 includes as well the influence of tissue stiffness and cell stretch (Fig. 2) through the term $\theta^+ = \max(\theta, 0)$

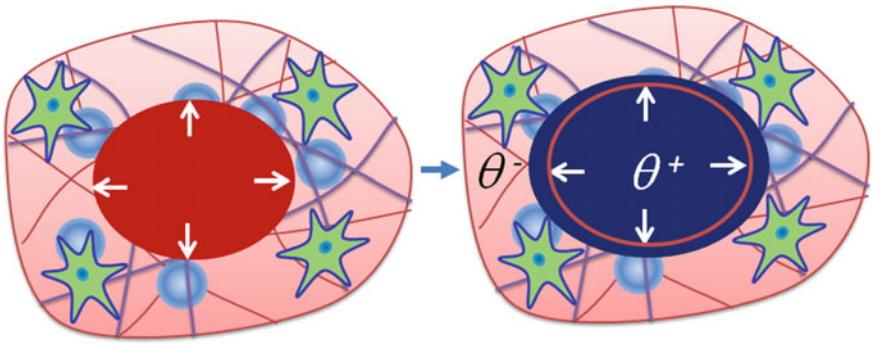

Fig. 2 Initial mechanical environment of the injured site. After the injury takes place it is distracted due to the prestresses of the healthy skin that make volumetric strains in the wound to be positive and negative in the healthy skin. This distribution of stresses will induce differentiation of fibroblast into myofibroblasts inside the wound

(where $\theta = \nabla \cdot \mathbf{u}$) [60]. Finally, the last term on Eq. (3) accounts from the backward differentiation from species c_4 to species c_1, modeled through a linear kinetics.

The conservation of tissue momentum can be written in general form as

$$\nabla \cdot (\boldsymbol{\sigma}_{ecm} + \boldsymbol{\sigma}_{cell}) = \mathbf{f}_{ext}, \tag{4}$$

where $\boldsymbol{\sigma}_{ecm}$ denotes the host tissue constitutive material law (which can chose among elastic, viscoelastic, hyperelastic, with or without anysotropic effects [62]), $\boldsymbol{\sigma}_{cell}$ denotes the cell-induced stresses and $\mathbf{f}_{ext}$ the external forces acting on tissue. Normally, the external forces are assumed to be linear with the tissue stiffness, modeled as the product of cell density and extracellular matrix fibers density. The cell-induced stresses $\boldsymbol{\sigma}_{cell}$ is more accurately represented as the product of the net force per a single cell and the cellular densities exerting traction forces, as for instance

$$\boldsymbol{\sigma}_{cell} = p_{cell}(\theta) c_1 \mathbf{I} \tag{5}$$

where an isotropic behavior has been assumed, governed by the cellular function $p_{cell}(\theta)$ that copes with the regulation of the traction force by the tissue stiffness through the cellular volumetric deformation θ [60].

With this model different results could be obtained such as the temporal evolution of the different cellular and chemical species and the extracellular matrix mechanical environment (Fig. 3). Models as the above-described have been extensively used to analyze the course of the healing process, and in particular, to unveil patterns leading to unsuccessful healing. Most attention has been driven to hypoxic wounds, where an insufficient oxygen supply impedes the progress of healing. In this line, Flegg et al. [12] used a biochemical model of angiogenesis to investigate the impact of oxygen based therapies. More extensive models of angiogenesis include the effect of the tissue mechanics, such as Schugart et al. [49] and Xue et al. [65]. Menon et

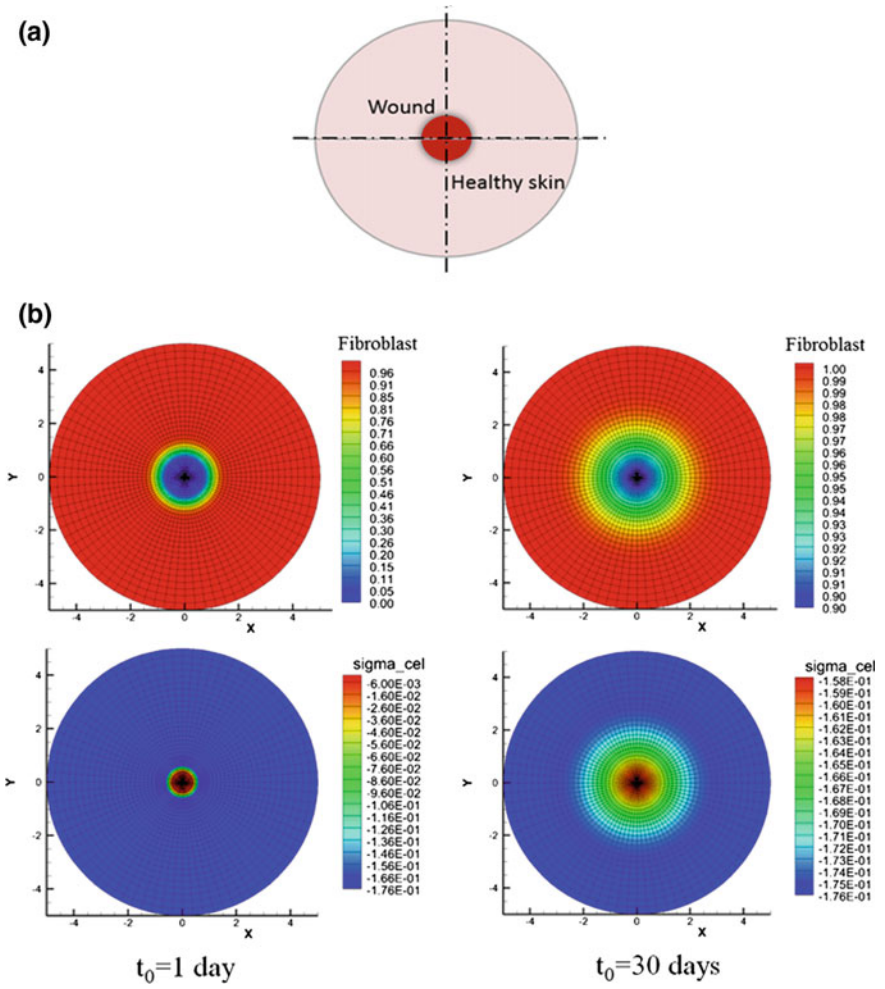

Fig. 3 **a** Superficial circular wound simulated in which both wound and surrounding healthy skin are included; **b** evolution of fibroblast inside the wound and volumetric stress (MPa). The model proposed in [59] has been used in the simulation. Note the different scales used in the contour legends at the begin and end of the simulation

al. [37] used a biochemical model of wound closure to study the effect of prolonged inflammation on the healing kinetics. Purely mechanical models have been also considered to design improved cushions for preventing pressure ulcers in patients with reduced motility [30].

6 Discussion and Conclusions

In silico models represent a powerful tool to understand the wound healing process and how different factors influence its outcome. Note that they offer a straightforward framework to isolate not only the mechanical variables but also the biochemical ones. Besides, physically based models set a step forward in the understanding of different phenomena such as the differentiation of fibroblast into myofibroblast and the contraction kinematics [60]. Thus, *in silico* models provide a cheap platform on which elucidate the main variables which will be important to produce future skin substitutes which better mimic the morphology of the wound and skin. Moreover, they add the possibility of performing patient and site specific simulations in order to determine the viability of different treatments before their application; as well as the opportunity to simulate both physiological and pathological states.

Some ideas arise when analyzing the results of computational models of wound healing, regarding the design of new treatments. First, the design of patient specific skin substitutes could aid to reduce scarring by controlling tissue contraction, in this respect, wound morphology could be naturally incorporated. Secondly, the skin scaffold need to adequately mimic the material properties of the substituted tissue (such as stiffness evolution, anisotropy, prestress and Langer's lines). Similarly, the use of negative pressure therapies is conditioned to a better knowledge of the pressure level to apply. Thirdly, it is equally important to take into account the interaction of cells with the skin substitutes by mechanosensing and how cell-cell interactions are modified when the tissue properties are not the same as the wound or the healthy tissues. And last but not least, a deeper knowledge of the intricate governing the healing cascade need to be gained before a definitive wound healing treatment for severe wounds can be found. As far as we know, the complete aetiology of this injuries is not completely understand, and, despite the efforts made to treat and prevent severe wounds their prevalence rate remains still high.

The design of skin substitutes has been traditionally made with passive and biologically compatible scaffolds which replace healthy skin. However, the new trend goes towards skin substitutes which mimic the mechanical and architectural properties of the wound [39] in order to actively promote healing through mechanotransduction. Cells detect, react and adapt to the mechanical stimulus that they feel, which is undoubtedly influenced by the mechanical properties of the skin and the wound along the healing process. This aspect should be considered when designing new treatments. It may be important to properly reproduce the mechanical environment in each time point of the healing process in order to better reproduce the environment which better induce cell activity and produce no alterations in cell mechanotransduction when compared with normal wound healing. This will be essential to understand mechanotransduction of cells and how it could be altered due to different extracellular matrix environments such as the ones of skin substitutes. *In silico* models could

also be used to determine the outcome of each skin substitute before implantation. Moreover, different new factors should be incorporated in *in silico* models.

The importance of considering the different spatial and temporal scales that characterize the healing process has been proven experimentally through the study of various treatments [11, 20, 66]. It is necessary to go down until the nanoscale to understand the cell-to-cell and cell-to-ECM interactions that guide the healing process. Different attempts have been made to reproduce this interaction such as the proposal of cellular function laws based on experimental evidences [60]. However, in order to properly determine the interaction of the cell and extracellular matrix, new models of wound healing should incorporate the nanoscale implicitly. Recently, several models of single cell events such as migration of cells in two [40] and three dimensions [4, 5] have been developed. However, to completely understand the aetiology of severe wounds (and consequently search for the most suitable treatment) it is necessary to incorporate all the involved scales in order to unveil the individual role of each factor at each scale and the interactions among scales. Moreover, as far as we know, the topology and internal architecture of the wounds has not been incorporated in the models, even though they guide different events of healing [20, 66].

Additionally, it would be also very important to understand the way skin develops during embryogenesis and fetal growth. Computational models focused on these early phases could also aid in understanding the the healing process, as well as exploiting their complementary nature respect to in vivo and in vitro experiments an their intrinsic capability of individuating the role of mechanics on it. This would guide the design of more complex structures for skin scaffolds [38] as well as the analisys of more favorable mechanical environments for skin development and healing. The absence of scaring in fetal wounds [28] could be considered as the ideal situation to be mimicked.

Finally, it should be noticed that a wide range of approaches have been developed to study wound healing, both from experimental and computational perspectives. However, these approaches are closed to the one specific aspect under consideration. It has been proved for other biological tissues [18] that the interrelationship among the different events can have and important role in the improvement of healing and consequently the design of new treatments. Therefore, it seems more convenient nowadays to exploit the specific knowledge in the last decades in a joint and global model of the healing process.

Acknowledgements This research was supported by the European Research Council (ERC) through the project ERC-2012-StG 306751 and the Spanish Ministry of Economy and Competitiveness through the project DPI2012-32880 (project partly founded by the European Development Fund).

References

1. Baroni A, Buommino E, De Gregorio V, Ruocco E, Ruocco V, Wolf R (2012) Structure and function of the epidermis related to barrier properties. Clin Dermatol 30(3):257–262. https://doi.org/10.1016/j.clindermatol.2011.08.007
2. Bennett G, Dealey C, Posnett J (2004) The cost of pressure ulcers in the UK. Age Ageing 33(3):230–235. https://doi.org/10.1093/ageing/afh086
3. Bischoff JE, Arruda EM, Grosh K (2000) Finite element modeling of human skin using an isotropic, nonlinear elastic constitutive model. J Biomech 33(6):645–652. https://doi.org/10.1016/S0021-9290(00)00018-X
4. Borau C, Kamm RD, García-Aznar JM (2011) Mechano-sensing and cell migration: a 3D model approach. Phys Biol 8(6):066008
5. Borau C, Polacheck WJ, Kamm RD, García-Aznar JM (2014) Probabilistic Voxel-FE model for single cell motility in 3D. In Silico Cell Tissue Sci 1:2. https://doi.org/10.1186/2196-050X-1-2
6. Bosman F, Cleutjens J, Beek C, Havenith M (1989) Basement membrane heterogeneity. Histochem J 21(11):629–633. https://doi.org/10.1007/BF01002481
7. Buganza Tepole A, Gosain AK, Kuhl E (2014) Computational modeling of skin: using stress profiles as predictor for tissue necrosis in reconstructive surgery. Comput Struct 143:32–39
8. Cox HT (1941) The cleavage lines of the skin. Br J Surg 29(114):234–240. https://doi.org/10.1002/bjs.18002911408
9. Dealey C, Posnett J, Walker A (2012) The cost of pressure ulcers in the United Kingdom. J Wound Care 21(6):261–266. https://doi.org/10.12968/jowc.2012.21.6.261
10. Edalat F, Sheu I, Manoucheri S, Khademhosseini A (2012) Material strategies for creating artificial cell-instructive niches. Curr Opin Biotechnol 23(5):820–825. https://doi.org/10.1016/j.copbio.2012.05.007
11. Ehrlich HP (2013) A snapshot of direct cell-cell communications in wound healing and scarring. Adv Wound Care 2(4):113–121. https://doi.org/10.1089/wound.2012.0414
12. Flegg JA, McElwain DLS, Byrne HM, Turner IW (2009) A three species model to simulate application of hyperbaric oxygen therapy to chronic wounds. Plos Comput Biol 5(7):e1000451
13. Flegg JA, Byrne HM, McElwain LS (2010) Mathematical model of hyperbaric oxygen therapy applied to chronic diabetic wounds. Bull Math Biol 72(7):1867–1891
14. Flynn C, McCormack BAO (2010) Simulating the wrinkling and aging of skin with a multi-layer finite element model. J Biomech 43(3):442–448. https://doi.org/10.1016/j.jbiomech.2009.10.007
15. Flynn C, Taberner A, Nielsen P (2011) Modeling the mechanical response of in vivo human skin under a rich set of deformations. Ann Biomed Eng 39(7):1935–1946. https://doi.org/10.1007/s10439-011-0292-7
16. Ganapathy N, Venkataraman SS, Daniel R, Aravind RJ, Kumarakrishnan VB (2012) Molecular biology of wound healing. J Pharm Bioallied Sci 4(Suppl 2):S334–S337. https://doi.org/10.4103/0975-7406.100294
17. Gasser TC, Ogden RW, Holzapfel GA (2006) Hyperelastic modelling of arterial layers with distributed collagen fibre orientations. J R Soc Interface 3(6):15–35. https://doi.org/10.1098/rsif.2005.0073
18. Gomez-Benito MJ, Gonzalez-Torres LA, Reina-Romo E, Grasa J, Seral B, Garcia-Aznar JM (2011) Influence of high-frequency cyclical stimulation on the bone fracture-healing process: mathematical and experimental models. Phil Trans R Soc A 369:4278–4294
19. Groeber F, Holeiter M, Hampel M, Hinderer S, Schenke-Layland K (2011) Skin tissue engineering in vivo and in vitro applications. Adv Drug Deliv Rev 63(45):352–366. https://doi.org/10.1016/j.addr.2011.01.005
20. Heit YI, Dastouri P, Helm DL, Pietramaggiori G, Younan G, Erba P, Mnster S, Orgill DP, Scherer SS (2012) Foam pore size is a critical interface parameter of suction-based wound healing devices. Plast Reconstr Surg 129(3):589–597. https://doi.org/10.1097/PRS.0b013e3182402c89

21. Hinz B (2006) Formation and function of the myofibroblast during tissue repair. J Invest Dermatol 127(3):526–537
22. Huang C, Leavitt T, Bayer LR, Orgill DP (2014) Effect of negative pressure wound therapy on wound healing. Curr Probl Surg 51(7):301–331. https://doi.org/10.1067/j.cpsurg.2014.04.001
23. Ilizarov G, Soybelman L (1969) Some clinical and experimental data concerning lengthening of lower extremities. Exp Khir Arrestar 14:27
24. Javierre E, Vermolen FJ, Vuik C, van der Zwaag S (2008) Numerical modelling of epidermal wound healing. In: Numerical Mathematics and Advanced Applications, pp. 83–90. Springer-Verlag Berlin, Berlin; Heidelberg Platz 3, D-14197 Berlin, Germany
25. Javierre E, Moreo P, Doblare M, Garcia-Aznar JM (2009) Numerical modeling of a mechano-chemical theory for wound contraction analysis. Int J Solids Struct 46(20):3597–3606
26. Langer K (1861) Zur anatomie und physiologie der haut. ber die spaltbarkeit der cutis. Sitzungsbericht der Mathematisch-naturwissenschaftlichen Classe der Wiener Kaiserlichen Academie der Wissenschaften Abt 44
27. Lanir Y, Fung YC (1974) Two-dimensional mechanical properties of rabbit skin II. experimental results. J Biomech 7(2):171–182. https://doi.org/10.1016/0021-9290(74)90058-X
28. Leung A, Crombleholme TM, Keswani SG (2012) Fetal wound healing: implications for minimal scar formation. Curr Opin Pediatr 24(3):371–378. https://doi.org/10.1097/MOP.0b013e3283535790
29. Levenson SM, Geever EF, Crowley LV, Oates JF, Berard CW, Rosen H (1965) Healing of rat skin wounds. Ann Surg 161(2):293–308
30. Levy A, Kopplin K, Gefen A (2013) Simulations of skin and subcutaneous tissue loading in the buttocks while regaining weight-bearing after a push-up in wheelchair users. J Mech Behav Biomed Mater 28:436–447. https://doi.org/10.1016/j.jmbbm.2013.04.015
31. Lindblad WJ (2008) Considerations for selecting the correct animal model for dermal wound-healing studies. J Biomater Sci Polym Ed 19(8):1087–1096. https://doi.org/10.1163/156856208784909390
32. Lott-Crumpler DA, Chaudhry HR (2001) Optimal patterns for suturing wounds of complex shapes to foster healing. J Biomech 34(1):51–58
33. Maggelakis S (2003) A mathematical model of tissue replacement during epidermal wound healing. Appl Math Model 27(3):189–196
34. Maksimovic S, Nakatani M, Baba Y, Nelson AM, Marshall KL, Wellnitz SA, Firozi P, Woo SH, Ranade S, Patapoutian A, Lumpkin EA (2014) Epidermal merkel cells are mechanosensory cells that tune mammalian touch receptors. Nature 509(7502):617–621. https://doi.org/10.1038/nature13250
35. Manoussaki D (2003) A mechanochemical model of angiogenesis and vasculogenesis. Esaim-Math Model Numer Anal (Modelisation Mathematique Et Analyse Numerique) 37(4):581–599
36. Marinkovich MP, Keene DR, Rimberg CS, Burgeson RE (1993) Cellular origin of the dermal-epidermal basement membrane. Dev Dyn 197(4):255–267. https://doi.org/10.1002/aja.1001970404
37. Menon SN, Flegg JA, McCue SW, Schugart RC, Dawson RA, McElwain DLS (2012) Modelling the interaction of keratinocytes and fibroblasts during normal and abnormal wound healing processes. Proc R Soc Lond B Biol Sci 279(1741):3329–3338. https://doi.org/10.1098/rspb.2012.0319
38. Metcalfe AD, Ferguson MWJ (2007) Bioengineering skin using mechanisms of regeneration and repair. Biomaterials 28(34):5100–5113. https://doi.org/10.1016/j.biomaterials.2007.07.031
39. Metcalfe AD, Ferguson MWJ (2007) Tissue engineering of replacement skin: the crossroads of biomaterials, wound healing, embryonic development, stem cells and regeneration. J R Soc Interface 4(14):413–437. https://doi.org/10.1098/rsif.2006.0179
40. Moreo P, García-Aznar JM, Doblaré M (2008) Modeling mechanosensing and its effect on the migration and proliferation of adherent cells. Acta Biomater 4(3):613–621
41. Morykwas MJ, Argenta LC, Shelton-Brown EI, McGuirt W (1997) Vacuum-assisted closure: a new method for wound control and treatment: animal studies and basic foundation. Ann Plast Surg 38(6):553–562

42. Murphy KE, Hall CL, McCue SW, McElwain DLS (2011) A two-compartment mechanochemical model of the roles of transforming growth factor β and tissue tension in dermal wound healing. J Theor Biol 272(1):145–159
43. Ní Annaidh A, Bruyère K, Destrade M, Gilchrist MD, Otténio M (2012) Characterization of the anisotropic mechanical properties of excised human skin. J Mech Behav Biomed Mater 5(1):139–148. https://doi.org/10.1016/j.jmbbm.2011.08.016
44. Olsen L, Sherratt JA, Maini PK (1995) A mechanochemical model for adult dermal wound contraction and the permanence of the contracted tissue displacement profile. J Theor Biol 177(2):113–128
45. Pettet G, Byrne H, Mcelwain D, Norbury J (1996) A model of wound-healing angiogenesis in soft tissue. Math Biosci 136(1):35–63
46. Pettet G, Chaplain M, McElwain D, Byrne H (1996) On the role of angiogenesis in wound healing RID A-5355-2010. Proc R Soc Lond Ser B Biol Sci 263(1376):1487–1493
47. Reina-Romo E, Gómez-Benito MJ, Domínguez J, García-Aznar JM (2012) A lattice-based approach to model distraction osteogenesis. J Biomech 45(16):2736–2742. https://doi.org/10.1016/j.jbiomech.2012.09.004
48. Ridge MD, Wright V (1966) The directional effects of skin. J Investig Dermatol 46(4):341–346
49. Schugart RC, Friedman A, Zhao R, Sen CK (2008) Wound angiogenesis as a function of tissue oxygen tension: a mathematical model. Proc Natl Acad Sci U S A 105(7):2628–2633
50. Seneschal J, Clark R, Gehad A, Baecher-Allan C, Kupper T (2012) Human epidermal langerhans cells maintain immune homeostasis in skin by activating skin resident regulatory t cells. Immunity 36(5):873–884. https://doi.org/10.1016/j.immuni.2012.03.018
51. Sherratt J, Murray J (1990) Models of epidermal wound-healing. Proc R Soc B Biol Sci 241(1300):29–36
52. Sherratt JA, Sage EH, Murray JD (1993) Chemical control of eukaryotic cell movement: a new model. J Theor Biol 162(1):23–40. https://doi.org/10.1006/jtbi.1993.1074
53. Shevchenko RV, James SL, James SE (2010) A review of tissue-engineered skin bioconstructs available for skin reconstruction. J R Soc Interface 7(43):229–258. https://doi.org/10.1098/rsif.2009.0403
54. Smith LT, Holbrook KA (1986) Embryogenesis of the dermis in human skin. Pediatr Dermatol 3(4):271–280. https://doi.org/10.1111/j.1525-1470.1986.tb00525.x
55. Tao Y, Winkler M (2011) A chemotaxis-haptotaxis model: the roles of nonlinear diffusion and logistic source. SIAM J Math Anal 43(2):685–704
56. Tobin DJ (2006) Biochemistry of human skin-our brain on the outside. Chem Soc Rev 35(1):52–67. https://doi.org/10.1039/B505793K
57. Tranquillo R, Murray J (1992) Continuum model of Fibroblast-Driven wound contraction—inflammation-mediation. J Theor Biol 158(2):135
58. Uitto J, Olsen DR, Fazio MJ (1989) Extracellular matrix of the skin: 50 years of progress. J Invest Dermatol 92(4s):61S–77S
59. Valero C, Javierre E, García-Aznar JM, Gómez-Benito MJ (2013) Numerical modelling of the angiogenesis process in wound contraction. Biomech Model Mechanobiol 12(2):349–360. https://doi.org/10.1007/s10237-012-0403-x
60. Valero C, Javierre E, García-Aznar JM, Gómez-Benito MJ (2014) A cell-regulatory mechanism involving feedback between contraction and tissue formation guides wound healing progression. PLoS ONE 9(3):e92774. https://doi.org/10.1371/journal.pone.0092774
61. Valero C, Javierre E, García-Aznar JM, Gómez-Benito MJ (2014) Nonlinear finite element simulations of injuries with free boundaries: Application to surgical wounds. Int J Numer Methods Biomed Eng 30(6):616–633. https://doi.org/10.1002/cnm.2621
62. Valero C, Javierre E, García-Aznar JM, Gómez-Benito MJ, Menzel A (2015) Modeling of anisotropic wound healing. J Mech Phys Solids 79:80–91. https://doi.org/10.1016/j.jmps.2015.03.009
63. Vermolen FJ, Javierre E (2010) Computer simulations from a finite-element model for wound contraction and closure. J Tissue Viability 19(2):43–53

64. Vermolen FJ, Javierre E (2012) A finite-element model for healing of cutaneous wounds combining contraction, angiogenesis and closure. J Math Biol 65(5):967–996
65. Xue C, Friedman A, Sen CK (2009) A mathematical model of ischemic cutaneous wounds. Proc Natl Acad Sci U S A 106(39):16782–16787
66. Yildirimer L, Thanh NTK, Seifalian AM (2012) Skin regeneration scaffolds: a multimodal bottom-up approach. Trends Biotechnol 30(12):638–648. https://doi.org/10.1016/j.tibtech.2012.08.004

Traction Force Microscopy in Differentiating Cells

Shada Abuhattum, Amit Gefen and Daphne Weihs

Abstract This chapter provides an overview of the traction force microscopy method used to measure forces applied by cells on substrates under different culture conditions and particularly, as reviewed here, during differentiation. Different relevant mathematical and computational theories for traction measurement are reviewed here, and are being compared based on pros and cons, and implementations in experimental setups. Furthermore, we summarize the literature which reports the effects of the mechanical environment on the differentiation and commitment of stem cells, as relevant to traction force microscopy work. We conclude by focusing on an example application, where we describe changes in the mechanical forces applied by preadipocytes onto a soft (gel) substrate during their differentiation.

Keywords Traction force microscopy · Stem cells · Adipogenesis · Mechanobiology

1 Introduction

In this book chapter we emphasize the importance of cell force measurements as a link to the intracellular processes. We detail the different approaches for measuring forces exerted by cells that were developed over the last few decades. This chapter focuses on employing thick elastic substrates for measuring traction forces where the theory of elasticity can be applied. Fluorescent beads are embedded in this substrate and their location changes when cells apply forces. We present three different approaches for extracting the traction forces from the displacements of the beads. The comparison between the approaches allows to understand the advantages and disadvantages of

S. Abuhattum · D. Weihs (✉)
Faculty of Biomedical Engineering, Technion-Israel Institute of Technology, 3200003 Haifa, Israel
e-mail: daphnew@bm.technion.ac.il

A. Gefen
Department of Biomedical Engineering, Tel Aviv University, 6997801 Tel Aviv, Israel

P. R. Fernandes and P. J. da Silva Bartolo (eds.), *New Developments in Tissue Engineering and Regeneration*, Computational Methods in Applied Sciences 51,
https://doi.org/10.1007/978-3-030-15372-4_2

each method and to correctly choose the suitable method for a given experimental setup. In addition, this chapter will review selected studies conducted on stem cells and committed cells. We show that stem cells can be affected by the stiffness of the substrate; the same stem cells can commit to different lineages when the substrate stiffness is changed from soft to rigid. Finally, we describe changes in the forces applied by preadipocytes during the process of differentiation. Understanding the mechanotransduction and mechanical properties of differentiating cells can reveal new approaches for tissue engineering and regeneration.

2 Cell Cytoskeleton and Force Generation

A cell applies mechanical forces in many biological processes such as organogenesis, wound healing, inflammation, angiogenesis and metastasis. During these processes cells migrate, differentiate, and proliferate. To do this, cells must attach to and spread on a substrate where they generate internal forces through their cytoskeleton and transmit them to the substrate [1]. Thus, evaluating cell-matrix interaction is important for understanding these cell-scale processes.

Rather than spatially organize the cell content, the cytoskeleton connect the cell physically and biochemically to the external environment. It also generates coordinated forces to enable migration and morphology changes of the cell [2]. The cytoskeleton includes three different types of bio-polymer protein networks: actin, microtubules, and intermediate filaments. The actin, which is mainly located near the membrane, is the most dynamic component. It plays a key role in the interaction of the cell with the extracellular matrix [3]. The microtubules surround the cytoplasm and connect the nucleus to the plasma membrane. They have an essential role in motility, division, morphogenesis and organization of the cell and in organelle transport [4]. The intermediate filaments are found between the microtubules and the actin. They are less dynamic, and have a major role in absorbing mechanical stresses [5, 6].

The cytoskeleton is connected to the external environment through focal adhesion (FA) assemblies. Thus, when the cell adheres to a substrate or extracellular matrix (ECM) the FAs are formed to allow force generation and mechanical transduction [7]. The actin cytoskeleton generates traction forces through two main components, the actomyosin stress fibers that generate tension which contracts the cell body [8]; and the actin that polymerizes to form protrusion for facilitating cell migration [9]. Accordingly, FAs transmit mechanical signals from and to the cytoskeleton, and by that, plays a critical role in the cell biological processes. Therefore, measuring these traction forces had been used as a main approach to understand inner cell dynamics.

3 Cell Traction Force Measurements

The traction force microscopy (TFM) method is widely used for measuring the forces applied by cells. It has been improved and customized substantially over the

past few years to allow its implementation in different cell systems and in 2 or 3 dimensions. However, inferring the applied traction forces from the dynamics of the substrate is commonly shared for all TFM approaches [10]. For this purpose, the cells are adhered or embedded in elastic substrates that deform when cell-traction is applied and through these deformations forces are calculated. Early attempts showed a contractile ability for human foreskin fibroblasts. The fibroblasts were mixed with rat tail collagen solution; once the collagen was polymerized it formed a disk with defined diameter. The embedded cells contracted and changed the diameter of the disk [11]. This attempt was later developed to measure the contractile forces of the embedded cells, by relating the change in diameter to the gel characteristics [12]. This method succeeded to quantify the contractile forces for all the cells embedded in the gel but could not separate the calculations for individual cells.

For single cell force measurements, thin silicone membranes were introduced. In this technique, cells that were cultured on the membranes generated traction forces and created wrinkles on the membrane [13]. Measurements of the forces were done by reversing the wrinkles with a flexible needle [14]. However, no computational method for force measurement was available due to the non-linearity of the wrinkling problem. Therefore, the thin silicone membranes were replaced in some latter studies by thick polyacrylamide gels (PAM) that deformed slightly, but did not form wrinkles when cells applied forces [15, 16]. The PAM gels contained embedded markers and their movement under cell-applied forces was tracked and analyzed to yield the displacement field resulted by the tractions. In most cases, the gel was a continuous substrate that deformed, and the traction forces were calculated by solving the inverse problem of the elasticity theory [17, 18]. In other studies, a different approach was adopted—an array of cantilever beams which was used as a discontinuous substrate [19]. The cantilevers each bend when the cells apply forces, and traction forces were calculated from the beam calibration for a pre-defined force-deflection relation. This allowed calculation of traction forces applied by cells in one direction, but did not allow localized measurements over the entire cell's spreading area. To solve that, recent studies have used pillar arrays where each pillar is a local strain gauge [17, 20]. By changing the material properties or length of these poly(dimethylsiloxane) (PDMS) pillars, the stiffness of the array can be adjusted. The forces are thereby measured in each direction and over the contact surface of the cell.

Both discrete PDMS pillars and continuous PAM gels are used for cell traction measurements. A pillar-based approach allows rapid measurements with simple calculations of the traction forces that cells apply. Thus, this method is often being used to test drug effects on cells. However, the pillars restrict the area of cell adhesion and may result in substantially different forces than on flat unconstrained substrates. Accordingly, tractions measured on a continuous thick substrate can better describe in vivo processes.

3.1 Cell Traction Force Microscopy and Analysis

In this section we will focus on thick PAM gels to describe the different approaches used for acquiring images and calculating traction forces from the displacement field of the markers.

The different approaches for traction analysis share the same experimental setup but differ in the displacement field and traction force calculations [1]. The PAM gel is prepared by mixing acrylamide, bis-acrylamide and fluorescent beads. In some studies the fluorescent beads are brought to the upper surface of the gel by centrifuging the gels during the gelation process [17] or by reducing the polymerization rate and turning the gel upside down [15]. The gels are then coated with a substrate such as collagen type I to facilitate better adherence of the cells. The desired locations are saved and photographs of the fluorescent beads are captured once with the cells attached and a second time after trypsinization (where cells are removed) to have the reference image of the beads location without traction forces.

After acquiring the images the displacements of the beads are calculated. There are three main methods for calculating the displacements: The Dembo and Wang's (DW) method [15, 21], the Butler et al. method [18] and the Yang et al. method [22].

Using the DW method, displacements are calculated by defining a mesh for the image with fluorescent beads without the cell I1 (i.e. the reference image). Each one of the nodes N in this mesh is coupled with a point with the same coordinates on the beads image with the cell I2. Then, a search area around this point in image I2 is defined. Each pixel in this area centers a squared window and is correlated to a same size window centered by the original node N in I1. The pixel that has the highest cross-correlation values is considered the best match for the original node *N* and its displacement is calculated.

According to the Butler et al. method, the correlation is achieved based on a small window rather than pixels. Briefly, a window, typically of 64 × 64 pixels, moves over image I1 and is correlated to the respective window in image I2. The coordinate of the peak cross-correlation is determined as the displacement of the window center in I1. For 0.2 μm beads, this specific window size was chosen to guarantee one fluorescent marker in each window. However, when changing the beads size or the magnification, the size of the window should be changed accordingly.

The Yang el al. method takes a different approach to find the displacements of the beads. The first step there is to identify the beads by requiring them to occupy a range of 4–8 pixels in the image. This is done by dividing the image into a window of 16 × 16 pixels for averaging the contrasts. The next step is to turn the image into a binary image where each pixel is assigned a value of 1 if its original value was higher than the averaged local intensity of the window, and 0 otherwise. A cluster of pixels that fell in the range of 4–8 pixels is deemed a bead. The matching between the two images is performed as follows: the distance between two beads in the image without the cell I1 is calculated. The same two coordinates are marked in the image with the cell I2 and a circle with a predefined radius is drawn around them. All the beads within the boundaries of one circle are connected to the beads in the second

circle and the displacement is calculated. The displacement that satisfies the best elongation and rotation criteria is chosen as a match for the original displacement in image I1.

The traction forces are derived from the displacement values calculated from the images of the beads. Each of the three aforementioned methods uses a different approach to calculate the traction force. DW and Butler et al. rely on the Boussinesq equation that assumes an infinite half-space substrate and gives the displacement values generated by a point load without taking the gel thickness into consideration. Yang et al. use a 3D finite element method for the displacement calculations.

Starting with the DW and Butler et al. methods, the relation between the displacements and the forces applied can be obtained using the theory of elasticity [23], after assuming zero body forces and an infinite half-space elastic substrate. The Green's functions $G(x)$ that relate the traction $t(x)$ to the displacements $u(x)$ are calculated through the Boussinesq solution. The above relation can be written as a convolution integral:

$$u(x) = \int G\left(x, x'\right) T\left(x'\right) dx' \tag{1}$$

The DW method solves Eq. (1) in the real space. They start by marking the cell boundaries and discretizing it using a mesh where the traction forces are assumed to be applied. Due to the fact that the number of displacement values calculated from the images is much larger than the number of traction forces that need to be found, the inversion of Eq. (1) is not possible. For resolving this problem, initial information about the expected tractions need to be estimated. This initial estimation is implemented by the Tikhonov regularization method where a minimization of a specific term will provide constrains that can be employed to Eq. (1) for solving it [24].

The Butler et al. method solves Eq. (1) in a Fourier field where convolution becomes a simple multiplication:

$$\tilde{u}(k) = \tilde{G}(k)\tilde{T}(k) \tag{2}$$

And the Green's function is as follows:

$$\tilde{G}(k) = \frac{2(1+\nu)}{Ek^3} \begin{pmatrix} (1-\nu)k^2 + \nu k_y^2 & -\nu k_x k_y \\ -\nu k_x k_y & (1-\nu)k^2 + \nu k_x^2 \end{pmatrix} \tag{3}$$

where k is the radial wave vector, ν is Poisson's ratio, E is Young's Modulus and $\tilde{u}, \tilde{G}, \tilde{T}$ are the Fourier transforms of the displacement, and Green's function and traction force, respectively. For finding the traction forces from the displacement field, one can multiply the displacements by the inverse Green's function and apply on the product a two dimensional inverse Fourier transform FT_2^{-1}:

$$\tilde{T}(k) = FT_2^{-1}(\tilde{G}(k)^{-1}\tilde{u}(k)) \tag{4}$$

This method offers two approaches for traction force recovery: Unconstrained and constrained methods. The unconstrained method does not require the confinement of the forces to be within a pre-marked location. In this method, the displacements are measured in all locations and the traction is calculated for each of the displacements. This enables the measurement of traction forces when the cell boundaries are not marked, such as in a monolayer traction analysis [25, 26]. However, in the constrained method the traction forces are confined within the marked cell boundaries. Thus, the calculation of the traction forces requires iterations of the traction forces found in the unconstrained method while setting the forces outside the boundaries to be zero. New displacement values are calculated from the modified traction force map. These values replace the measured displacement values and the unconstrained method is again applied in the next iteration. These iterations are repeated until a convergence is reached.

Yang et al. used a 3D finite elements method instead of the Boussinesq solution. In this method a static equilibrium equation is defined and the substrate is meshed with eight-node isoparametric brick elements. The static equilibrium equation relates the displacement matrix at the nodes u to the force matrix at the nodes F by a stiffness matrix K that contains the substrate characteristics as follows:

$$[K][u] = [F] \tag{5}$$

The forces in the nodes outside the cell boundaries are zero and the boundary conditions at the bottom of the substrates are fixed. Substituting this information in the above equation will allow the calculation of the nodal traction force using a finite element software package.

The three methods mentioned above are widely used in measurements of cell traction forces. The DW method differs from Butler et al. and Yang et al. primarily in the assumption that the displacement data far from the cell boundaries are also used for the traction measurements while the other methods set them to zero. The justification for the Butler et al. and Yang et al. method is that the displacements decays at a rate of 1/r away from the cell and its contribution to the traction field is hence negligible.

4 Mechanical Properties of Mesenchymal and Committed Cells

Mesenchymal stem cells (MSCs) are able to differentiate through a series of separate and unique transitions into a variety of different phenotypes, such as bone, cartilage, tendon, ligament, marrow stroma, fat, dermis, and muscle [27]. The MSCs are also capable of migrating and aggregating to form a new structure or to repair existing

structures. Rather than chemical signaling, MSCs are also affected by mechanical signaling along their differentiation process. It was shown that MSCs cultured on gels with different elastic properties have committed to different cell lineages. Soft gel matrices that mimic brain elasticity (elastic modulus of ~0.1–1 kPa) induced neural behavior in human MSCs [28, 29]. On gels mimicking muscle stiffness (elastic modulus of ~8–17 kPa), MSCs had a spindle shape morphology similar to that of myoblasts [28] and these myoblasts formed myotubes with improved sarcomere formation [30]. On much stiffer gels (i.e. elastic modulus of ~25–40 kPa), MSCs had a polygonal shape similar in morphology to that of osteoblasts [28].

To understand the changes in forces applied by stem cells during their growth and development from 2D into 3D colonies, Teo et al. [31] cultured murine embryonic stem cells (mESCs) on a 4200 Pa PAM gels. The mESCs transformed from 2D colonies into pluripotent 3D spheroids. During their growth, the traction forces applied by the cells on the PAM substrate decreased. This work showed that during 3D proliferation, the cell-cell interactions of the mESCs became more important than cell-substrate interaction. These cell-cell interactions seem to be essential for the stabilization of the colony structure.

Fu et al. [32] characterized in their study responses of human mesenchymal stem cells (hMSCs) to changes in the rigidity of substrates. They used PDMS microposts with different post heights to change the substrate rigidity. Cells cultured on soft microposts had a rounded morphology and disorganized actin filaments. On rigid microposts the cells were well spread and showed highly organized actin stress fibers. The Fu group also showed a strong correlation between traction forces and cell spreading, that is, when cells spreaded more they applied higher traction forces (with respect to rounded cells).

4.1 Traction Forces Exerted by Differentiating Adipocytes

Preadipocytes originate from stem cells and can become committed to the adipocyte lineage and fulfill a fat storage capacity [33]. Typically, they have an elongated spindle shape morphology which facilitates their proliferation and migration. During the differentiation to adipocytes, their morphology becomes rounded which enables a more efficient packaging of triglycerides within the cytoplasm. This change in morphology requires a change in the organization of cytoskeletal components. The organization of the cytoskeleton is responsible for changes in the forces exerted by the differentiating cells on their substrate.

Abuhattum et al. [17] recently evaluated the changes in morphology and the forces applied on an elastic gel substrate by preadipocytes during their differentiation process. Mouse embryonic 3T3-L1 preadipocytes were used and their differentiation was biochemically induced as described in previous work [34]. Single cells were cultured for 24 hours prior to traction force measurements on 2440 Pa collagen-coated PAM gels containing 0.2 μm fluorescence beads in their upper surface (Fig. 1a). Images for the cell and for the fluorescence beads were acquired. The cells were then removed

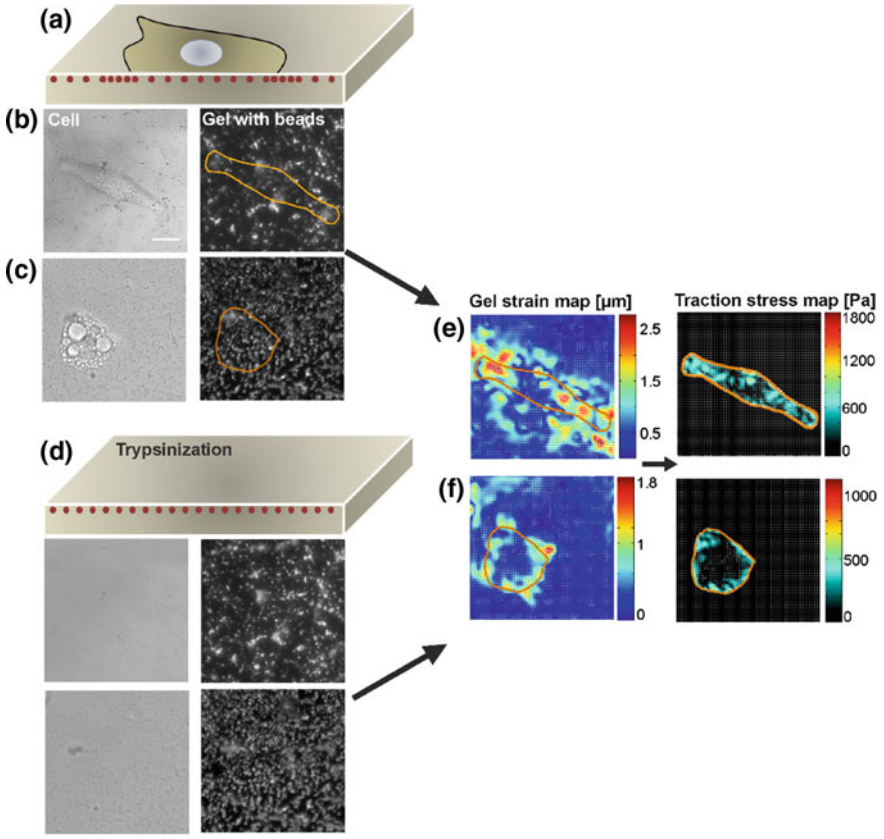

Fig. 1 Force traction microscopy of differentiating adipocytes: **a** a cell attached to a polyacrylamide gel substrate applies forces on the gel, which cause displacements of fluorescent beads under the surface of the gel. **b** An optical microscopy image of a preadipocyte, fibroblast-like cell (left) and the corresponding fluorescent image of the beads in the gel (right). **c** A microscopy image of a more mature adipocyte, where intracellular lipid droplets can be identified (left), and a corresponding fluorescent image of the beads in the gel. **d** The matching set of images after trypsinization which detaches the cells from the gel. **e** Strain and stress maps for the aforementioned preadipocyte. **f** Strain and stress maps for the aforementioned differentiating adipocyte

using trypsin to obtain a reference image of the gel without the traction forces that the cells applied (Fig. 1d). The displacement of the beads were calculated using a custom-made MATLAB algorithm based on the Butler el al. method which has been described previously [18], with window size of 32 × 32 to fit this specific experimental system. Strain and stress maps were obtained correspondingly, as depicted in Fig. 1.

5 Summary

This chapter reviewed the traction force microscopy method which is used to measure forces applied by cells on substrates under different culture conditions with a focus on forces applied by adipocytes during differentiation. Different relevant mathematical and computational theories for traction measurement were reviewed here, and were compared based on pros and cons, and implementations in various experimental setups. Furthermore, we summarized the literature with regard to the effects of variations in the mechanical environment on the commitment and differentiation of mesenchymal stem cells, as relevant to traction force microscopy work. We concluded by focusing on one example application, where we describe changes in the mechanical forces applied by preadipocytes onto a soft PAM gel substrate during their differentiation.

References

1. Wang JHC, Lin JS (2007) Cell traction force and measurement methods. Biomech Model Mechanobiol 6(6):361–371. https://doi.org/10.1007/s10237-006-0068-4
2. Fletcher DA, Mullins D (2010) Cell mechanics and the cytoskeleton. Nature 463(7280):485–492. https://doi.org/10.1038/Nature08908
3. Pollard TD, Cooper JA (2009) Actin, a central player in cell shape and movement. Science 326(5957):1208–1212. https://doi.org/10.1126/science.1175862
4. Valiron O, Caudron N, Job D (2001) Microtubule dynamics. Cell Mol Life Sci 58(14):2069–2084
5. Nagle RB (1994) A review of intermediate filament biology and their use in pathological diagnosis. Mol Biol Rep 19(1):3–21
6. Herrmann H, Bar H, Kreplak L, Strelkov SV, Aebi U (2007) Intermediate filaments: from cell architecture to nanomechanics. Nat Rev Mol Cell Bio 8(7):562–573. https://doi.org/10.1038/Nrm2197
7. Balaban NQ, Schwarz US, Riveline D, Goichberg P, Tzur G, Sabanay I, Mahalu D, Safran S, Bershadsky A, Addadi L, Geiger B (2001) Force and focal adhesion assembly: a close relationship studied using elastic micropatterned substrates. Nat Cell Biol 3(5):466–472
8. Kolega J, Janson LW, Taylor DL (1991) The role of solation-contraction coupling in regulating stress fiber dynamics in nonmuscle cells. J Cell Biol 114(5):993–1003
9. Elson EL, Felder SF, Jay PY, Kolodney MS, Pasternak C (1999) Forces in cell locomotion. Biochem Soc Symp 65:299–314
10. Schwarz US, Soine JR (2015) Traction force microscopy on soft elastic substrates: a guide to recent computational advances. Biochim Biophys Acta. https://doi.org/10.1016/j.bbamcr.2015.05.028
11. Bell E, Ivarsson B, Merrill C (1979) Production of a tissue-like structure by contraction of collagen lattices by human fibroblasts of different proliferative potential in vitro. Proc Natl Acad Sci USA 76(3):1274–1278
12. Moon AG, Tranquillo RT (1993) Fibroblast-populated collagen microsphere assay of cell traction force: Part 1. Continuum model. AIChE J 39(1):163–177. https://doi.org/10.1002/aic.690390116
13. Harris A, Wild P, Stopak D (1980) Silicone rubber substrata: a new wrinkle in the study of cell locomotion. Science 208(4440):177–179. https://doi.org/10.1126/science.6987736

14. Burton K, Taylor DL (1997) Traction forces of cytokinesis measured with optically modified elastic substrata. Nature 385(6615):450–454. https://doi.org/10.1038/385450a0
15. Dembo M, Wang YL (1999) Stresses at the cell-to-substrate interface during locomotion of fibroblasts. Biophys J 76(4):2307–2316
16. Pelham RJ, Wang YL (1997) Cell locomotion and focal adhesions are regulated by substrate flexibility. Proc Natl Acad Sci USA 94(25):13661–13665
17. Abuhattum S, Gefen A, Weihs D (2015) Ratio of total traction force to projected cell area is preserved in differentiating adipocytes. Integr Biol. https://doi.org/10.1039/c5ib00056d
18. Butler JP, Tolic-Norrelykke IM, Fabry B, Fredberg JJ (2002) Traction fields, moments, and strain energy that cells exert on their surroundings. Am J Physiol Cell Physiol 282(3):C595–C605
19. Galbraith CG, Sheetz MP (1997) A micromachined device provides a new bend on fibroblast traction forces. Proc Natl Acad Sci USA 94(17):9114–9118
20. du Roure O, Saez A, Buguin A, Austin RH, Chavrier P, Silberzan P, Ladoux B (2005) Force mapping in epithelial cell migration. Proc Natl Acad Sci USA 102(7):2390–2395. https://doi.org/10.1073/pnas.0408482102
21. Marganski WA, Dembo M, Wang YL (2003) Measurements of cell-generated deformations on flexible substrata using correlation-based optical flow. Methods Enzymol 361:197–211
22. Yang Z, Lin JS, Chen J, Wang JH (2006) Determining substrate displacement and cell traction fields—a new approach. J Theor Biol 242(3):607–616. https://doi.org/10.1016/j.jtbi.2006.05.005
23. Lldlemkamp LP (1986) Theory of elasticity. Elsevier
24. Dembo M, Oliver T, Ishihara A, Jacobson K (1996) Imaging the traction stresses exerted by locomoting cells with the elastic substratum method. Biophys J 70(4):2008–2022. https://doi.org/10.1016/S0006-3495(96)79767-9
25. Del Alamo JC, Meili R, Alonso-Latorre B, Rodriguez-Rodriguez J, Aliseda A, Firtel RA, Lasheras JC (2007) Spatio-temporal analysis of eukaryotic cell motility by improved force cytometry. Proc Natl Acad Sci USA 104(33):13343–13348. https://doi.org/10.1073/pnas.0705815104
26. Trepat X, Wasserman MR, Angelini TE, Millet E, Weitz DA, Butler JP, Fredberg JJ (2009) Physical forces during collective cell migration. Nat Phys 5(6):426–430. https://doi.org/10.1038/Nphys1269
27. Caplan AI (1991) Mesenchymal stem cells. J Orthop Res 9(5):641–650. https://doi.org/10.1002/jor.1100090504
28. Engler AJ, Sen S, Sweeney HL, Discher DE (2006) Matrix elasticity directs stem cell lineage specification. Cell 126(4):677–689. https://doi.org/10.1016/j.cell.2006.06.044
29. Saha K, Keung AJ, Irwin EF, Li Y, Little L, Schaffer DV, Healy KE (2008) Substrate modulus directs neural stem cell behavior. Biophys J 95(9):4426–4438. https://doi.org/10.1529/biophysj.108.132217
30. Serena E, Zatti S, Reghelin E, Pasut A, Cimetta E, Elvassore N (2010) Soft substrates drive optimal differentiation of human healthy and dystrophic myotubes. Integr Biol 2(4):193–201. https://doi.org/10.1039/b921401a
31. Teo A, Lim M, Weihs D (2015) Embryonic stem cells growing in 3-dimensions shift from reliance on the substrate to each other for mechanical support. J Biomech 48(10):1777–1781. https://doi.org/10.1016/j.jbiomech.2015.05.009
32. Fu J, Wang YK, Yang MT, Desai RA, Yu X, Liu Z, Chen CS (2010) Mechanical regulation of cell function with geometrically modulated elastomeric substrates. Nat Methods 7(9):733–736. https://doi.org/10.1038/nmeth.1487
33. Shoham N, Gefen A (2012) Mechanotransduction in adipocytes. J Biomech 45(1):1–8
34. Shoham N, Mor-Yossef Moldovan L, Benayahu D, Gefen A (2015) Multiscale modeling of tissue-engineered fat: is there a deformation-driven positive feedback loop in adipogenesis? Tissue Eng Part A 21(7–8):1354–1363. https://doi.org/10.1089/ten.TEA.2014.0505
35. Tan JL, Tien J, Pirone DM, Gray DS, Bhadriraju K, Chen CS (2003) Cells lying on a bed of microneedles: an approach to isolate mechanical force. Proc Natl Acad Sci USA 100(4):1484–1489. https://doi.org/10.1073/pnas.0235407100

Adaptive Multi-resolution Volumetric Modeling of Bone Micro-structure

Yizhak Ben-Shabat and Anath Fischer

Abstract The emerging field of additive manufacturing with bio-compatible materials has led to personalized design of porous micro-structures used in healthcare. Complex micro-structures are characterized by freeform surfaces and spatially varying porosity. Currently, there is no CAD system that can handle the design of micro-structures due to their high complexity. This paper describes a direct expansion of our research on *reconstructing 3D adaptive models of porous micro-structures*. Using this approach, a designer can either manually select a Region of Interest (ROI), or define a curvature based criterion for selecting ROI while defining its level of detail. In the proposed approach, the multi-resolution volumetric model is based on designing a customized model, composed of the following stages (a) Reconstructing a multi-resolution volumetric model of a porous structure; (b) Defining ROIs and their resolution properties; and (c) Constructing an adaptive model. The feasibility of the proposed method is demonstrated on 3D models of porous micro-structures. These models are characterized by a large amount of detail and geometrical complexity. The proposed method has been applied on bone models that were reconstructed from micro-CT images. The proposed approach facilitates the porous characteristic and enables local reduction of the model complexity while optimizing the accuracy. For additive manufacturing application, the approach can be used for designing a porous micro-structure while reducing material volume and eliminating irrelevant geometric features.

Keywords Bone micro-structure · Multi-resolution · Adaptive volumetric modeling

Y. Ben-Shabat · A. Fischer (✉)
Faculty of Mechanical Engineering, Technion, 32000 Haifa, Israel
e-mail: meranath@technion.ac.il

P. R. Fernandes and P. J. da Silva Bartolo (eds.), *New Developments in Tissue Engineering and Regeneration*, Computational Methods in Applied Sciences 51,
https://doi.org/10.1007/978-3-030-15372-4_3

1 Introduction

Multi-resolution volumetric modeling is applied in a variety of fields, including additive manufacturing, computer vision, virtual reality, finite element analysis and CAD. In recent years the significance of multi-resolution modeling has increased due to the ability of creating highly detailed models. It improves the effectiveness of computation, transmission, storage and visualization of the geometric model. Visualizing a high resolution model is time consuming and requires high computer resources. In order to cope with this challenge an adaptive method is required. Such method enables to select Regions of Interest (ROI) with desired resolutions. In this manner an artificial fusion between different resolutions is generated.

Volumetric hierarchical representations allow a bi-directional transition from a macro- to micro-resolution models using levels of detail (LOD). The most common hierarchical multi-resolution data structures for 2D images and 3D volumes are Quadtree and Octree, respectively. Their main principle is the recursive decomposition of space by a factor of two for each axis [1, 2]. These data structures are also compatible for methods which generate adaptive multi-resolution models with ROIs, which can be defined either manual or based on geometric properties.

In the field of computer graphics and CAD, the geometrical characteristics of surfaces play an important role in many applications such as: feature extraction and contouring. Curvature is one of the most important surface characteristic. For continuous representation of parameterized surfaces the challenge of deriving shape characteristics can be expressed in a closed form formula of differential geometry. However, for discrete surfaces, represented as volumetric voxel model or by a triangular mesh, an approximation is applied. For volumetric voxel models, to the best of our knowledge, there is no direct method that approximates the voxel curvature. Therefore, in order to calculate the curvature of a discrete voxel volumetric model, first the underlying surface must be approximated.

The goal of this work is to develop a new CAD method for the design of porous micro-structures as a module of a larger system for bone diagnosis and implant scaffold design. This proposed system is illustrated in Fig. 1 and consists of the following stages:

a. High resolution medical imaging—acquiring the bone input geometry.
b. Image segmentation—differentiating between bone and background segments.
c. 3D model reconstruction—from 2D images into a 3D volumetric model.
d. Multi-scale finite element analysis (FEA)—analysing the stress and strain regimes on the bone.
e. Micro-scale scaffold design—designing a patient specific custom scaffold according to the geometry and FEA.
f. Diagnosis/Treatment assessment—based on the collected data from previous stages a medical treatment plan may be assessed.

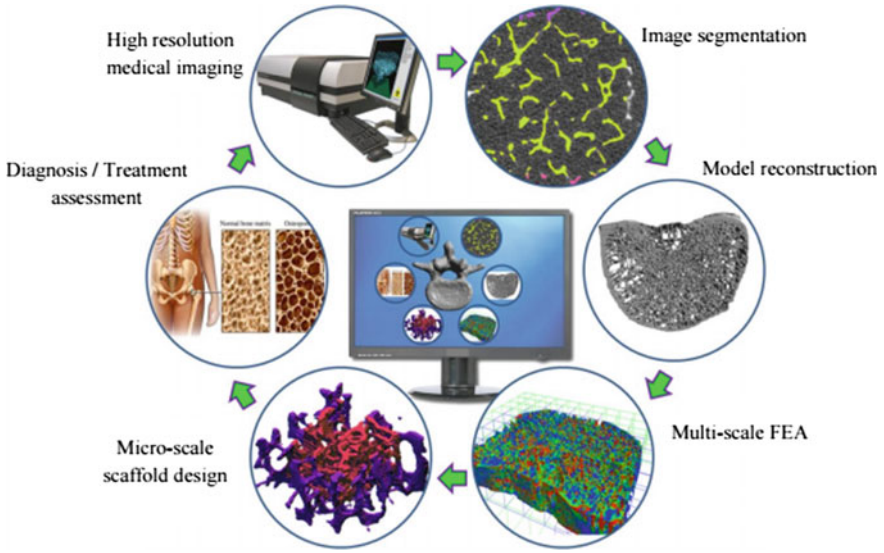

Fig. 1 Computerized system for design and diagnostic of bones [3]

2 Approach

The approach is composed of four main stages:

- CT image processing
- Multi resolution model construction
- Region of interest selection
- Adaptive model construction

Following is a detailed description of each stage:

a. *Input Processing*—In this work we use the Quadtree and Octree data structures for the representation of 2D images and 3D volumes [1, 2, 4]. These data structures are based on nodes and their connectivity relations and facilitate the hierarchical nature of multi-resolution models.
b. *Multi resolution model construction*—this stage is based on two options:

   1. No topological preservation method—B/W color check is performed and the lower LODs are constructed only according to B/W color information.
   2. Topological preservation method—An extension was made for the 2D topological preservation method proposed by Jia et al. [5] to 3D volumetric models of voxels in a similar manner as Whalen [6].
      The topological preservation method consists of two steps:
      i. A connectivity test of the neighbouring nodes for the B/W elements and its relation to the original connectivity of the node.
      ii. A B/W color test of the neighbouring nodes.

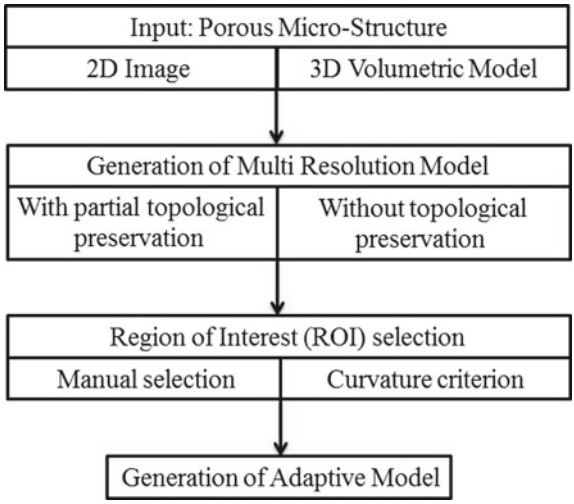

Fig. 2 Block diagram of the proposed approach

c. *Region of interest (ROI) selection*—this stage is based on one of two selection options:

   1. Manual selection—The user defines location, geometry and LOD.
   2. Curvature criteria selection—the location of the LOD is determined by the curvature properties of the underlying surface and the geometry and LOD.

d. *Adaptive model construction*—the information from the previous stages is combined and visualized as an adaptive model which contains the different, predefined, LODs in a single model.

The method was applied on 2D images and 3D volumes of porous microstructures. A visual and quantitative comparison of the resulting models was conducted. A block diagram of the approach is depicted in Fig. 2.

3 Implementation

In this research the representation method for Quadtree and Octree proposed by Gargantini [4] was used. The highest LOD was stored in the tree leaves and the lowest LOD was stored the root of the tree. The different tree levels were generated in a bottom-up manner; therefore every consequent level is generated according to its children.

The result of this method is a structure, from which the path to each node along the hierarchy can be extracted. The hierarchical nature of the tree structure is based on an explicit representation of hierarchical levels of detail. An extension of Podshivalov et al. approach [3, 7, 8] was made, generating the hierarchical structure in a bottom-up approach and storing each level of detail separately. A mask field was introduced

for each node and was populated after selecting a region of interest (ROI). The Area of Interest (AOI) was defined in an image, while the Volume of Interest (VOI) was defined in a volumetric model. The mask was populated only for nodes that are inside the ROI. The mask represents the LOD for each node. This mask enables the visualization of nodes from multiple levels according to the ROI.

There are some cases in which an ROI is selected only for a subset of the children of a given ancestor. In this case the ROI does not explicitly define an LOD for these nodes. The proposed method ensures that the LOD is defined implicitly for these nodes as the maximum allowed LOD.

Figure 3 shows an example of the mask preservation in the matrix form (a–d) and in tree data structure form (e) on a 2D image: Fig. 3a represents the initial 8×8 image i.e. the highest LOD and an AOI selection in the shape of a square of size 2×2 in the bottom center (marked in red). The LOD inside the square is defined to be 1. Figure 3b–d represents the masks of LODs 2, 3, 4, respectively. Figure 3e demonstrates a graphical representation of the tree data structure of the AOI selection marked in red and the mask field across the different levels. It can be seen in each level that a subset of children nodes does not include the ROI, however it still effects their value.

The approach is not limited by the geometry or the LOD distribution of the ROI. In previous work [9] four manual, user defined ROIs, were introduced: (a) rectangular AOI with a constant LOD; (b) circular AOI with a linear change of LOD between center and circumference; (c) cuboid VOI with constant LOD; and (d) spherical VOI with linear change of LOD between center and bounding surface. In another work [10], an ROI selection criteria based on surface curvature was proposed. To the best

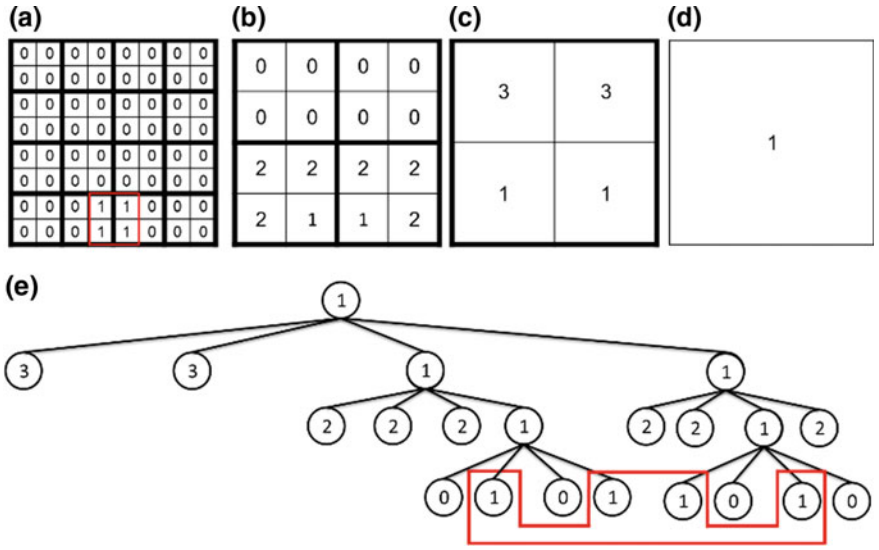

Fig. 3 Mask values in matrix and Quadtree form. **a** Mask field of level 1—highest level and AOI marked in red; **b–d** mask field of matrix levels 2–4 respectively, and **e** mask field values in Quadtree structure form with AOI marked in red (Color figure online)

of our knowledge, there is no direct method to approximate the voxel curvature for volumetric voxel models. Therefore, in order to approximate the curvature, first the underlying surface is approximated. The "marching cubes" algorithm [11] was used for approximating the underlying surface as a triangular mesh. A fairing algorithm [12] was then used to smooth the stair like affect created when approximating the volumetric representation as a triangle mesh. Finally, Rusinkiewicz curvature estimating algorithm [13] was used to retrieve the curvature tensor and principal curvature in each vertex. The curvature based ROI selection criterion is applied on each voxel. Visualization of the principal curvatures is performed using a color coding scheme. For each vertex in the mesh, the principal curvatures k1 and k2 were examined.

The calculation of levels of detail requires conversions and manipulations of the data in order to preserve topological information. The 2D and 3D space was defined according to definition 2.1 given by Kong [14], who describes the adjacency for elements which are full and elements which are empty in order to prevent topological paradoxes. The topological preservation process uses the image shrinking algorithm described by Jia et al. [5]. The algorithm examines the effect of changing a node's B/W color on the connectivity of its surrounding node neighbours. Fundamentally, this introduces an additional B/W color constraint in images and volume constraint for 3D models when traversing from a higher resolution to a lower one. Finally, the processed model undergoes through a visualization stage where hexahedral faces are drawn on a 2D plane or in a 3D space. The size of the faces is determined by its LOD parameters. This process results in an adaptive model.

4 Examples and Discussion

4.1 2D Examples—Adaptive Models

In Fig. 4 the 2D result models of the approach using manual selection is presented. Figure 4a–e depicts a synthetic 2D equivalent for a porous microstructure in the form of uniformly distributed circular holes in a 128 × 128 image. The AOI is marked by a circle of 64 pixels radius placed in the image center. The AOI properties are defined to be the maximum resolution in the center of the circle and change linearly to the minimum resolution on the circles circumference. The final model contains 8 LODs. However only LODs 1–5 are presented since levels 6–8 are redundant. Figure 4f presents the image fourth LOD without the AOI for reference. Note that black pixels represent the presence of material and white pixels represent its absence.

Figure 5a–f depicts a 128 × 128 2D multi-resolution model of a bone section micro-structure. In this example a rectangular AOI was defined by the user around a specific cavity. The resolution inside the AOI was defined to be constant. Therefore a change was observed inside the AOI between (a) and (b) (levels one and two) however no change inside the AOI between (b) and (f). Outside the AOI, the change in resolution is evident. This model has 8 levels of detail, only 6 are presented since levels 6–8 are redundant.

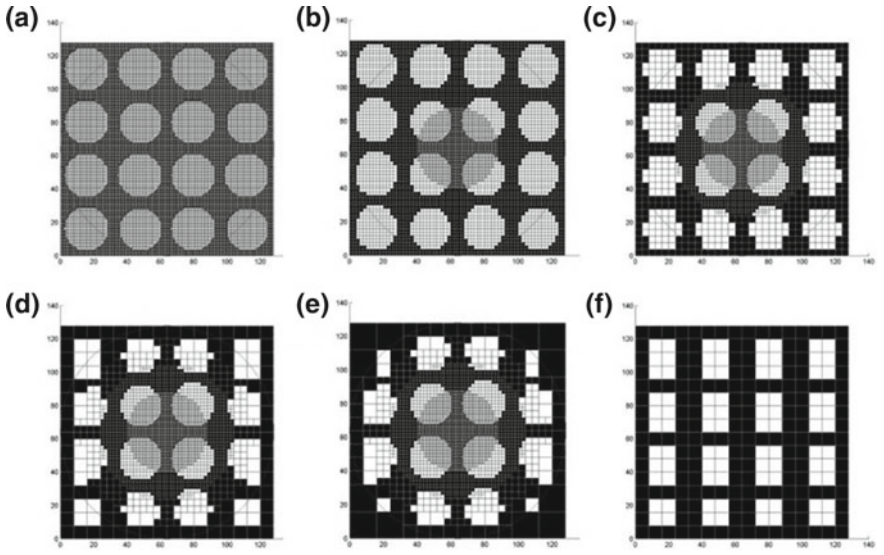

Fig. 4 Adaptive model of 128 × 128 images with a circular linearly varying AOI. **a** Level one (input model), **b–e** levels two to five respectively, **f** level four of the same input without AOI for reference (Color figure online)

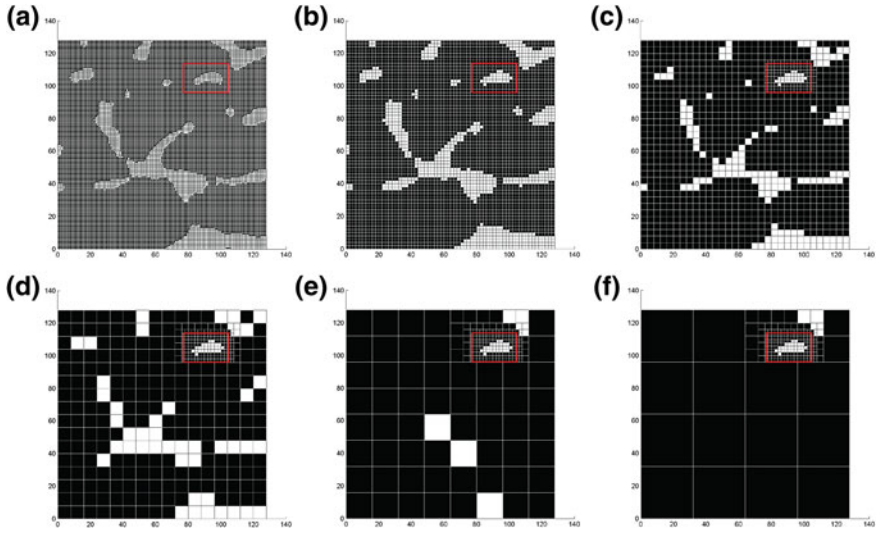

Fig. 5 Adaptive model of bone section microstructure with rectangular AOI. **a** Level one (input model), and **b–f** levels two to six respectively (Color figure online)

4.2 3D Examples—Bone Fragment Extraction

In the following example, a fragment of a μCT slice of L3 vertebra model was used. The extraction of the fragment was performed by overlaying a 12×10 grid over the entire model. Each grid element is a 128^3 cube of voxel data which was processed separately. The extraction of these cubes was performed for computational speed and memory consumption reasons. Note that the entire original high resolution vertebra model requires approximately 1 GB of memory only for its volumetric representation. Furthermore, a database for computational applications will require much more memory, for example, in finite element analysis the memory increases as a function of the problems degrees of freedom for each node. In Fig. 6 the extraction process is illustrated.

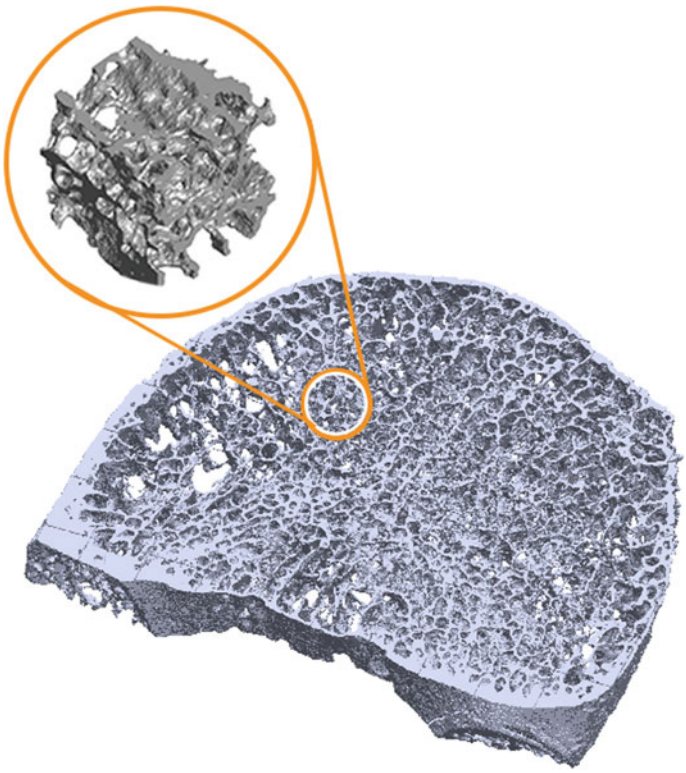

Fig. 6 Extraction of a 128^3 cube from a slice of L3 vertebra

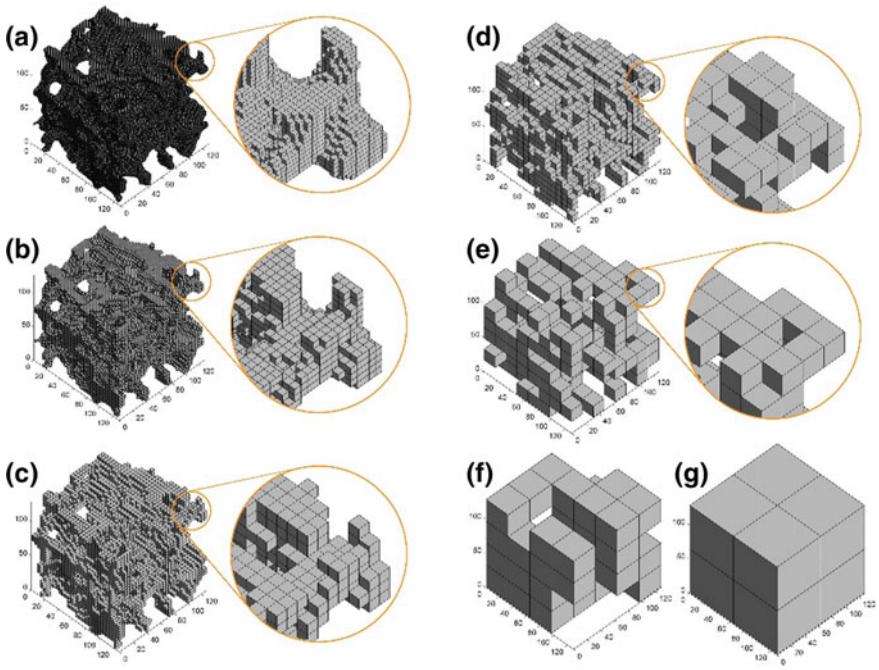

Fig. 7 Multi-resolution model of 128^3 μCT image, L3 vertebra volume segment. **a**–**g** Levels of detail 1–7 respectively

4.3 3D Examples—Multi-resolution Models

The bone fragment from the previous section was used to generate a hierarchical multi-resolution model according to the original high-resolution model. Figure 7a depicts the original high-resolution bone fragment, Fig. 7b–g depict LODs 2–7 respectively.

4.4 3D Examples—Curvature Analysis

Visualization of the curvature analysis was performed using a color map for each vertex. Each vertex color is determined by a linear interpolation between nine pairs of control values. These control values correspond to all possible combinations, positive, zero and negative, of k1 and k2. The result of the interpolation is depicted in Fig. 8. The color coding scheme was chosen this way in an effort to represent both principal curvatures in a single color map.

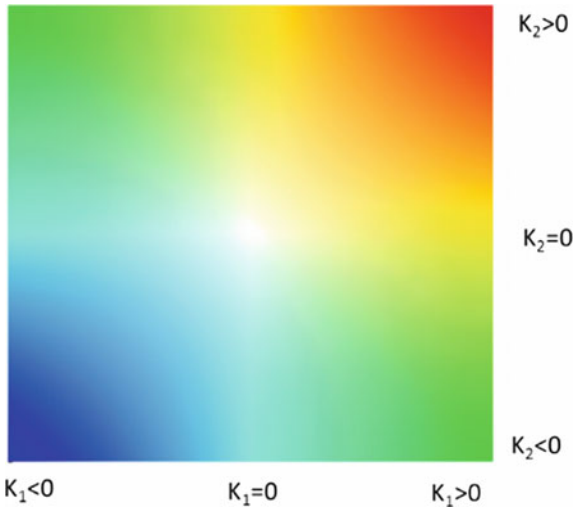

Fig. 8 Principal curvature color coding scheme of the proposed method (Color figure online)

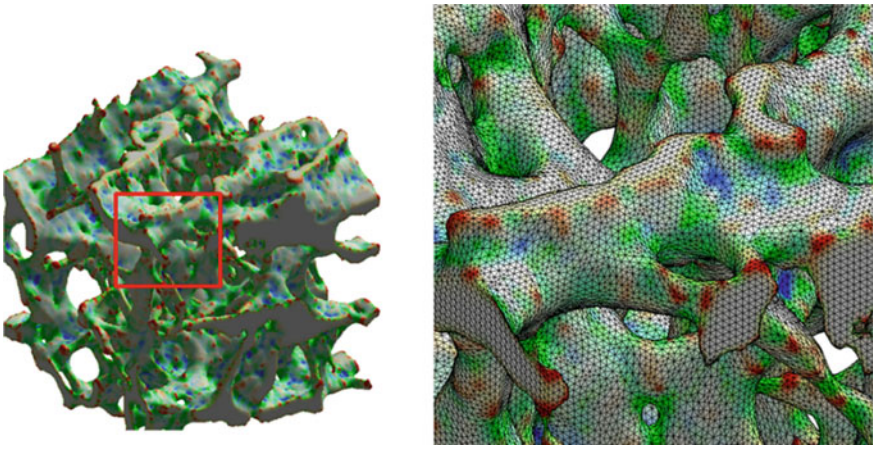

Fig. 9 Color coded curvature analysis of a bone fragment micro structure. Left—bone fragment, right—enlarged area with visible triangle mesh (Color figure online)

The principal curvatures of the extracted high-resolution bone fragment model were estimated. Figure 9 depict the results of the curvature analysis which was applied on a bone fragment micro structure. Figure 10 provides a zoomed in detailed view on some ROIs such as valleys (indicated in blue), ridges (indicated in red) and holes (indicated in green).

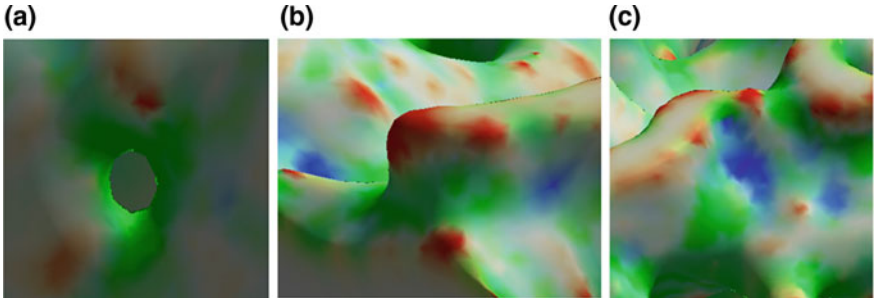

Fig. 10 Curvature analysis color coded ROIs. **a** local hole; **b** local ridge, and **c** local valley (Color figure online)

4.5 Topological Preservation

In the case of 2D images a synthetic image that mimics the characteristics of a slice of a porous micro-structure was manually generated in order to explore the topological preservation method effect. This image is essentially a 128^2 black image with white circles distributed on a grid. The diameter of the circles and the spacing between them were chosen arbitrarily and represent the porosity (white holes). Figure 11a depicts the original image and the multi resolution image with topological preservation (b–e) and without it (f–i). It is evident that without the topological preservation method, the holes grow larger as the LOD decreases until eventually a completely white image is reached. On the other hand, when imposing the topological preservation method, the white circles gradually shrinks until eventually a completely black image is reached. Note that there is no change in the last three LODs and they are not presented because they are redundant. Quantitatively, the topologically preserved model maintains a single connected component throughout all of its LODs while the non-preserving model maintains a single connected component until LOD 3 is reached. In level 4 it has twenty five connected components and in level 6 none.

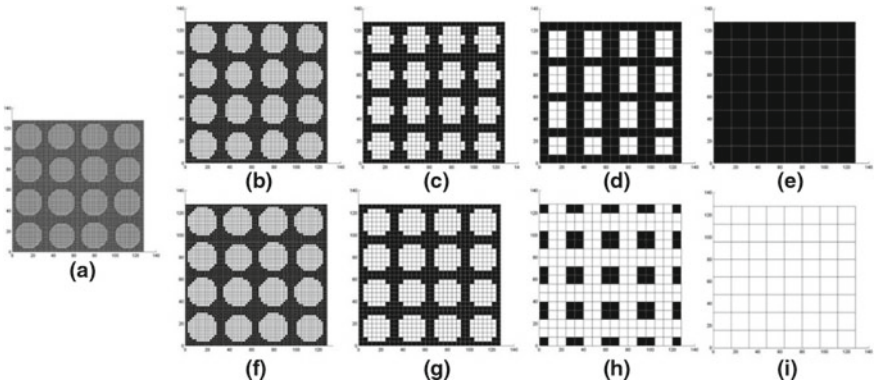

Fig. 11 A 128^2 image with circular holes. **a** original image (highest LOD); **b–e** LOD 2–5 with topological preservation—black connectivity preserved, and **f–i** LOD 2–5 without topological preservation—black connectivity not preserved (Color figure online)

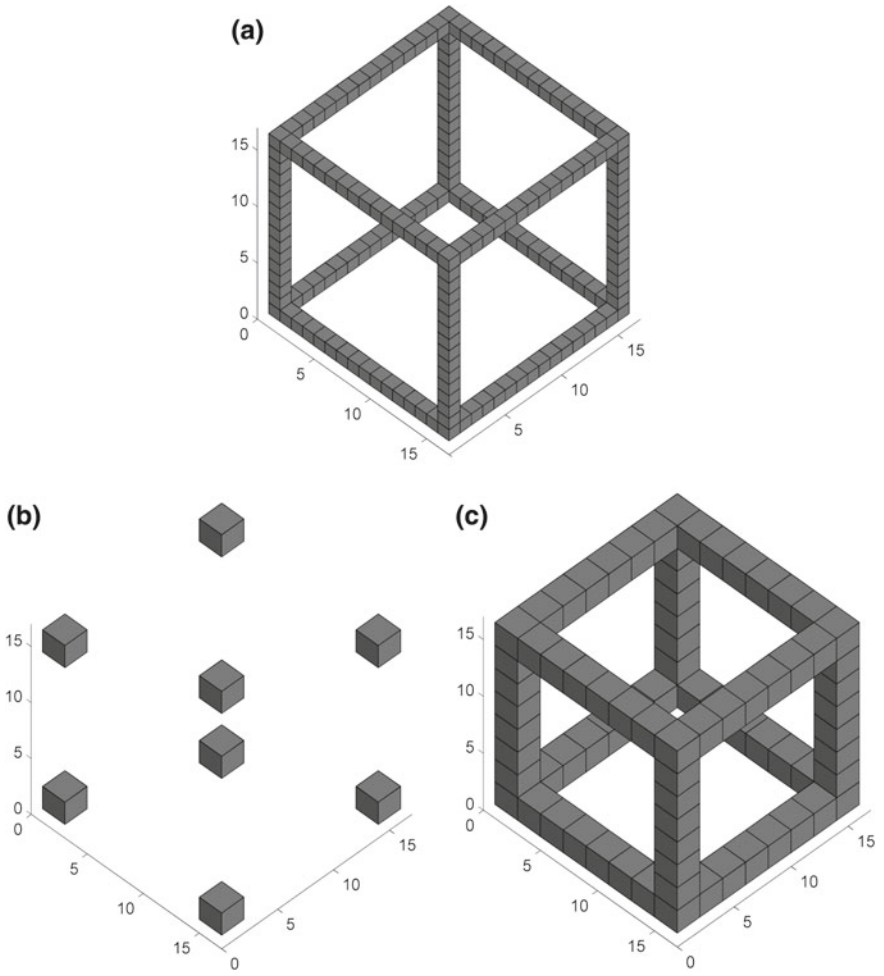

Fig. 12 Cube wireframe model. **a** Original model. **b** Lower LOD without topological preservation. **c** Lower LOD with topological preservation

The main effect of topological preservation on a 3D model is depicted in Fig. 12 which show an original model of a wireframe cube. Without topological preservation the wire frame cube model changes significantly, it generates eight connected components instead of the initial one. When using the topological preservation method there is only one connected component, yet the frame thickness increases.

Finally, the approach was applied on a bone fragment porous micro-structure. The effect of the topological preservation method on LODs 2–5 is depicted in Fig. 13. Since it is visually difficult to distinguish between the different connected components, they were colored differently. It is evident that when utilizing the topological preservation method there are significantly less components that disconnected from the main component.

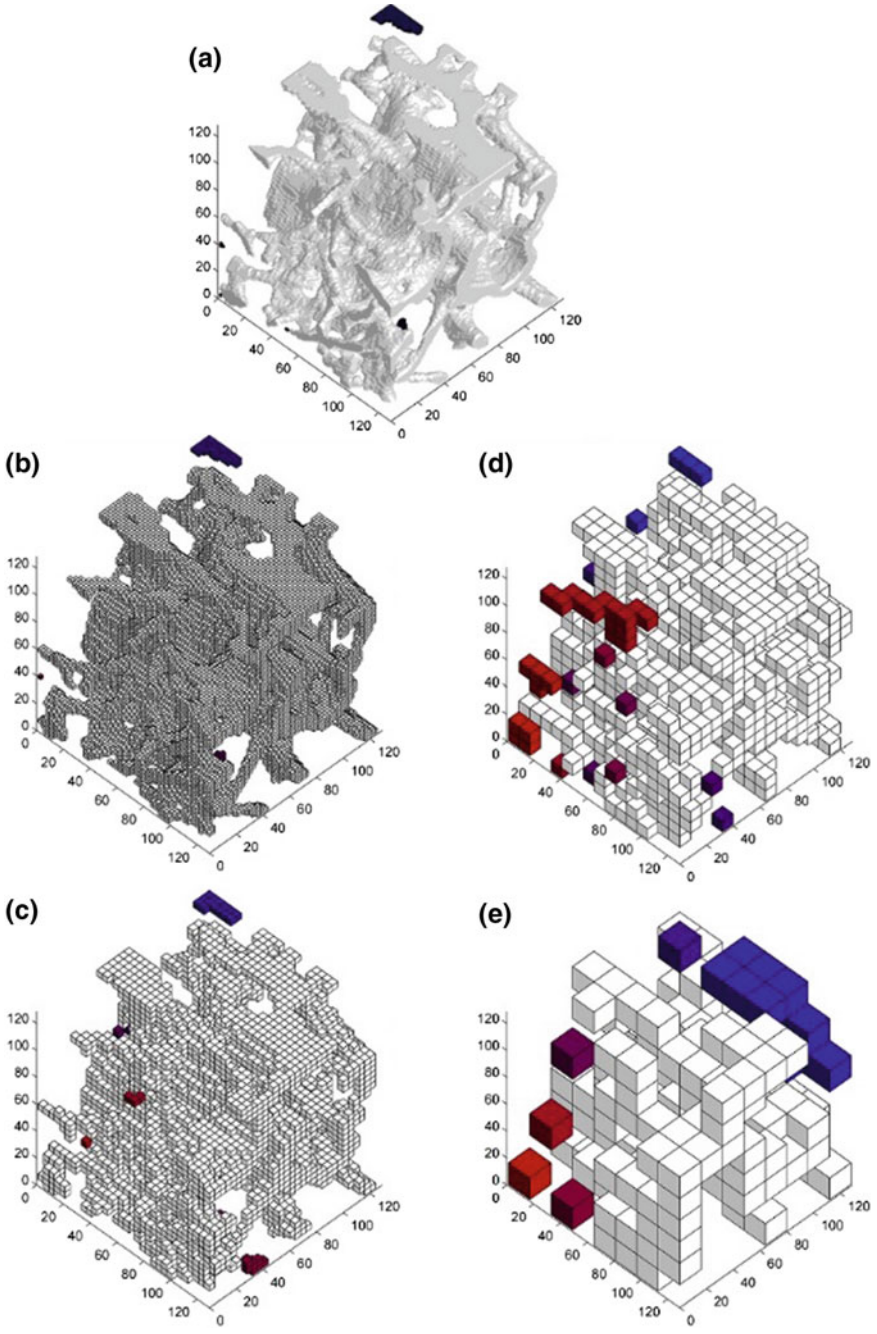

Fig. 13 128^3 Bone porous micro-structure. **a** Original model **b–e** LODs; 2–5 without topological preservation, and **f–i** LODs 2–5 with topological preservation (Color figure online)

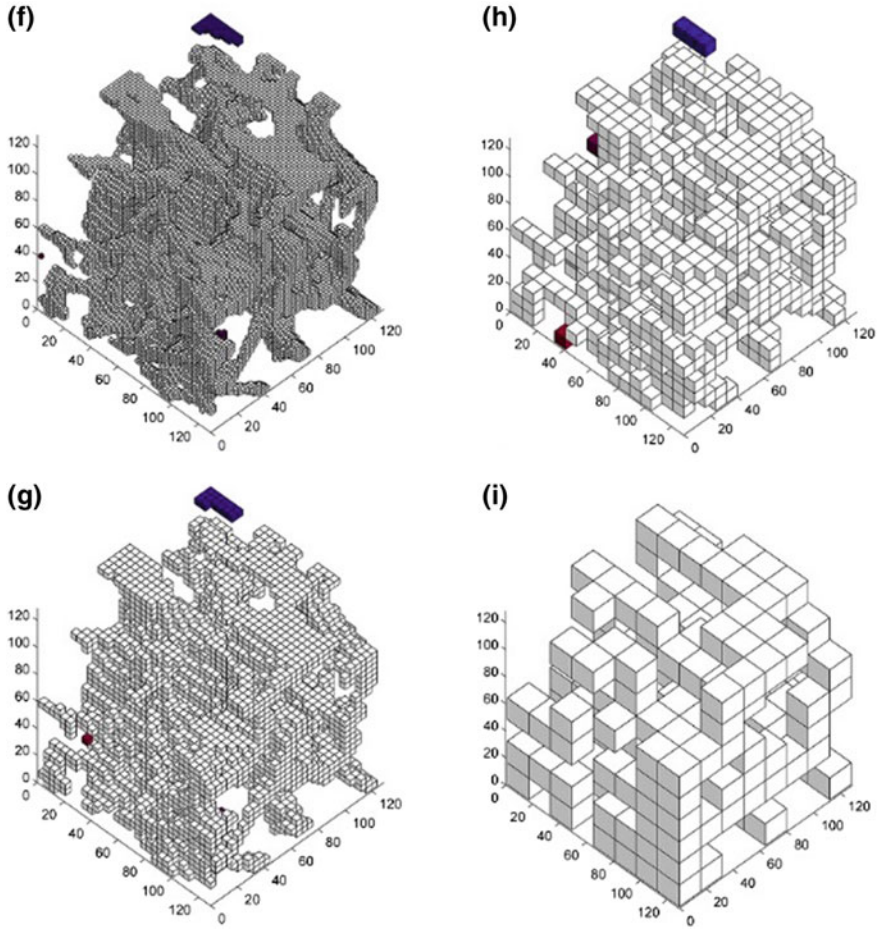

Fig. 13 (continued)

A quantitative comparison of the connected components created using the two methods is presented in Fig. 14. The value for each LOD is the average and standard deviation over 20 different bone fragments. Both datasets converge to a single connected component in the lowest LOD. However, there is a significant difference (in 95% certainty) in LODs 3–5, indicating that when the topology is not preserved, a large amount of components get separated from the main component.

Furthermore, an analysis was performed for the volumetric error between the original model and each LOD. The error was subdivided into two main components:

a. Black error ($\boldsymbol{error}_{\boldsymbol{Black}}$)—The relative portion of elements which were black in the original model and transformed to white in a lower LOD in relation to the entire volume.

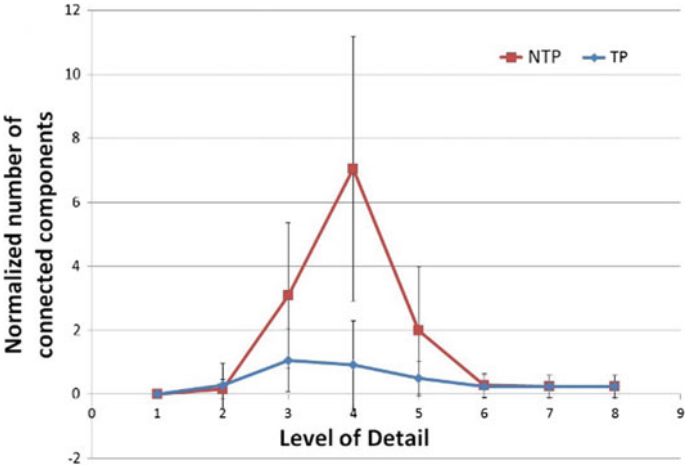

Fig. 14 Quantitative comparison of the normalized average number of connected components relative to the level of detail when using topological preservation method (TP) and not using topological preservation method (NTP). 20 bone fragments were used

b. White error ($\boldsymbol{error}_{\boldsymbol{White}}$)—The relative portion elements which were white in the original model and transformed to black in a lower LOD in relation to the entire volume.

The black error and white error components were given penalty weights $\boldsymbol{P}_{\boldsymbol{Black}}$, $\boldsymbol{P}_{\boldsymbol{White}}$ respectively. The error calculation formula is given in (1).

$$\boldsymbol{error} = \boldsymbol{P}_{\boldsymbol{Black}} \cdot \boldsymbol{error}_{\boldsymbol{Black}} + \boldsymbol{P}_{\boldsymbol{White}} \cdot \boldsymbol{error}_{\boldsymbol{White}} \tag{1}$$

Penalty values were initially set to be $\boldsymbol{P}_{\boldsymbol{Black}} = \boldsymbol{P}_{\boldsymbol{White}} = 1$. The average and standard deviation results for the case of no topological preservation (NTP) and with topological preservation (TP) are presented in Fig. 15. The topological preservation method demonstrates larger errors starting at the fourth LOD. This is due to the constraint which prefers the formation of new bonds and the creation of material over the separation of connected components. However, statistically these two datasets are not significantly different. In order to avoid this misleading result the penalty values were set to be $\boldsymbol{P}_{\boldsymbol{Black}} = 1$, $\boldsymbol{P}_{\boldsymbol{White}} = 0$, making it acceptable if an element turned from white to black from the original model to a lower LOD. Results for this case are depicted in Fig. 16. It is evident that the error for all LODs is either equal or lower for both methods. Statistical analysis concludes that LODs 4, 5 and 6 of the two methods are significantly different in 95% certainty level.

In conclusion of the statistical analysis, when utilizing topological preservation methods there were less disconnected components and lower volumetric error.

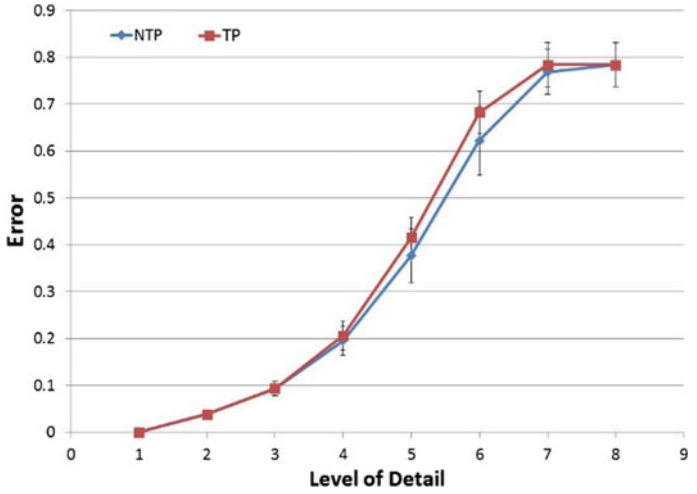

Fig. 15 Error comparison between non-topological preserved model (NTP) and a topological preserved model (TP) for $\boldsymbol{P_{Black}} = \boldsymbol{P_{White}} = 1$

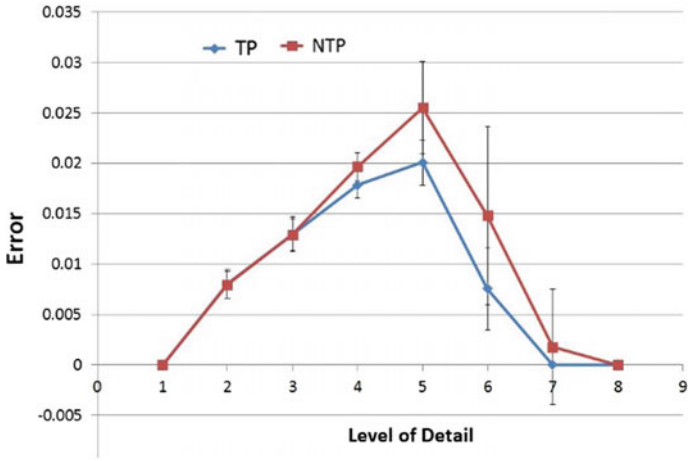

Fig. 16 Error comparison between non-topological preserved model (NTP) and a topological preserved model (TP) for $\boldsymbol{P_{Black}} = 1, \boldsymbol{P_{White}} = 0$

4.6 3D Examples—Adaptive Models

The bone fragment was subjected to a VOI selection. The VOI was a sphere located at the top center of the fragment with a diameter equal to the fragment width. The level of detail inside the VOI was chosen to be the highest possible. In similarity to the previous 2D example, the approach yields a unified visualization of the high LOD inside the VOI (red small voxels) and low LOD outside the VOI (color gradient

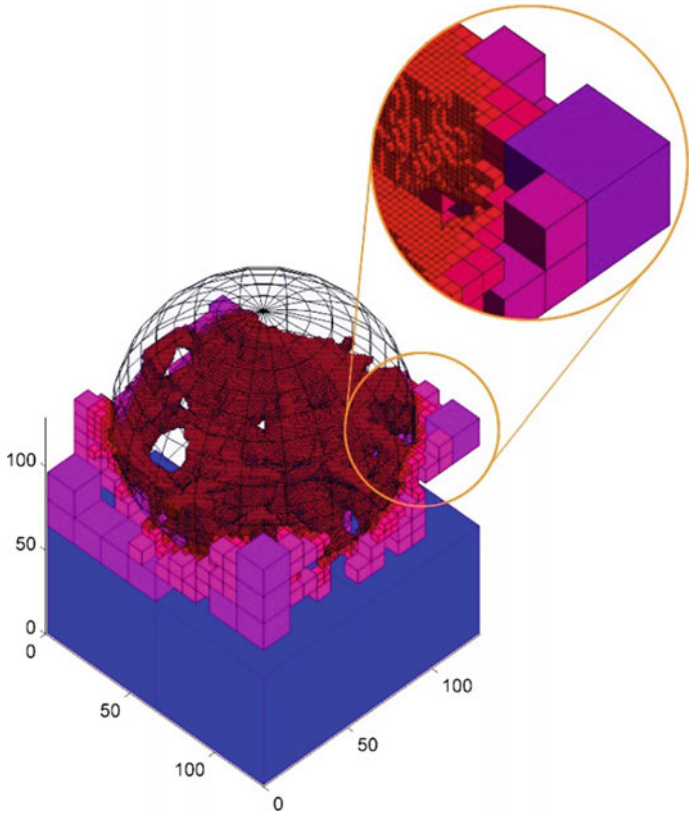

Fig. 17 Adaptive model of 128^3 μCT images, L3 vertebra volume segment with spherical, constant resolution VOI (Color figure online)

from red to blue voxels). In other words it is evident in Fig. 17 that inside the VOI, all of the geometry is maintained while on the exterior information is reduced.

In addition an adaptive model was also generated after a VOI was selected based on a curvature criterion. Here the selection criterion was chosen to be a high value of normal curvature. In order to distinguish between different areas of high curvature, non-maximal suppression was used to find local maximum values. Potential ROIs were selected to be the ten vertices with the highest normal curvature with radius of 15% of the model size. The potential ROIs are depicted in Fig. 18, the spheres are semi-transparent and their color corresponds to their curvature value (red is the highest and blue the lowest of the ten). Note that here only some of the spheres are visible because of the point of view.

The bottom center ROI was arbitrarily chosen. The LOD in it was defined to be the maximal inside and minimal outside. The result is depicted in Fig. 19. It can be seen that the local rod feature which includes a ridge that generated the high normal curvature is fully preserved while the rest of the model is coarsely approximated. The

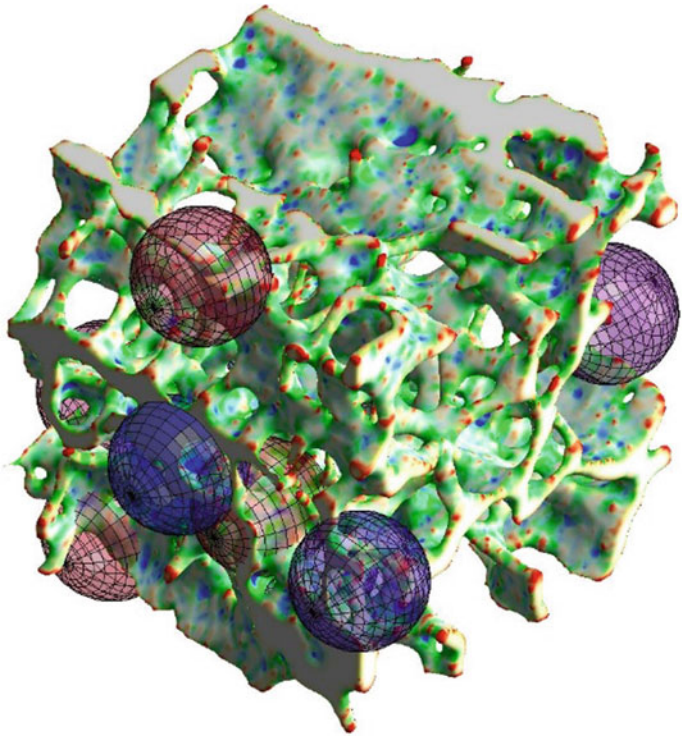

Fig. 18 Bone fragment porous structure with color coded curvature values and potential spherical ROIs based on normal curvature values (Color figure online)

color coding here represents the LOD of the elements—red elements are from the highest LOD and blue elements are from the lowest LOD, all other elements color is a linear interpolation between the red and blue.

5 Summary and Conclusions

An adaptive multi-resolution method for hierarchical volumetric models has been presented. The adaptive model is represented by octree. The hierarchical structure was generated and represented in a multi-resolution data structure. The adaptive model was constructed with a mask field. Regions of interest were defined by curvature characteristic and parameters of geometric elements for different LODs.

One of the main advantages of the presented approach is that it enables control over levels of detail for volumetric models and is not limited to a single level. Furthermore, in this paper a few types of ROIs were presented. However, the approach can accommodate for any ROI requirement. There are a few limitations to the approach.

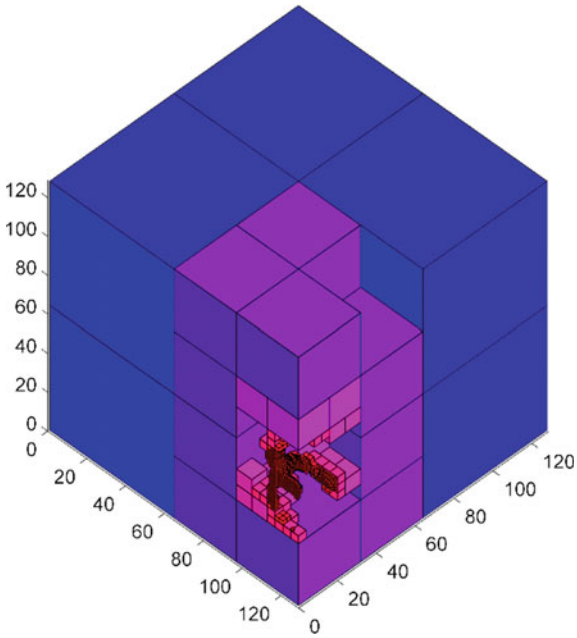

Fig. 19 Porous micro-structure adaptive model for curvature based ROI selection criterion (Color figure online)

The first is the dependency of the resulted model in the initial orientation of the model, meaning that the same object in different orientations will have different results due to the traversal order on the data structure. In addition, even though a topological preservation method is implemented, there are cases in which the topology will not be completely preserved.

References

1. Samet H (1990) The design and analysis of spatial data structures. Addison-Wesley, Reading, MA
2. Samet H (2006) Foundations of multidimensional and metric data structures. Morgan Kaufmann
3. Podshivalov L, Fischer A, Bar-Yoseph PZ (2011) 3D hierarchical geometric modeling and multiscale FE analysis as a base for individualized medical diagnosis of bone structure. Bone 48(4):693–703
4. Gargantini I (1982) An effective way to represent quadtrees. Commun ACM 25(12):905–910
5. Jia X, Wang D, Wu Y, Luo X (2010) A shrinking algorithm for binary images to preserve topology. In: 2010 3rd international congress on image and signal processing (CISP). IEEE, pp 1181–1185
6. Whalen D (2012) A topology-preserving voxelization shrinking algorithm. In: Proceedings of bridges 2012: mathematics, music, art, architecture, culture. Tessellations Publishing, pp 523–524
7. Podshivalov L, Fischer A, Bar-Yoseph PZ (2011) Multiscale FE method for analysis of bone micro-structures. J Mech Behav Biomed Mater 4(6):888–899

8. Podshivalov L, Gomes CM, Zocca A, Guenster J, Bar-Yoseph P, Fischer A (2013) Design, analysis and additive manufacturing of porous structures for biocompatible micro-scale scaffolds. Procedia CIRP 5:247–252
9. Yizhak Ben Shabat AF (2013) Adaptive hierarchical multi resolution volumetric geometric modeling. Technion
10. Shabat YB, Fischer A (2014) Design of adaptive porous micro-structures for additive manufacturing. In: 24th CIRP design conference, vol 21, pp 133–137
11. Lorensen WE, Cline HE (1987) Marching cubes: a high resolution 3D surface construction algorithm. ACM, ACM Siggraph Comput Graph, pp 163–169
12. Desbrun M, Meyer M, Schröder P, Barr AH (1999) Implicit fairing of irregular meshes using diffusion and curvature flow. In: Proceedings of the 26th annual conference on computer graphics and interactive techniques. ACM Press/Addison-Wesley Publishing Co., pp 317–324
13. Rusinkiewicz S (2004) Estimating curvatures and their derivatives on triangle meshes. In: Proceedings of the 2nd international symposium on 3D data processing, visualization and transmission, 2004. 3DPVT 2004. IEEE, pp 486–493
14. Kong TY, Rosenfeld A (1989) Digital topology: introduction and survey. Comput Vis Graph Image Process 48(3):357–393

Low Temperature 3D Printing of Drug Loaded Bioceramic Scaffolds and Implants

Susanne Meininger, Elke Vorndran, Miguel Castilho, Paulo Rui Fernandes and Uwe Gbureck

Abstract 3D powder printing (3DP) enables the fabrication of porous scaffolds with anisotropic aligned pores for bone tissue engineering and for the fabrication of custom made implants for cranio-maxillofacial surgery. By combining 3D printing and self-setting biocement matrices, a low temperature processing chain can be established for a simultaneous spatial control over both structure geometry and composition by using multi-colour printers. This contribution aims to highlight bioceramic material approaches in order to fabricate scaffolds and implants by 3DP with a special emphasis on the drug modification of such structures.

Keywords Bioceramics · 3D powder printing · Multi-colour printing · Bone implants · Drug delivery systems · Bone regeneration

1 Introduction

Additive manufacturing (AM) techniques are considered to be suitable methods to produce tissue replacement materials with a complex internal or external structure based on prefabricated structure designs or patient specific computer tomography data [1, 2]. The underlying principle of AM is a layerwise fabrication of near net shape structures by spatial control of material bonding with methods such as stereolithography [3], fused deposition modelling [4], 3D powder printing [5–10], 3D plotting [11, 12], melt electrospinning writing (MEW) [13, 14] or selective laser sintering [15]. Such generated structures may either directly serve as patient specific implants (PSI) or they can be used as porous scaffolds with aligned pores for

S. Meininger · E. Vorndran · U. Gbureck (✉)
Department of Functional Materials in Medicine and Dentistry, University of Würzburg, Würzburg, Germany
e-mail: uwe.gbureck@fmz.uni-wuerzburg.de

M. Castilho
Department of Orthopedics, University Medical Center Utrecht, Utrecht, The Netherlands

P. R. Fernandes
IDMEC, Instituto Superior Técnico, Universidade de Lisboa, Lisbon, Portugal

P. R. Fernandes and P. J. da Silva Bartolo (eds.), *New Developments in Tissue Engineering and Regeneration*, Computational Methods in Applied Sciences 51,
https://doi.org/10.1007/978-3-030-15372-4_4

guided tissue ingrowth. Materials processed by AM cover a broad range from pure metals [16], polymers [17], ceramics [18] or composites [19, 20], whereas every AM method requires specific material properties for processing.

A major application site for PSI prepared by AM are large sized bone defects predominantly in the cranio-maxillofacial area [21]. Bone is a highly hierarchical and slowly growing tissue with only a limited self-healing capacity, whereas in humans defects above a critical size of approximately 10 mm show no bony regeneration but the ingrowth of fibrous tissue [22]. Here, it is essential that the scaffold simulates natural bone tissue growth by providing adequate composition, morphology, structure, and mechanical properties. According to Karageorgiou et al. the main criteria for this purpose are sufficient mechanical strength within the range of cancellous bone as well as a highly interconnected porosity of at least 50% with pore sizes between 100 and 800 μm, whereas pore characteristics (size, interconnectivity) are predominant parameters for nutrient exchange and cell ingrowth [23]. Since bone is a highly mineralized tissue with approx. 70 wt% hydroxyapatite as inorganic component, manufacturing approaches for bone scaffolds and implants usually comprise calcium phosphate compounds (e.g. hydroxyapatite, tricalcium phosphate, brushite) to mimic the bone ionic composition. Scaffold preparation either involves the fabrication of a green ceramic structure by the aid of polymeric binders, which are burnt out afterwards, or low temperature self-setting cement powder and pastes can be applied to avoid sintering and to produce hydrated calcium phosphate phases [6, 9, 17]. The latter is only possible by using non-thermal AM procedures (e.g. 3D plotting or printing), whereas the absence of heat enables the simultaneous deposition of drugs [24] or even living cells [25] within the scaffold.

This contribution aims to highlight material approaches to fabricate bioceramic scaffolds and implants by 3D printing with a special emphasis on the drug modification of such structures. The 3D powder printing technology enables the fabrication of porous scaffolds with anisotropically aligned pores in the sub millimeter range and has gained increasing attention for the fabrication of scaffolds for bone tissue engineering and custom made implants for cranio-maxillofacial surgery. Since 3D printing is a low temperature procedure it enables in addition a simultaneous spatial control over both structure geometry and composition by using multi-colour printers in conjunction with low temperature self-setting ceramic matrices.

2 3D Printing Technology

3D powder printing (3DP) is an attractive technology due to its rapid and inexpensive model making ability in technical or medical applications, e.g. for the fabrication of casting moulds [26] or biodegradable and osteoactive implants [10, 27–31]. The 3D powder printing technique forms a 3-dimensional structure based on thin powder layers and a binding agent, which is locally sprayed onto the powder leading to a localised solidification of the powder particles [32, 33]. The solidification process can be either induced by a physical mechanism (e.g. organic liquid, swelling or partial

dissolution of polymeric additives, phase changes) or by a chemical reaction (e.g. hydraulic cement setting, acid-base reaction). A detailed description of the different hardening possibilities during 3DP can be found in literature [34]. Although the reactive binding component is often distributed in the powder and the printing liquid only starts the binding process, the printing liquid will be denominated as "binder" within this article.

The general underlying principle of 3DP is demonstrated in Fig. 1a. In a first step, a thin and smooth layer of powder is prepared in the building chamber by a counter-clockwise rotating roller transferring powder from the reservoir to the printing bed in a defined layer thickness. Secondly, the print head locally sprays the binder on the powder surface such that the first layer of the implant structure is printed surrounded by unreacted powder. After this the roller moves back, the powder reservoir lifts up by the thickness of one layer and the roller moves another powder layer to the printing bed which is at the same time lowered by one layer thickness. The second printed layer of the structure is created on top of the first one and both layers stick together by binder diffusion due to capillary forces of the powder bed. This process repeats until all of the layers of the sample are printed. The samples are then removed from the printing bed and cleaned from residual unreacted powder. Cleaning is commonly performed by blowing air, whereas the surface finish of the printed part can be improved by vibration with the addition of smaller particles. While cleaning of the outer surface is relatively easy, the removal of loose powder particles from the inner part (e.g. small pores <500 μm intended for blood vessel ingrowth) is much more demanding and may require additionally wet methods such as ultrasonication or microwave assisted boiling of the sample [35]. However, these procedures are only possible in liquids which do not dissolve the binder to avoid mechanical disintegration of the printed sample. An approach for an improved depowdering of porous implants suggested by Butscher et al. [36] is based on the design of an outer cage with windows, which are large enough to enable depowdering, but at the same time can trap loosely bound (3D printed) filler particles in the inside of the implant. Since the initial strength of the printed parts is in most cases relatively low, a post-processing regime is commonly applied to increase strength, e.g. by polymer infiltration [37], repeated immersion in binder liquid for hydraulic setting systems [9] or sintering [38]. Generally, it has to be taken into account that the 3DP process is an anisotropic manufacturing process due to the layer wise preparation of thin powder layers by a roller. This means that the final size of the printed structure may also show an anisotropic deviation from the theoretical values and this also applies for other properties such as the mechanical strength [39, 40].

Commercially available 3D powder printing systems (e.g. Z-Corp systems) commonly use thermally working drop-on-demand print-heads (Fig. 1b, c), in which the binder droplets (approx. 30 picoliter in volume [41]) are created in thin nozzles and ejected by a steam bubble formed by thermal evaporation of the binder liquid. Such thermal print heads are comparatively cheap, but problems may occur if either the binding liquid dries within the nozzles or solids are precipitated during binder evaporation, both leading to a clogging of the nozzles and hence a reduction of print head life time and printing quality. An alternative is the use of piezoelectric print

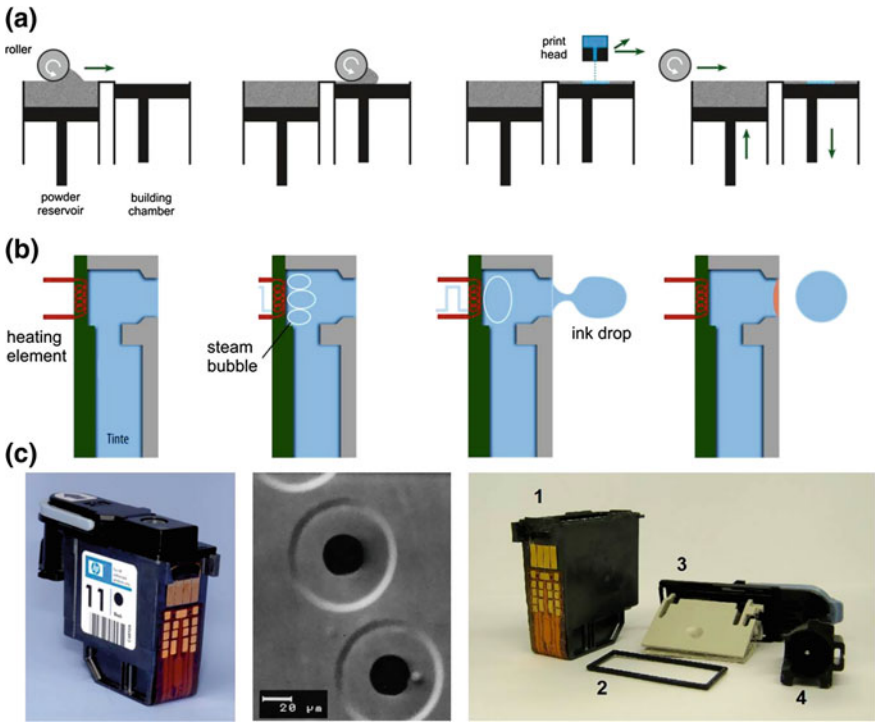

Fig. 1 **a** Fabrication steps for additive manufacturing of a sample by 3D printing. 1–2: a roller transfers a thin powder layer to the building room, 3: localised application of binder liquid leads to spatially controlled hardening of the powder. 4: repetition of 1–3 results in the fusion of the printed layers and the formation of a three dimensional object. **b** Thermally working print-head, which ejects droplets through a nozzle by binder evaporation. **c** Left: commercially available print-head (used in ZCorp Printers), middle: SEM of print-head nozzles, right: single parts of the print-head

heads, which form the binder drops by the sudden volume change of a piezoelectric material, which causes an acoustic pulse and hence forms an ink-droplet in the nozzle [42].

Printing systems are nowadays available from various companies enabling the fabrication of samples spanning from the millimeter to the meter range [43]. Worth to note is, that all commercial 3D powder printers (including materials) up to now are designed for civil engineering purpose, their use in biomedical engineering is sometimes difficult due to the special requirements (e.g. cleaning, sterilization etc.) of this field. Similar, most of the commercially available print heads for 3DP systems stem from ordinary ink jet printers and are hence filled with ink, which has to be carefully removed prior to use. Even small ink residues within the print head may also lead to clogging of the nozzles when using experimental binder liquids, in addition any ink contamination of the fabricated samples may have a detrimental effect on the biocompatibility.

3 Material Approaches to 3D Powder Printing of Ceramic Bone Scaffolds

3D powder printed samples are characterized by a high microporosity >30 vol.%, which is a result from the voids between the loosely packed powder particles during the fabrication process. This microporosity is beneficial since it enables nutrients diffusion to support cell ingrowth and vascularization into larger sized macropores with sizes of a few 100 μm [20, 44]. Many recent studies have dealt with the adaption of the 3D printing process to the fabrication of bone substitutes from calcium phosphate based powders such as hydroxyapatite (HA) [45, 46], ß-tricalcium phosphate (β-TCP) [47, 48], biphasic HA/β-TCP mixtures (BCP) [49, 50], β-TCP/calcium pyrophosphate ceramics [51], calcium polyphosphates [52] or brushite [9]. Most of the investigated material systems require a final sintering step for binder burn out and densification of the ceramic. This usually results in the formation of a microcrystalline texture and—in case of hydroxyapatite—practically insoluble implants. Direct printing of more soluble nanocrystalline hydroxyapatite (HA) similar to the mineral phase of bone (e.g. by a cement setting reaction to avoid sintering) is difficult and would require the use of polymeric additives to control liquid binder localisation over a long time period. The reason for this is the low crystal growth rate of HA leading to a low reactivity between solid and liquid during printing. Preferably, 3D printing of nanoscale HA samples is performed in a two-step regime, in which first the sample is fabricated using a fast setting reaction (e.g. brushite formation or use of calcium sulphate powders), followed by a hydrothermal treatment of the finished part to transform it into HA without change of size and shape [8, 27, 30].

A general requirement for powders used for 3D printing is a sufficient flowability to form thin powder layers with a smooth surface to obtain high printing quality. This property is associated with the particle size distribution of the powder. It has been demonstrated that ideal particle sizes for 3D powder printing are in the range of 15–35 μm [7, 53, 54]. Larger particles in the size range of the individual powder layer thickness (80–150 μm) may interfere with printing quality similar to small particle fractions <5 μm, which build up large sized agglomerates in the millimeter range. An approach to improve the powder flowability and hence the quality of the powder surface is based on a plasma coating of the particles with SiO_x nanoparticles as demonstrated by Butscher et al. [7]. These nanoparticles act as spacer between the larger size powder particles and hence reduce attractive van der Waals forces. The printing quality can also be increased by a controlled humidification of the powder surface prior to printing. This is thought to stabilize the loosely packed particles to avoid movement of the particle layer (and hence the printed sample) during recoating with the next powder layer. Indeed, it was demonstrated that for a low layer thickness of 44 μm, applied moisture had a strong positive effect on geometrical sample accuracy, especially when only a small number of samples was simultaneously printed [5].

Since the binder liquid is sprayed onto a porous powder bed, also a rapid hardening reaction is necessary to reduce uncontrolled binder spreading due to capillary

forces and to ensure high printing quality. Such hardening reactions can be based on different mechanisms as described above, whereas cement setting reaction offer the advantage of a low temperature processing regime to produce hydrated ceramics (e.g. brushite) and to simultaneously deposit organic drugs within the printed matrix. Suitable biocements are based on reactive calcium phosphate powders (e.g. TTCP or α-TCP), which react during printing with acidic phosphate solutions to form a matrix of secondary calcium phosphates in a fast dissolution—precipitation reaction:

$$Ca_3(PO_4)_2 + H_3PO_4 + 6H_2O \rightarrow 3CaHPO_4 \cdot 2H_2O$$

The high reactivity leads to a rapid setting and solidification within seconds and mostly prevents undesired binder spreading such that macropores down to a size of approx. 300–400 μm can be printed within a structure (Fig. 2). Since the degree of conversion during printing is small, commonly a post-hardening regime by short immersion cycles in binder liquid are applied to increase both the amount of brushite formed in the sample as well as the mechanical performance. Following this, compressive strength of up to 22 MPa can be obtained [9]. An alternative setting reaction was recently described by Mandal et al. [55], who used diluted phytic acid solution as binder liquid, which formed calcium chelates with tetracalcium phosphate powder during 3D printing. This approach was beneficial since the printed structured did not convert into low soluble hydroxyapatite during prolonged immersion in physiological solution. The strength of 3D printed samples can be generally increased by polymer impregnation, which can be either performed during the printing process or post printing [56].

3D printed calcium phosphate structures were demonstrated to have an excellent biocompatibility both under in vitro [53, 57] and in vivo conditions [20, 58–61]. Klammert et al. could prove the biocompatibility of printed brushite/monetite scaffolds in an osteoblastic cell culture model [57] with an application in bone replacement by printing highly accurate craniofacial implants [21]. The biocompatibility and osteoconductivity of such printed implants was confirmed in vivo by Habibovic et al. after implantation in bone in a sheep model [58]. Surprisingly, the same authors were also able to demonstrate that the materials were at the same time osteoinductive leading to the formation of bone after intramuscular implantation. Cell-biological aspects of 3D printed implant resorption were investigated by Detsch et al. [53] by seeding the macrophage cell line RAW 264.7 on 3D printed HA, β-TCP and BCP surfaces. All such materials promoted the differentiation of macrophage precursor cells into bone-resorbing osteoclast-like cells, whereas a 60:40 mixture of HA and β-TCP showed the most promising results regarding cell growth, differentiation and hence material degradation. The latter can also be adjusted by post-processing of 3D printed samples, e.g. by autoclaving brushite to form monetite ($CaHPO_4$). Monetite ceramics show an enhanced in vivo degradation profile [9, 62], likely because of the absence of a phase transformation into a lower soluble HA phase in vivo. A veterinary application of 3D printed brushite samples was investigated by Castilho et al. [63], who fabricated a customized calcium phosphate implant (composed of

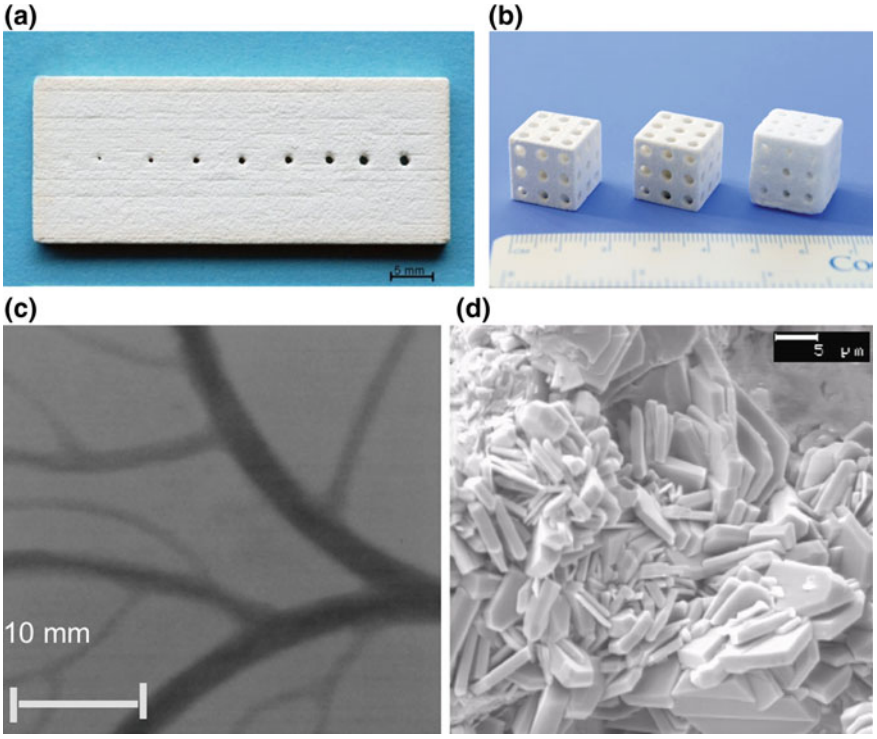

Fig. 2 **a**, **b** Examples of 3D printed macroporous brushite samples, **c** X-ray micrograph of a branched pore system in a sample and **d** microstructure of the samples after 3 × 30 s post hardening in 20% phosphoric acid

brushite, monetite and tricalcium phosphate) for canine cruciate ligament treatment by tibial tuberosity advancement in dogs (Fig. 3).

The implant was designed using a suitable topology optimization methodology in order to maximize permeability due to an overall porosity of 59.2%. The latter was achieved by the combination of process-immanent microporosity of approximately 40% and a designed interconnected macroporous network with pore sizes of 845 µm. The mechanical properties of such printed implants were in the range of trabecular bone enabling complete restoration of the dog's limb function without any adverse complications.

4 Drug Modification of 3D Printed Implants

Drug delivery systems (DDS) are designed for the controlled release of bioactives directly into a defined target tissue and to maintain a sufficient therapeutic level of the drug over a defined period of time. This should avoid risks of a systemic

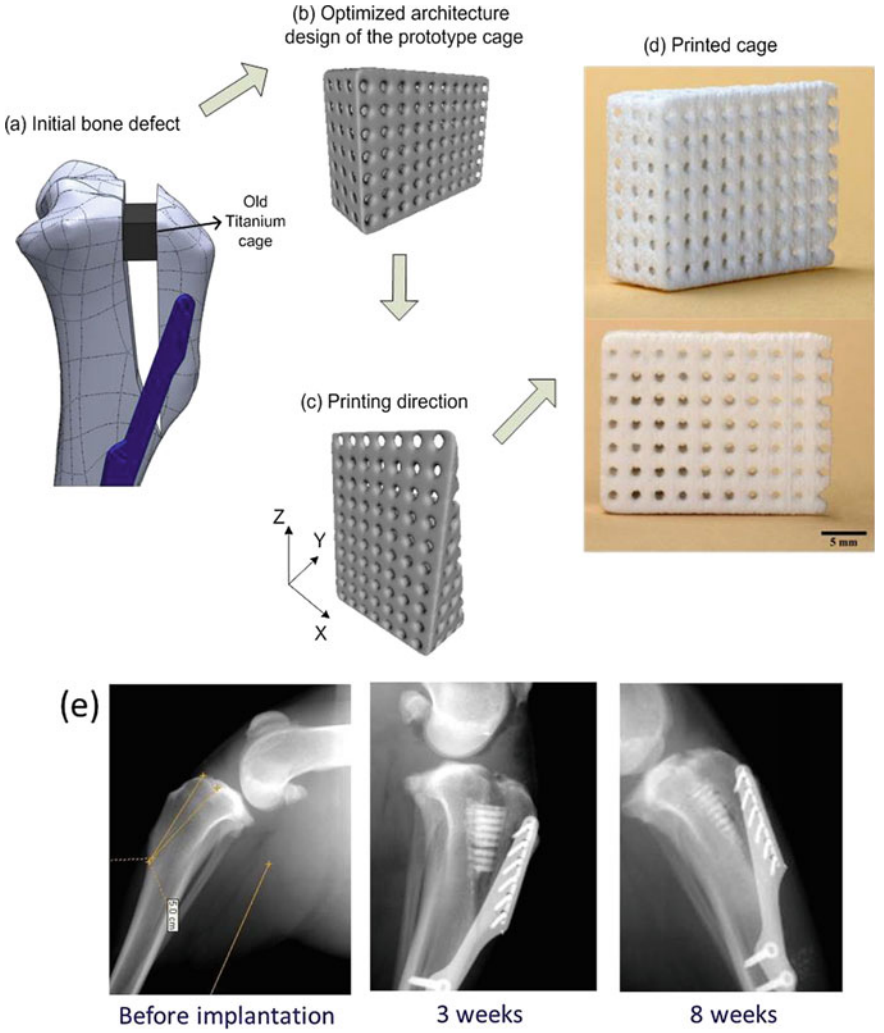

Fig. 3 **a**–**d** Fabrication regime of a calcium phosphate cage resulting from the periodic repetition of an optimized unit cell with 1000 μm macropore size; **e** X-ray micrographs of the implanted cage in the dog left stifle joint after different time intervals post operatively. Unpublished images from Ref. [63]

drug application, especially side effects due to a high plasma concentration, a low bioavailability resulting from low blood supply or biological barriers of target tissue, or an elimination or inactivation of the drug during in vivo transport [64]. Common modifications in the area of bone tissue regeneration include bioactives to induce angiogenesis or osteogenesis [65], chemotherapeutical agents to treat cancer [66] or antibiotics for infection treatment or prophylaxis [67]. Recent developments concern the use of microporous 3D printed CaP-scaffolds as drug carriers. Drug modification is possible by immersion of the porous ceramic scaffolds in an aqueous drug solution leading to a homogeneous distribution of the drug within the scaffold structure [68–70]. The adsorption behaviour and the release kinetic of antibiotics on different printed calcium phosphate matrices (brushite, monetite, hydroxyapatite) are predominantly determined by physical properties like porosity and specific surface area of the matrices or drug-matrix interactions [68]. Commonly, a quantitative release within 2 days was observed due to the microporosity with pore sizes in the range of 10–15 μm. A sustained release was achieved by infiltration of the DDS with a degradable polymer [68]. Later, an in vivo study showed, that simultaneous manual application of BMP-2 within a 3D printed biphasic calcium phosphate scaffold enhance bone growth compared to unloaded or to scaffolds with a delayed BMP application [70, 71].

A more sophisticated approach to create DDS by additive manufacturing is the use of multiphase-printers [72], which enable the simultaneous processing of different materials in one scaffold. An example are multicolour-3D printers, in which the colour information can be used to deposit bioactive compounds at desired locations in the 3D scaffolds for a spatial control of drug release kinetics and tissue response. For this process, drugs will be dissolved or dispersed in a solution and printed within defined areas of the scaffold, whereas the solutions have to be adjusted to gain optimal printability [73]. This was firstly demonstrated by Wu et al. [74], who controlled the release rate of dyes (methylene blue and alizarin yellow) as model drug from polymers (polycaprolactone, polyethylene oxide) by adjusting the local drug concentration and matrix composition. The authors demonstrated that 3D printing is not limited to adjust only zero order release kinetics but can also produce multiple diffusion gradients within a single device to create more complicated drug release profiles not easily achieved with conventional processing techniques [68]. Following studies dealt with the fabrication of polymeric DDS with controlled release patterns of single or multiple drugs [75, 76], e.g. by printing multilayer concentric cylinders, in which each layer can be loaded with a specific drug to obtain an orderly release profile from the outside to the center of the DDS with peak concentrations at 8–12 days intervals. Bone tuberculosis treatment by loading the printed DDS with either isoniazid or rifampicin was discussed to be an application [76]. Another study by Yu et al. investigated the release behaviour of acetaminophen from depot loaded ethylcellulose tablets. Release-retarding material gradients and drug-free diffusion barriers were utilized to gain a constant release rate over a period of 5–13 h governed by matrix erosion and diffusion process [75].

An application of this concept to ceramic bone implants used a commercially available multi-colour printer for sample preparation [24], in which the black chan-

nel was used for applying the binder, while the other three channels were filled with solutions containing either BMP-2, vancomycin, heparin as drugs or a chitosan solution to produce either homogeneous, depot or gradient drug loadings (Fig. 4a). A spatial resolution of approximately 300 μm of the drugs within the matrix was achieved by using a cellulose modified tricalcium phosphate powder. Drug release kinetics were shown to depend on the drug localisation within the scaffolds; while homogeneously loaded scaffolds provided first order release kinetics, drug depots or gradients resulted in zero order release over a period of 3–4 days with release rates in the range 0.68–0.96%/h (Fig. 4b).

A crucial prerequisite for such 3D printed DDS is that the pharmacological activity of imprinted drugs is maintained until final release. This is somewhere challenging since the fabrication regime includes harsh conditions, e.g. (1) parts of the binder solution are thermally evaporated during printing, (2) high shear forces occur during bubble ejection or (3) the acid pH during setting of the above mentioned brushite cement matrix. While (1) and (2) seemed to have only a minor effect on drug activity (demonstrated by purging the solutions through the print-heads without cement matrix), (3) seemed to be a parameter diminishing the activity of delicate protein based factors. Indeed, only for pH insensitive drugs like vancomycin it was possible to demonstrate more or less unchanged activity after the whole process chain and release from the brushite matrix (Fig. 5a). A solution to this problem might be the use of neutral setting cements for 3D printing based on the formation of struvite ($MgNH_4PO_4 \cdot 6H_2O$) from magnesium phosphate powder and ammonium phosphate solution. Indeed, by using this approach it was possible to measure a certain BMP-2 activity after printing and release, however the determined activities were quite low compared to the activity of the used binder solution (Fig. 5b) [77]. This is thought to be a result of the quite low porosity of struvite cements (5–7% according to [78]), which may have led to a physical entrapment of the drug within the matrix.

5 Conclusion

3D powder printing of ceramic implants and scaffolds enables the fabrication of patient specific implants or macroporous scaffolds from a broad range of materials. The possibility to perform the process at room temperature by using self-setting ceramic bone cements offers the possibility for a simultaneous control over geometry, porosity and composition. Such cements are hydrated phases of calcium or magnesium phosphates (brushite, monetite, struvite) with an enhanced degradation ability compared to traditionally used sintered materials such as hydroxyapatite or tricalcium phosphate. The progress in developing low temperature rapid prototyping systems using a cement setting reaction may open the possibility to fabricate scaffolds of different compositions (ceramic, hydrogel) which are simultaneously loaded with bioactives to control release profile and cellular response. Clearly, such a fabrication chain of drug loaded samples would require a processing under sterile conditions since common sterilisation procedures (heat, γ-irradiation) may negatively affect the

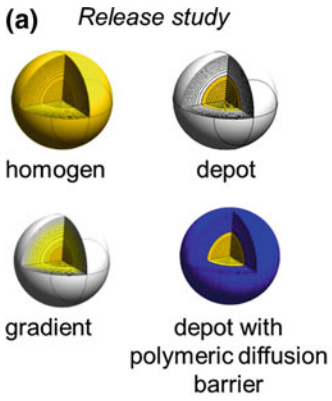

binder application [%]				colour code
Cyan (print-head 3)	Magenta (print-head 2)	Yellow (print-head 1)	White (print-head 0)	
bioactive 3	bioactive 2	bioactive 1	binder	
-	-	-	100	white
-	-	85	15	yellow
-	18	-	82	magenta
11	-	-	89	cyan
34	12	-	54	blue
	31	53	16	red
8	-	23	69	green
33	35	31	1	black

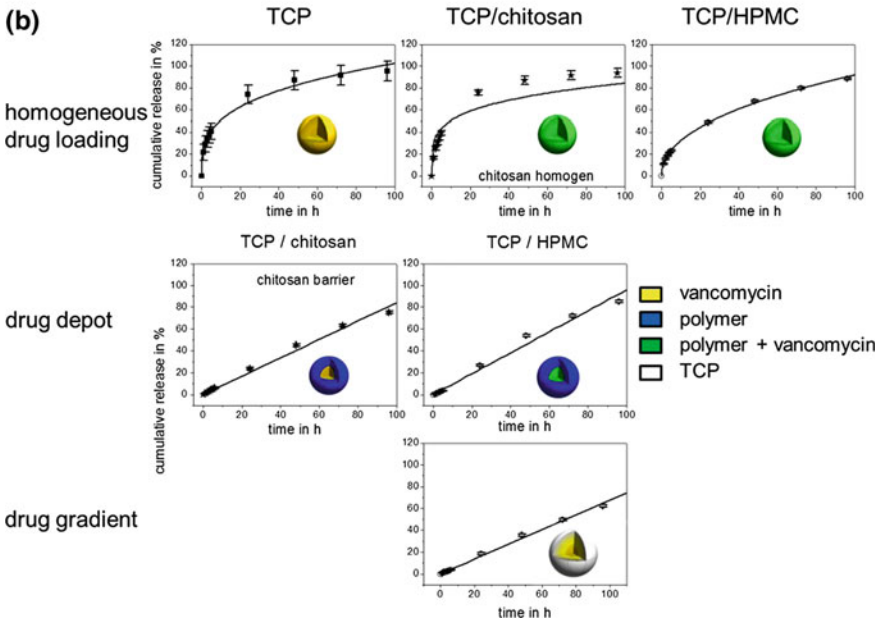

Fig. 4 **a** Spherical bioceramic samples prepared by 3D powder printing with either homogeneous, depot or graded drug loading. Hardening of samples is achieved by printing binder solution (H_3PO_4) with the black print-head, while localized deposition of drugs is achieved by additional print-heads based on the colour information of each sample. **b** Vancomycin release kinetics from brushite samples in PBS buffer over a course of 4 days [24]. The ceramic spheres were printed with TCP powder, partially mixed with hydroxymethyl propyl cellulose (HPMC), and phosphoric acid as binder. The vancomycin or chitosan was locally incorporated within the samples by spraying of the antibiotic or chitosan solution through a print head (Color figure online)

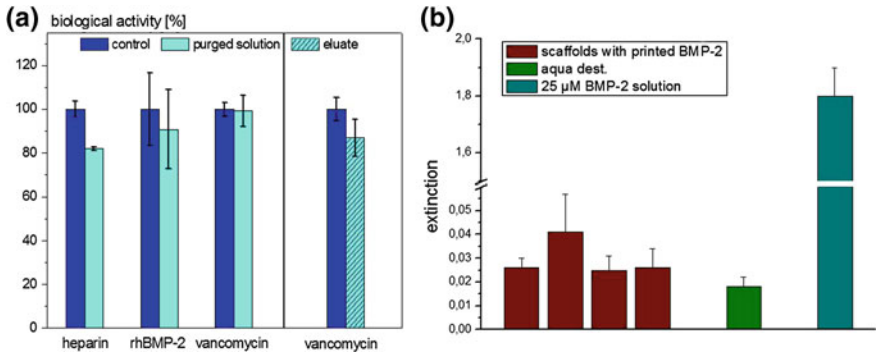

Fig. 5 **a** Pharmaceutical activity of drugs after applying through the print-head and after the whole process chain; matrix: brushite from TCP powder and phosphoric acid as binder [24]; **b** BMP-2 activity after release from a neutral pH setting struvite matrix [77] (Color figure online)

pharmacological activity of many imprinted drugs. Engineering suitable and reliable printers for sterile processing is likely the next step in the fabrication and clinical application of drug or cell loaded ceramic implants.

Acknowledgements Paulo Rui Fernandes would like to thank to Fundação para a Ciência e Tecnologia (Portugal) for the support through project PTDC/BBB-BMC/5655/2014 and LAETA project UID/EMS/50022/2019.

References

1. Vorndran E, Moseke C, Gbureck U (2015) 3D printing of ceramic implants. MRS Bull 40:127–136
2. Garrett B (2014) 3D printing: new economic paradigms and strategic shifts. Glob Policy 5:70–75
3. Melchels FPW, Feijen J, Grijpma DW (2010) A review on stereolithography and its applications in biomedical engineering. Biomaterials 31:6121–6130
4. Teo EY, Ong SY, Chong MSK, Zhang ZY, Lu J, Moochhala S et al (2011) Polycaprolactone-based fused deposition modeled mesh for delivery of antibacterial agents to infected wounds. Biomaterials 32:279–287
5. Butscher A, Bohner M, Doebelin N, Galea L, Loeffel O, Muller R (2013) Moisture based three-dimensional printing of calcium phosphate structures for scaffold engineering. Acta Biomater 9:5369–5378
6. Butscher A, Bohner M, Hofmann S, Gauckler L, Muller R (2011) Structural and material approaches to bone tissue engineering in powder-based three-dimensional printing. Acta Biomater 7:907–920
7. Butscher A, Bohner M, Roth C, Ernstberger A, Heuberger R, Doebelin N et al (2012) Printability of calcium phosphate powders for three-dimensional printing of tissue engineering scaffolds. Acta Biomater 8:373–385
8. Suwanprateeb J, Suvannapruk W, Wasoontararat K (2010) Low temperature preparation of calcium phosphate structure via phosphorization of 3D-printed calcium sulfate hemihydrate based material. J Mater Sci Mater Med 21:419–429

9. Gbureck U, Hozel T, Klammert U, Wurzler K, Muller FA, Barralet JE (2007) Resorbable dicalcium phosphate bone substitutes prepared by 3D powder printing. Adv Func Mater 17:3940–3945
10. Leukers B, Gulkan H, Irsen SH, Milz S, Tille C, Schieker M et al (2005) Hydroxyapatite scaffolds for bone tissue engineering made by 3D printing. J Mater Sci Mater Med 16:1121–1124
11. Luo YX, Lode A, Akkineni AR, Gelinsky M (2015) Concentrated gelatin/alginate composites for fabrication of predesigned scaffolds with a favorable cell response by 3D plotting. RSC Adv 5:43480–43488
12. Luo YX, Lode A, Sonntag F, Nies B, Gelinsky M (2013) Well-ordered biphasic calcium phosphate-alginate scaffolds fabricated by multi-channel 3D plotting under mild conditions. J Mater Chem B 1:4088–4098
13. Brown TD, Edin F, Detta N, Skelton AD, Hutmacher DW, Dalton PD (2014) Melt electrospinning of poly(epsilon-caprolactone) scaffolds: phenomenological observations associated with collection and direct writing. Mater Sci Eng C Mater Biol Appl 45:698–708
14. Mota C, Puppi D, Gazzarri M, Bartolo P, Chiellini F (2013) Melt electrospinning writing of three-dimensional star poly(E-caprolactone) scaffolds. Polym Int 62:893–900
15. Sadeghian Z, Heinrich JG, Moztaradeh F (2004) Direct laser sintering of hydroxyapatite implants by layer-wise slurry deposition (LSD). CFI-Ceramic Forum Int 81:E39–E43
16. Ryan GE, Pandit AS, Apatsidis DP (2008) Porous titanium scaffolds fabricated using a rapid prototyping and powder metallurgy technique. Biomaterials 29:3625–3635
17. Hutmacher DW (2001) Scaffold design and fabrication technologies for engineering tissues—state of the art and future perspectives. J Biomater Sci Polym Ed 12:107–124
18. Legeros RZ, Lin S, Rohanizadeh R, Mijares D, Legeros JP (2003) Biphasic calcium phosphate bioceramics: preparation, properties and applications. J Mater Sci Mater Med 14:201–209
19. Bakarich SE, Gorkin R, Panhuis MIH, Spinks GM (2014) Three-dimensional printing fiber reinforced hydrogel composites. ACS Appl Mater Interfaces 6:15998–16006
20. Inzana JA, Olvera D, Fuller SM, Kelly JP, Graeve OA, Schwarz EM et al (2014) 3D printing of composite calcium phosphate and collagen scaffolds for bone regeneration. Biomaterials 35:4026–4034
21. Klammert U, Gbureck U, Vorndran E, Rodiger J, Meyer-Marcotty P, Kubler AC (2010) 3D powder printed calcium phosphate implants for reconstruction of cranial and maxillofacial defects. J Cranio Maxillofac Surg 38:565–570
22. Aaboe M, Pinholt EM, Hjortinghansen E (1995) Healing of experimentally created defects—a review. Br J Oral Maxillofac Surg 33:312–318
23. Karageorgiou V, Kaplan D (2005) Porosity of 3D biomaterial scaffolds and osteogenesis. Biomaterials 26:5474–5491
24. Vorndran E, Klammert U, Ewald A, Barralet JE, Gbureck U (2010) Simultaneous immobilization of bioactives during 3D powder printing of bioceramic drug-release matrices. Adv Func Mater 20:1585–1591
25. Lode A, Krujatz F, Bruggemeier S, Quade M, Schutz K, Knaack S et al (2015) Green bioprinting: fabrication of photosynthetic algae-laden hydrogel scaffolds for biotechnological and medical applications. Eng Life Sci 15:177–183
26. Vorndran E, Wunder K, Moseke C, Biermann I, Muller FA, Zorn K et al (2011) Hydraulic setting $Mg_3(PO_4)_2$ powders for 3D printing technology. Adv Appl Ceram 110:476–481
27. Seitz H, Rieder W, Irsen S, Leukers B, Tille C (2005) Three-dimensional printing of porous ceramic scaffolds for bone tissue engineering. J Biomed Mater Res Part B Appl Biomater 74B:782–788
28. Leukers B, Gulkan H, Irsen SH, Milz S, Tille C, Seitz H et al (2005) Biocompatibility of ceramic scaffolds for bone replacement made by 3D printing. Materialwiss Werkstofftech 36:781–787
29. Gbureck U, Holzel T, Doillon CJ, Muller FA, Barralet JE (2007) Direct printing of bioceramic implants with spatially localized angiogenic factors. Adv Mater 19:795–+
30. Gbureck U, Holzel T, Thull R, Muller FA, Barralet JE (2006) Preparation of nanocrystalline hydroxyapatite scaffolds by 3D powder printing. Cytotherapy 8:14

31. Bergmann C, Lindner M, Zhang W, Koczur K, Kirsten A, Telle R et al (2010) 3D printing of bone substitute implants using calcium phosphate and bioactive glasses. J Eur Ceram Soc 30:2563–2567
32. Bose S, Vahabzadeh S, Bandyopadhyay A (2013) Bone tissue engineering using 3D printing. Mater Today 16:496–504
33. Hwa LC, Rajoo S, Noor AM, Ahmad N, Uday MB (2017) Recent advances in 3D printing of porous ceramics: a review. Curr Opin Solid State Mater Sci 21:323–347
34. Kumar A, Mandal S, Barui S, Vasireddi R, Gbureck U, Gelinsky M et al (2016) Low temperature additive manufacturing of three dimensional scaffolds for bone-tissue engineering applications: processing related challenges and property assessment. Mater Sci Eng R Rep 103:III-39
35. Sachs EM CM, Bredt JF (1996) Process for removing loose powder particles from interior passages of a body. United States: U.S. Patent and Trademark Office. Massachusetts Institute of Technology, pp 5, 490, 882
36. Butscher A, Bohner M, Doebelin N, Hofmann S, Muller R (2013) New depowdering-friendly designs for three-dimensional printing of calcium phosphate bone substitutes. Acta Biomater 9:9149–9158
37. Suwanprateeb J, Sanngam R, Suwanpreuk W (2008) Fabrication of bioactive hydroxyapatite/bis-GMA based composite via three dimensional printing. J Mater Sci Mater Med 19:2637–2645
38. Winkel A, Meszaros R, Reinsch S, Muller R, Travitzky N, Fey T et al (2012) Sintering of 3D-printed glass/HAp composites. J Am Ceram Soc 95:3387–3393
39. Castilho M, Dias M, Gbureck U, Groll J, Fernandes P, Pires I et al (2013) Fabrication of computationally designed scaffolds by low temperature 3D printing. Biofabrication 5
40. Meininger S, Mandal S, Kumar A, Groll J, Basu B, Gbureck U (2016) Strength reliability and in vitro degradation of three-dimensional powder printed strontium-substituted magnesium phosphate scaffolds. Acta Biomater 31:401–411
41. Creagh LT, McDonald M (2003) Design and performance of inkjet print heads for non-graphic-arts applications. MRS Bull 28:807–811
42. de Gans BJ, Duineveld PC, Schubert US (2004) Inkjet printing of polymers: state of the art and future developments. Adv Mater 16:203–213
43. Lu K, Reynolds WT (2008) 3DP process for fine mesh structure printing. Powder Technol 187:11–18
44. Boyan BD, Hummert TW, Dean DD, Schwartz Z (1996) Role of material surfaces in regulating bone and cartilage cell response. Biomaterials 17:137–146
45. Will J, Melcher R, Treul C, Travitzky N, Kneser U, Polykandriotis E et al (2008) Porous ceramic bone scaffolds for vascularized bone tissue regeneration. J Mater Sci Mater Med 19:2781–2790
46. Suwanprateeb J, Sanngam R, Panyathanmaporn T (2010) Influence of raw powder preparation routes on properties of hydroxyapatite fabricated by 3D printing technique. Mater Sci Eng C Mater Biol Appl 30:610–617
47. Fielding GA, Bandyopadhyay A, Bose S (2012) Effects of silica and zinc oxide doping on mechanical and biological properties of 3D printed tricalcium phosphate tissue engineering scaffolds. Dent Mater 28:113–122
48. Vorndran E, Klarner M, Klammert U, Grover LM, Patel S, Barralet JE et al (2008) 3D powder printing of beta-tricalcium phosphate ceramics using different strategies. Adv Eng Mater 10:B67–B71
49. Castilho M, Moseke C, Ewald A, Gbureck U, Groll J, Pires I et al (2014) Direct 3D powder printing of biphasic calcium phosphate scaffolds for substitution of complex bone defects. Biofabrication 6
50. Seitz H, Deisinger U, Leukers B, Detsch R, Ziegler G (2009) Different calcium phosphate granules for 3-D printing of bone tissue engineering scaffolds. Adv Eng Mater 11:B41–B46
51. Gbureck U, Hoelzel T, Biermann I, Barralet JE, Grover LM (2008) Preparation of tricalcium phosphate/calcium pyrophosphate structures via rapid prototyping. J Mater Sci Mater Med 19:1559–1563

52. Shanjani Y, De Croos JNA, Pilliar RM, Kandel RA, Toyserkani E (2010) Solid freeform fabrication and characterization of porous calcium polyphosphate structures for tissue engineering purposes. J Biomed Mater Res Part B Appl Biomater 93B:510–519
53. Detsch R, Schaefer S, Deisinger U, Ziegler G, Seitz H, Leukers B (2011) In vitro-osteoclastic activity studies on surfaces of 3D printed calcium phosphate scaffolds. J Biomater Appl 26:359–380
54. Tay BY, Evans JRG, Edirisinghe MJ (2003) Solid freeform fabrication of ceramics. Int Mater Rev 48:341–370
55. Mandal S, Meininger S, Gbureck U, Basu B (2018) 3D powder printed tetracalcium phosphate scaffold with phytic acid binder: fabrication, microstructure and in situ X-ray tomography analysis of compressive failure. J Mater Sci Mater Med 29
56. Vella JB, Trombetta RP, Hoffman MD, Inzana J, Awad H, Benoit DSW (2018) Three dimensional printed calcium phosphate and poly(caprolactone) composites with improved mechanical properties and preserved microstructure. J Biomed Mater Res Part A 106:663–672
57. Klammert U, Reuther T, Jahn C, Kraski B, Kubler AC, Gbureck U (2009) Cytocompatibility of brushite and monetite cell culture scaffolds made by three-dimensional powder printing. Acta Biomater 5:727–734
58. Habibovic P, Gbureck U, Doillon CJ, Bassett DC, van Blitterswijk CA, Barralet JE (2008) Osteoconduction and osteoinduction of low-temperature 3D printed bioceramic implants. Biomaterials 29:944–953
59. Fielding G, Bose S (2013) SiO_2 and ZnO dopants in three-dimensionally printed tricalcium phosphate bone tissue engineering scaffolds enhance osteogenesis and angiogenesis in vivo. Acta Biomater 9:9137–9148
60. Bose S, Banerjee D, Robertson S, Vahabzadeh S (2018) Enhanced in vivo bone and blood vessel formation by iron oxide and silica doped 3D printed tricalcium phosphate scaffolds. Ann Biomed Eng 46:1241–1253
61. Nandi SK, Fielding G, Banerjee D, Bandyopadhyay A, Bose S (2018) 3D-printed beta-TCP bone tissue engineering scaffolds: effects of chemistry on in vivo biological properties in a rabbit tibia model. J Mater Res 33:1939–1947
62. Torres J, Tamimi F, Alkhraisat MH, Prados-Frutos JC, Rastikerdar E, Gbureck U et al (2011) Vertical bone augmentation with 3D-synthetic monetite blocks in the rabbit calvaria. J Clin Periodontol 38:1147–1153
63. Castilho M, Dias M, Vorndran E, Gbureck U, Fernandes P, Pires I et al (2014) Application of a 3D printed customized implant for canine cruciate ligament treatment by tibial tuberosity advancement. Biofabrication 6
64. Arcos D, Vallet-Regi M (2013) Bioceramics for drug delivery. Acta Mater 61:890–911
65. Barralet J, Gbureck U, Habibovic P, Vorndran E, Gerard C, Doillon CJ (2009) Angiogenesis in calcium phosphate scaffolds by inorganic copper ion release. Tissue Eng Part A 15:1601–1609
66. Uchida A, Shinto Y, Araki N, Ono K (1992) Slow release of anticancer drugs from porous calcium hydroxyapatite ceramic. J Orthop Res 10:440–445
67. Sudo A, Hasegawa M, Fukuda A, Uchida A (2008) Treatment of infected hip arthroplasty with antibiotic-impregnated calcium hydroxyapatite. J Arthroplasty 23:145–150
68. Gbureck U, Vorndran E, Muller FA, Barralet JE (2007) Low temperature direct 3D printed bioceramics and biocomposites as drug release matrices. J Control Release 122:173–180
69. Cornelsen M, Petersen S, Dietsch K, Rudolph A, Schmitz K, Sternberg K et al (2013) Infiltration of 3D printed tricalciumphosphate scaffolds with biodegradable polymers and biomolecules for local drug delivery. Biomed Eng Biomedizinische Technik 58
70. Becker ST, Bolte H, Schuenemann K, Seitz H, Bara JJ, Beck-Broichsitter BE et al (2012) Endocultivation: the influence of delayed vs. simultaneous application of BMP-2 onto individually formed hydroxyapatite matrices for heterotopic bone induction. Int J Oral Maxillofac Surg 41:1153–1160
71. Strobel LA, Rath SN, Maier AK, Beier JP, Arkudas A, Greil P et al (2014) Induction of bone formation in biphasic calcium phosphate scaffolds by bone morphogenetic protein-2 and primary osteoblasts. J Tissue Eng Regen Med 8:176–185

72. Shende P, Agrawal S (2018) Integration of 3D printing with dosage forms: a new perspective for modern healthcare. Biomed Pharmacother 107:146–154
73. Sandler N, Maattanen A, Ihalainen P, Kronberg L, Meierjohann A, Viitala T et al (2011) Inkjet printing of drug substances and use of porous substrates-towards individualized dosing. J Pharm Sci 100:3386–3395
74. Wu BM, Borland SW, Giordano RA, Cima LG, Sachs EM, Cima MJ (1996) Solid free-form fabrication of drug delivery devices. J Control Release 40:77–87
75. Yu DG, Yang XL, Huang WD, Liu J, Wang YG, Xu H (2007) Tablets with material gradients fabricated by three-dimensional printing. J Pharm Sci 96:2446–2456
76. Wu W, Zheng Q, Guo X, Sun J, Liu Y (2009) A programmed release multi-drug implant fabricated by three-dimensional printing technology for bone tuberculosis therapy. Biomed Mater 4
77. Fuchs A (2013) MD thesis, University of Würzburg
78. Kanter B, Geffers M, Ignatius A, Gbureck U (2014) Control of in vivo mineral bone cement degradation. Acta Biomater 10:3279–3287

A Biomechanical Approach for Bone Regeneration Inside Scaffolds Embedded with BMP-2

C. Gorriz, F. Ribeiro, J. M. Guedes, J. Folgado and P. R. Fernandes

Abstract Scaffold-based strategies for Bone Tissue Engineering have been seen as a solution to repair bone in situations of large defect size and disease. Nevertheless, the factors that conduct to an optimal scaffold performance haven't been fully determined yet in spite of the intense research work on this field. This work presents the development of a computational model to analyse concurrently the process of degradation and the cell/tissue invasion in an artificial bone substitute embedded with BMP-2. The computational procedure comprises a degradation model which takes in account the hydrolysis process and its enhancement by autocatalysis and a mechano-regulated bone tissue regeneration model based on cell differentiation and growth theories including the effect of BMP-2. It assumes the domain of study to be only a representative volume element of a periodic scaffold constituted by several volume elements with periodic properties. The effective elastic and permeability properties are computed using an asymptotic homogenization method. Results show that the inclusion of BMP-2 in the scaffold leads to an increase on bone formation velocity. At the end of the process the quantity of bone is not significantly different with and without BMP-2, but an early bone formation contributes to a better mechanical stability of the bone substitute.

Keywords Bone scaffolds · Biodegradation · Bone regeneration · BMP-2 · Tissue Engineering

1 Introduction

The mechanism of bone regeneration, in normal condition, is a very efficient process. However, in situations of large defect size and disease it is necessary a surgical procedure. In fact, there are an estimated 2.2 million bone graft procedures performed annually to promote fracture healing or to fill defects [1]. The most common solu-

C. Gorriz · F. Ribeiro · J. M. Guedes · J. Folgado · P. R. Fernandes (✉)
IDMEC, Instituto Superior Técnico, Universidade de Lisboa, Lisbon, Portugal
e-mail: paulo.rui.fernandes@tecnico.ulisboa.pt

P. R. Fernandes and P. J. da Silva Bartolo (eds.), *New Developments in Tissue Engineering and Regeneration*, Computational Methods in Applied Sciences 51,
https://doi.org/10.1007/978-3-030-15372-4_5

tion is the use of autografts, though allografts and implantation of non-biological implants are also possible alternatives. These solution has some disadvantages such as bone limited supply, donor site morbidity, disease transmissions, host immune response, and, for implants, failure may occur after a certain time, due to the different mechanical properties of the material comparing with the original tissue [1]. The use of scaffold for Bone Tissue Engineering as bone substitutes is a promising alternative to previous solutions. These devices combine a three-dimensional structural porous matrix with cells and bioactive molecules to create an appropriate substitute that repairs the damaged tissue.

To obtain scaffolds with optimal performance, computational models for scaffold design has been developed [2–4], as well as models to simulate the scaffold degradation and the respective bone formation. Models to predict tissue regeneration inside scaffolds (degradation and bone formation) differ each other on the biodegradation model used [5–8] and on the bone formation approach [6–12]. These published works are essentially biomechanical, i.e., only the mechanical factors are considered as regulators for bone growth. However, the bone tissue regeneration strongly depends on the action of biochemical factors such as bone growth factors that stimulate the cellular chemotaxis, differentiation and proliferation [13]. In particular, the Bone Morphogenetic Protein 2 (BMP-2) is considered one of the most relevant signaling molecules for bone regeneration [14, 15]. Thus, scaffolds embedded with BMP-2 are also used to enhance bone formation [16], and so, a model able to predict the bone regeneration inside scaffolds embedded with BMP-2 would be a useful tool to assist on scaffolding design and development.

The main objective of this work is to propose a novel model to study the dynamic and interdependent process of degradation and the cell/tissue invasion in an artificial bone substitute taking in account the effect of BMP-2. This is accomplished through the development of a computational model combining a scaffold degradation model and a suitable bone tissue regeneration process. For this purpose the mechano-chemical model for bone healing recently published by Ribeiro et al. [17] is used. Results show that the inclusion of BMP-2 in the scaffold leads to an increase on bone formation velocity revealing the developed computational model as a useful tool to provide new insights on the design and behaviour of biodegradable scaffolds.

2 Materials and Methods

The computational model assumes the scaffold to be a porous periodic structure constituted by several volume elements with periodic properties, which allow us to study only a representative volume element of the scaffold. To compute the equivalent material properties of the scaffold an asymptotic homogenization method for periodic structures is used [18].

The computational model consists of a degradation model applicable to polymers with a mass degradation profile, comprising the hydrolysis process and its enhancement by autocatalysis [19] and a mechano-chemical regulated bone tissue

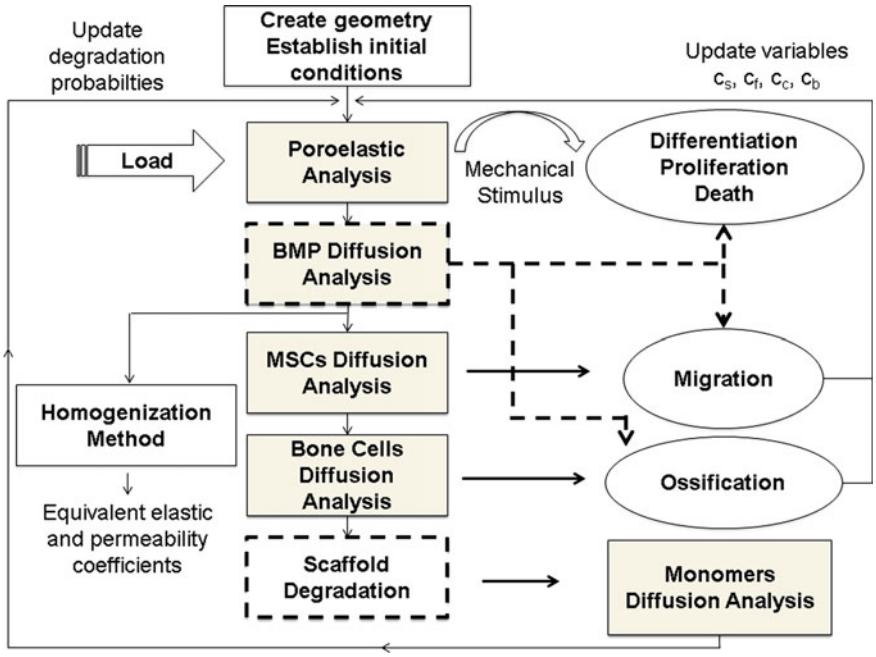

Fig. 1 Flowchart for the computational model to predict the bone formation inside the scaffold

regeneration model based on cell differentiation and growth theories [17] that is an extension of the model by Gómez-Benito and co-authors [20] in order to incorporate the effect of BMP-2. The flowchart for the model is presented in Fig. 1.

For a given initial geometry of the representative volume element a poroelastic analysis is performed to obtain the mechanical stimulus. Then diffusion analysis for BMP-2, mesenchymal cell (MCS) and bone cells are done. All this information allow us to determine the new concentrations for MSC (c_s), fibroblast (c_f), chondrocytes (c_c) and osteoblast (c_b) at each point of the scaffold and so the correspond tissue distribution. Finally, the new degradation stage is computed to complete the information about the material distribution inside the scaffold to restart the process. All the finite element analysis (poroelastic and diffusion) were performed using ABAQUS. The evolution of the properties of the tissue-polymer construct can be monitored at each instant (iteration) by computing the equivalent properties using homogenization methods.

2.1 Degradation Model

As mentioned above the model implemented here is an adaptation of the one described by Chen et al. [9]. For the domain of the representative volume element divided into a

finite number of elements, a state χ_H for every element is assigned: 1 for hydrolysable states, 0.001 for hydrolysed ones and 0 for the remaining void states. Then, for every hydrolysable element, a degradation probability is attributed according to Eq. (1),

$$P(\lambda, t) = \frac{\lambda_0 e^{-\lambda_0 t}[1 + \beta(e^{C_m} - 1)]}{V_0 V(t)} \tag{1}$$

where λ_0 is the degradation rate constant without autocatalytic effect, β is a constant to regulate the contribution of autocatalysis, C_m is the concentration of the monomers/by-products resultant from previous degradation, $V(t)$ is the volume fraction of polymer matrix at time t and V_0 is the initial volume fraction.

In every iteration, for every element with state, $\chi_H = 1$, a random generated number, r, is compared to that probability. If $P(\lambda, t) > r$, the element is hydrolysed and its state altered to $\chi_H = 0.001$.

C_m is a nodal variable increased when an element is degraded, by adding the mass of the degraded chains to all the adjacent nodes, n, of that element given by Eq. (2).

$$C^N_{m\,new} = C^N_m + \frac{\chi_H - \chi_h}{n} \tag{2}$$

The monomers motion through the scaffold is described by a diffusion equation, with attribution of different diffusivity constants during the degradation process, according to the element properties.

2.2 Bone Tissue Regeneration Model

The tissue regeneration model used in this work is based on cell differentiation and growth theories, where cellular process such as mitosis, migration, differentiation and apoptosis are mechano-regulated as proposed by Gómez-Benito et al. in 2005 for long bone healing [20] with the biochemical effect of BMP-2 modelled as proposed by Ribeiro et al. [17]. In this bone healing model the key parameters are the cell concentrations of: Mesenchymal Stem Cells (MSCs)—c_s; fibroblasts—c_f; chondrocytes—c_c; and osteoblasts—c_b.

These cell concentrations at a certain point within the scaffold evolves according to general balance equations defined for each cell type, function of proliferation, migration, differentiation and death rules [20]. Note that in this work this rules depend on both mechanical and chemical stimuli. The mechanical stimulus is the second invariant of the deviatoric strain tensor given by Eq. (3),

$$\psi = \sqrt{(\varepsilon_I - \varepsilon_{oct})^2 + (\varepsilon_{II} - \varepsilon_{oct})^2 + (\varepsilon_{III} - \varepsilon_{oct})^2} \tag{3}$$

where ε_I, ε_{II} and ε_{III} are the principal strains and ε_{oct} is octahedral strain defined as shown in Eq. (4).

$$\varepsilon_{oct} = \frac{1}{3}(\varepsilon_I + \varepsilon_{II} + \varepsilon_{III}) \tag{4}$$

The chemical stimulus is driven by the concentration of BMP-2 at each domain point. BMP-2 it is assumed to be encapsulated in the scaffold matrix and so, only after the degradation starts it is released. The concentration of BMP-2, obtained by a diffusion analysis, determines the fold value to be applied on the rules used to compute the cell concentrations. This is achieved using the theoretical curves defined by Ribeiro et al. [17] for MSC proliferation, MSC and bone cells chemotaxis, cartilage hypertrophy and bone tissue production.

Without being exhaustive in equation details that can be found in the referred works [17, 20] and in the Appendix, to illustrate the combined effect of the mechano-chemical stimulus let see the case of MSC. When the current concentration of MSC, c_s, is bellow an upper bound the new cell concentration is given by Eq. (5),

$$\frac{Dc_s}{Dt} = f_{prolif} + f_{mig} - f_{diff} - f_{death} \tag{5}$$

where f_{prolif} is the function that defines cell proliferation, f_{mig} is the function that defines cell migration, f_{diff} defines cell differentiation and f_{death} defines cell death. All this functions on the right hand side of Eq. (3) depend on the mechanical ψ ($\boldsymbol{x}$, t) at point $\boldsymbol{x}$ and instant t, and/or BMP-2 concentration. For instance f_{prolif} is given by Eq. (6),

$$f_{prolif} = \frac{\alpha_{prolif}\,\psi(\boldsymbol{x}, t)}{\psi(\boldsymbol{x}, t) + \psi_{prolif}}\,\phi(g) \tag{6}$$

where α_{prolif} and ψ_{proli} are constants, and $\phi(g)$ is the fold value obtained for the concentration g of BMP-2.

Sumarizing the cellular processes involved, chondrocytes and fibroblasts are produced from MSCs. Bone cells are also created from MSCs differentiation, but they may also be created as the result of cartilage calcification. Although cells are the key players on this process, the extracellular matrix (ECM) where cells are embedded are necessary to assess the physical properties of the regenerated tissues. Therefore each cell is considered to produce a specific ECM. This way, MSCs, chondrocytes, fibroblasts and bone cells originate granulation tissue, cartilage, fibrous tissue and bone tissue, respectively. Each volume of ECM is considered to be proportionally to the cell concentration responsible by its production (Eq. 7) where Q_i is the proportionality constant for the i type of cell and c_i is the respective concentration.

$$\frac{\partial V^i_{matrix}}{\partial t} = c_i \cdot Q_i \tag{7}$$

However, since the bone formation is influenced by the BMP-2 concentration, for the particular case of bone tissue this relation is written as in Eq. (8),

Table 1 Mechanical and permeability properties of the scaffold material and tissues

	PLGA	Granulation tissue	Bone tissue	Cartilage	Calcified cartilage	Fibrous tissue
E (MPa)	1200[11]	0.2[9]	982.489[10]	27.055[10]	57.055[10]	80.078[10]
ν	0.33[11]	0.167[9]	0.296[10]	0.104[10]	0.108[10]	0.128[10]
k ($\times 10^{-14}$ m^4/Ns)	0.001[9]	1[9]	0.001[9]	0.5[9]	0.5[9]	1[9]

$$\frac{\partial V^b_{matrix}}{\partial t} = c_b \cdot Q_b(g) \tag{8}$$

where the index b stands for bone and the proportionality constant $Q_b(g)$ depends on the BMP-2 concentration g and it is affected by the correspondent fold value.

The mechanical and permeability properties of the scaffold material, here considered to be 50:50 poly(lactic-co-glycolic acid) (PLGA), are presented in Table 1. When tissues are created, the nodal properties are the result of the combination of different tissues, so they are calculated using an average with the tissues volume fractions. The values used for each tissue are also presented in Table 1.

2.3 Material Properties by Homogenization

The model described above implies that at a certain instant we have in the defect region a construct of polymeric scaffold in degradation mixed with different biologic tissues. The assessment of the its properties during the healing time is useful to act in the scaffold design phase in order to optimize its perform. The asymptotic homogenization for periodic structures [18] is the method adopt here to determine the effective elastic and permeability properties of the system. The effective (homogenized) elastic properties are given by Eq. (9),

$$D^H_{ijkl} = \frac{1}{|Y|}\int_Y \left(E_{ijkl} - E_{ijpq}\frac{\partial \chi^{kl}_p}{\partial y_q}\right) dY \tag{9}$$

where $|Y|$ is the volume of the entire unit cell with the void and $\boldsymbol{\chi}^{kl}$ represents the characteristic deformations that result from six unit strains applied solely to the unit cell, and the homogenized permeability coefficients are given by Eq. (10),

$$K^H_{im} = \frac{1}{|Y|}\int_Y K_{ij}\left(\delta_{jm} - \frac{\partial \chi^m}{\partial y_j}\right) dY \tag{10}$$

where χ^m describes the microstructure pressure perturbations for a unit average pressure gradient in each direction m [21].

3 Results

3.1 Results for Scaffolds Without BMP-2

The model was computationally implemented in order to solve two and three dimensional problems [12]. To verify the model without the effect of BMP-2, 3D permeability maximized microstructures obtained by Dias et al. [3] through a topology optimization algorithm were used. Figure 2 show a representative volume element for a 35% porous scaffold where for Fig. 2a, b red is the polymer (PLGA).

The degradation profiles for this microstructure is shown in Fig. 3 for loads of 1 and 2 MPa. Experimental values from the works of Wu and Wang [22] and Oh et al. [23] are included in order to enable a comparison to assess the validity of the implemented degradation model. The evolution of tissues formation obtained for the same 35% porosity microstructure, are presented in Fig. 4.

On the first days, the main occurrences are the degradation of the polymer matrix and the proliferation and diffusion of the MSCs. Bone is the first tissue to be formed, appearing from the boundaries of the domain in regions located near the scaffold matrix. Around day 16, the areas surrounding the polymer matrix are under the influence of a mechanical stimulus that favors mainly the differentiation into chondrocytes and osteoblasts. About the same time, MSCs differentiation into fibroblasts occurs. Fibrous tissue formation is observed in areas of higher mechanical stimulus. From this point on, MSCs start migrating more profusely towards the inside of the polymer matrix as the number of voids is ever increasing. Due to the production of new tissues, that possess higher mechanical properties, the mechanical stability of the system is increased, further promoting the formation of bone in those locations. Around day 22/23, the bone cells, created mainly by intramembranous ossification, invade the matrix composed of calcified cartilage and replace it. After that, and until

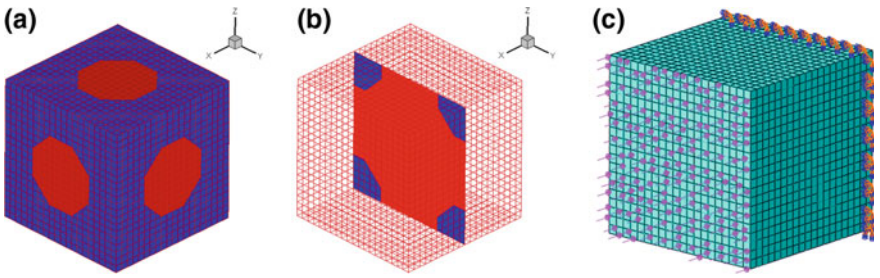

Fig. 2 **a** RVE for the tested scaffold. **b** Cross section. **c** Load boundary conditions

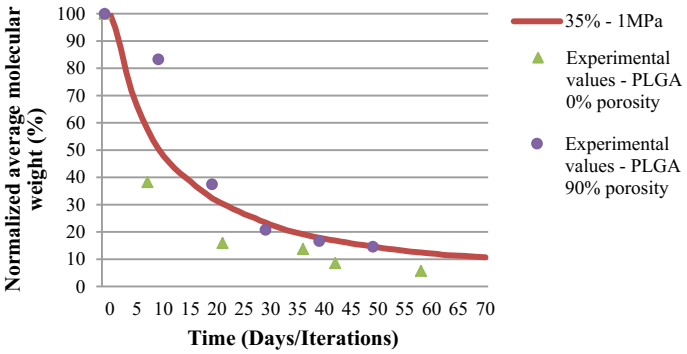

Fig. 3 Comparison between the simulation results and reported experimental results of normalized average molecular weight (%) as a function of time during biodegradation

day 50, bone tissue is created at a substantial velocity. Until the end of the simulation, bone continues to be formed but at a slower rate, filling a large part of the total domain.

Figure 5 displays the evolution of the effective normal (Cxx, Cyy, Czz) stiffness components of the stiffness tensor.

3.2 *BMP-2 Embedded Scaffolds. Comparison with Experimental Data*

To validate the developed computational model, the experimental study presented by Rahman et al. [24] was computationally reproduced. In the experimental study scaffolds made of 93.5% of poly(lactic-co-glycolic acid) and 6.5% of polyethylene glycol (PLGA/PEG), able to release BMP-2 by the degradation of the polymeric matrix were applied in rats calvaria. The scaffolds have a diameter of 4 mm and are 1 mm thick. In the computational simulation, a two dimensional model of a cross section was considered. Only half of the domain was analyzed due to axial symmetry. A BMP-2 dosage of 80 ng/mm^3 was considered. Results are presented in Figs. 6, 7 and 8.

3.3 *Results for Periodic Porous Scaffolds Embedded with BMP-2*

Here, for a sake of computational time reduction, two dimensional representation of idealized scaffolds were tested with the objective of assessing the performance of the developed computational model and analyse the rationality of using a mechano-

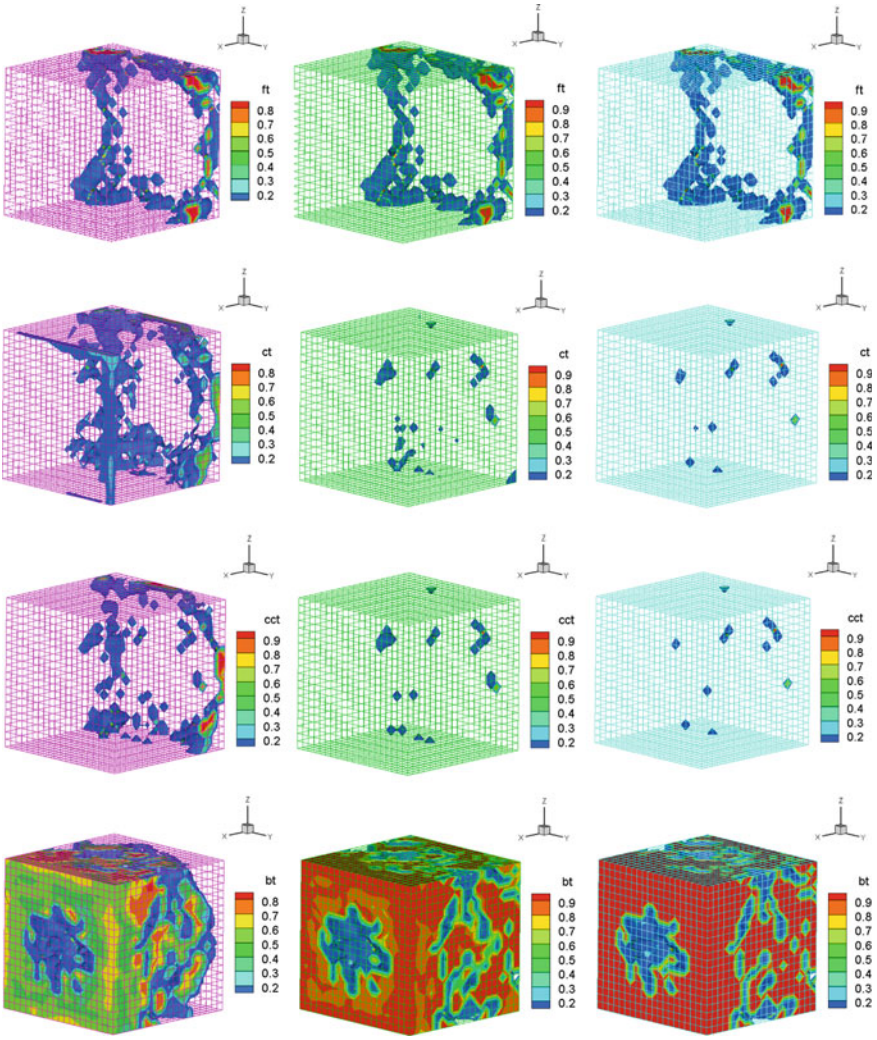

Fig. 4 Mechanobiological evolution of the scaffold-tissues system through time, for an applied load of 1 MPa. Left to right: day 20, 30 and 60. First row—fibrous tissue, second row—cartilage, third row—calcified cartilage, fourth row—bone tissue

chemical model considering the BMP-2 effect. The two dimensional geometries shown in Fig. 9 represent the cross sections of a unit cell of the idealized scaffolds. The unit cell is assumed to have 1 mm length. Figure 2a represent a scaffold with random distribution of material, Fig. 2b a laminate distribution of material and Fig. 2c a scaffold with longitudinal cylindrical struts.

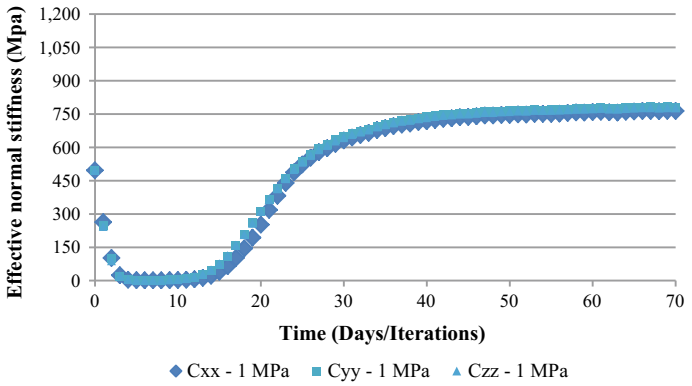

Fig. 5 Evolution of the effective normal stiffness

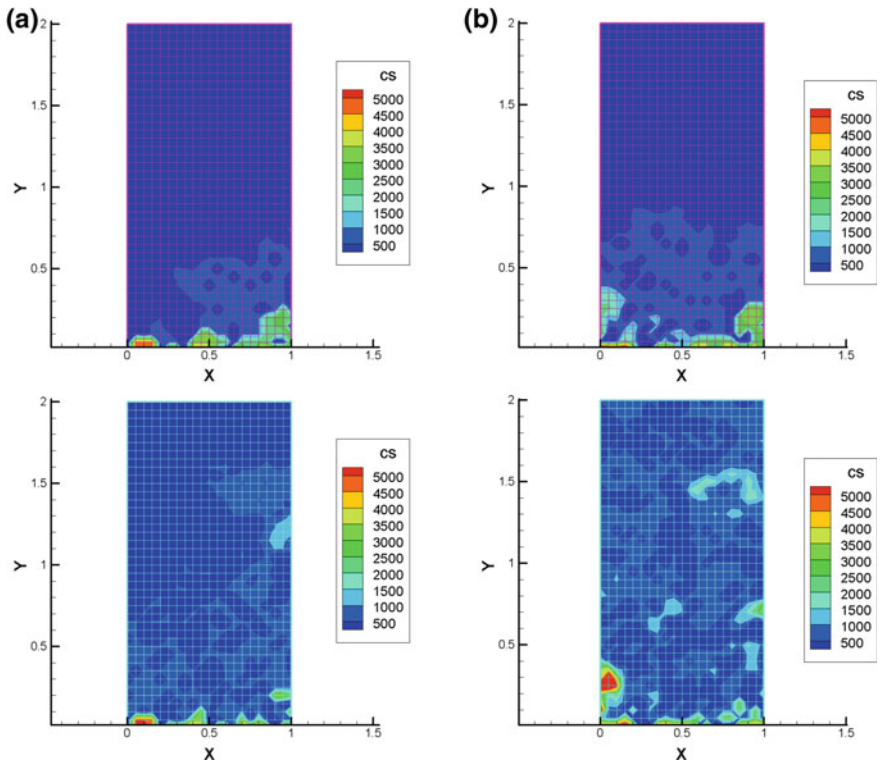

Fig. 6 MSCs concentration after 5 days (top) and after 10 days (bottom). **a** Without BMP-2. **b** With BMP-2

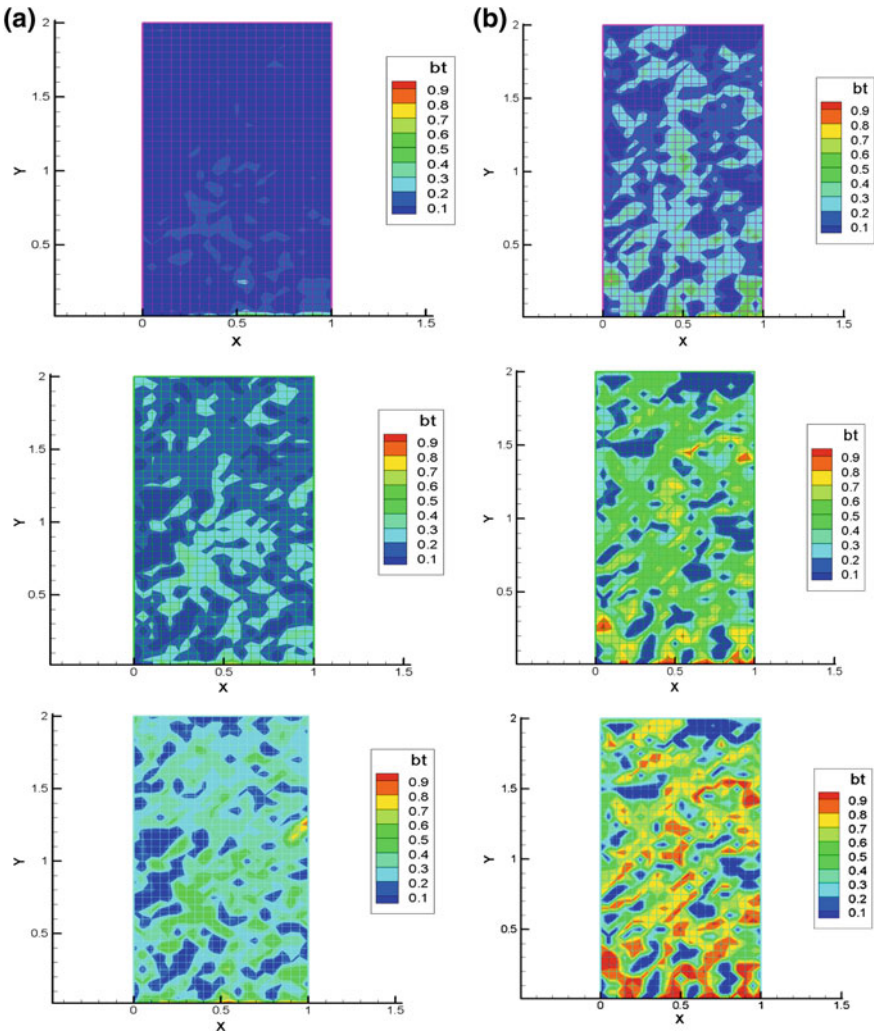

Fig. 7 Bone tissue after 20 days (top), 20 days (middle) and after 40 days (bottom). **a** Without BMP-2. **b** With BMP-2

Moreover, different dosages of BMP-2 were tested (30, 80 and 120 ng/mm^3). These values are in accordance with dosages used in in vivo studies of polymeric scaffolds [25].

Results of the percentage of bone formation for a period of two months for all models are presented in Fig. 10.

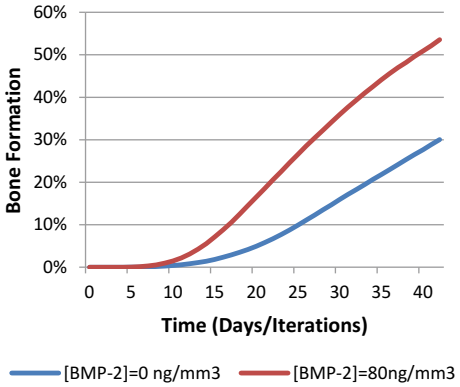

Fig. 8 Percentage of bone formation for a period of 6 weeks

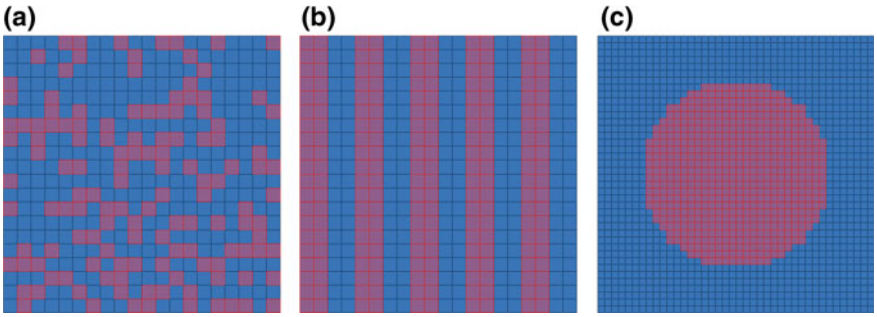

Fig. 9 Two dimensional models for RVE of idealized periodic scaffolds. The unit length is 1 mm. Red represents material and blue represents the porous region. **a** Random distribution, porosity 70%. **b** Laminate distribution, porosity 50%. **c** Longitudinal strut, porosity 65% (Color figure online)

4 Discussion

In this work a computational model for bone regeneration inside scaffolds embedded with BMP-2 was developed. The model combines a degradation model and a mechano-regulated bone tissue regeneration model based on cell differentiation and growth theories including the effect of BMP-2. The model was tested in three dimensional geometries of optimized scaffolds [3] and in idealized two dimensional geometries to assess the effect of BMP-2.

The degradation profiles for all simulations (2D and 3D) were very similar. The obtained values form a decreasing exponential over the degradation time, indicating a good agreement with what is expected in a bulk degradation, representing a simultaneous degradation on the surface and in the bulk of the material. On the last days, there is a small deceleration compared to what was expected. That could be

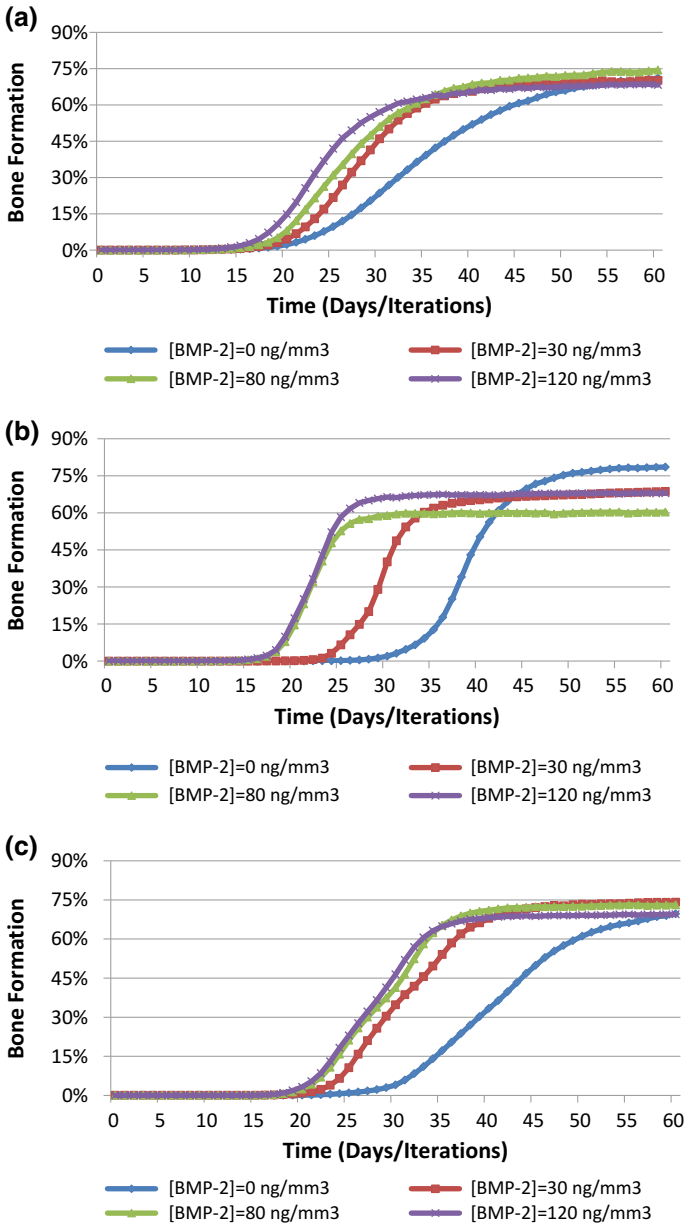

Fig. 10 Percentage of bone formation for a period of two months. **a** Scaffold with 70% porosity. **b** Scaffold with 50% porosity. **c** Scaffold with 65% porosity

interpreted as a need to perform a slight adjustment in the degradation rate constant or in autocatalysis factor.

The evolution of tissues formation for a 3D microstructure with 35% porosity microstructure and without BMP-2 was presented. When comparing the results concerning the percentage of tissue formation with the computational results obtained in [9] also for a permeability optimized microstructure an acceptable agreement is encountered. Moreover, the prediction of bone formation by Byrne et al. [26], for a 30% porous scaffold in similar conditions, is in accordance in terms of timing and magnitude with the current work results.

The curves in Fig. 5 for the evolution of the effective normal stiffness represent the decay of the mechanical properties of the system as the biomaterial is hydrolyzed, followed by an increase due to the contribution of the newly formed tissues. Due to the symmetry of the microarchitecture, the initial values are the same in every direction. As time goes by, due the randomness of the degradation model, the components start to deviate a little. Nevertheless, they remain somewhat close, specially the values referring to the mechanical properties in the y and z directions evidencing that the tissue regeneration occurs in an almost symmetrical manner, as a consequence of the symmetry of the initial microarchitecture. In Sanz-Herrera et al. [27], the evolution of the stiffness components of scaffold-tissues systems was also analyzed. The considered scaffolds were constituted by PCL, a polyester with a similar Young's modulus to that of PLGA. Simulations with three different scaffolds were performed, with ranging porosity values from 75 to 85% and with different pore distributions. There is a concordance regarding the shape of the evolution lines, especially with the more symmetric microarchitecture.

With respect to the analyses for scaffolds embedded with BMP-2, the model was first validated comparing the simulated results with an experimental setup presented by Rahman et al. [24]. Comparing Fig. 6a and b it is notorious the higher cells proliferation in early stages in presence of BMP-2. This higher concentrations of MSC will later potentiate the bone formation, since more cell are able to differentiate in osteoblasts. The combination of this effect with the capacity to attract bone cells due to chemical stimulus lead to a larger area of bone formation (Fig. 7). Together with an increase in bone formation, it results in a greater amount of bone over the whole domain. Results are also in agreement with the experimental ones [24]. The computational model gives a bone formation of nearly 54% for the simulation with BMP-2 after 6 weeks (Fig. 8), which is very close to the experimental value of 55%. Furthermore, the results also agree with respect to the increase in bone formation due to the growth factor comparing with the control (without BMP-2). The computational result present an increase of 23.5%, while in the experimental model this value is 24% after 6 weeks.

Analyzing the results for the two-dimensional periodic scaffolds with BMP-2, it confirms that the addition of BMP-2 increases the rate of bone formation comparing with the bone formation in scaffolds without the growth factor. Moreover, there are a correlation between the BMP-2 dosage and the bone formation. In fact an increase in the dosage correspond to a bigger amount of bone tissues for the initial and intermediate stages, as already observed in Ribeiro et al. [17]. This result is in

agreement with experimental results where a higher BMP-2 dosages correspond to bigger area, volume and density of bone [25]. With respect to the final quantity of bone, there are no difference between scaffolds with and without BMP-2. However, the higher bone formation in earlier stages is advantageous because it balances the loss of stiffness due to the scaffold degradation, which is very common with polymeric scaffolds [28].

Notwithstanding some limitations of the model such as the simulation of a single representative volume element or the no consideration of the vascularization effect, the presented work represents a useful tool to simulate the in vivo behaviour of biodegradable scaffolds and so, to contribute to bone scaffold development.

Acknowledgements Authors would like to tank to Fundação para a Ciência e Tecnologia (Portugal) for the support through project PTDC/BBB-BMC/5655/2014 and LAETA project UID/EMS/50022/2019.

Appendix

This appendix summarize the evolution equations for the bone regeneration model. Basically it is an adaptation to bone regeneration inside the scaffold of the model presented by Gomez-Benito et al. [20] and modified by Ribeiro et al. [17] to introduce the BMP-2 effect.

Mesenchymal Stem Cells (MSC)

The concentration of MSC can vary according to Eq. 11 due to proliferation, migration, differentiation and cell death,

$$\frac{Dc_s}{Dt} = \begin{cases} f_{prolif} + f_{mig} - f_{diff} - f_{death} & \text{if} \quad c_s < c_s \max \\ f_{mig} - f_{diff} - f_{death} & \text{if} \quad c_s = c_s \max \end{cases} \tag{11}$$

where f_{prolif} is the function that defines cell proliferation, f_{mig} is the function that defines cell migration, f_{diff} defines cell differentiation and f_{death} defines cell death. The mechanical stimulus $\psi\ (\boldsymbol{x}, t)$ at point $\boldsymbol{x}$ and instant t is the second invariant of the deviatoric strain tensor given by Eq. (12),

$$\psi = \sqrt{(\varepsilon_I - \varepsilon_{oct})^2 + (\varepsilon_{II} - \varepsilon_{oct})^2 + (\varepsilon_{III} - \varepsilon_{oct})^2} \tag{12}$$

with ε_I, ε_{II} and ε_{III} the principal strains and ε_{oct} the octahedral strain defined as shown in Eq. (13).

$$\varepsilon_{oct} = \frac{1}{3}(\varepsilon_I + \varepsilon_{II} + \varepsilon_{III}) \tag{13}$$

The f_{prolif} is given by Eq. (14),

$$f_{prolif} = \frac{\alpha_{prolif}\,\psi(\boldsymbol{x}, t)}{\psi(\boldsymbol{x}, t) + \psi_{prolif}}\,\phi(g) \tag{14}$$

where α_{prolif} and ψ_{prolif} are constants, and $\phi(g)$ is the fold value obtained for the concentration g of BMP-2 reflecting the chemical stimulus introduced in this approach. Once the concentration of BMP-2 is known the fold value to be applied is determined by the theoretical curves defined in Ribeiro et al. [17].

The f_{mig} is given by Eq. (15),

$$f_{mig} = -D_0 \nabla^2 c_s + D_g \nabla^2 g \tag{15}$$

where D_0 is the diffusion coefficient for MSCs and the second term of Eq. (15) represents the effect of BMP-2 on MSC chemotaxis with D_g being the respective diffusion coefficient.

The differentiation behaviour, f_{diff}, is defined by Eq. (16).

$$f_{diff} = \begin{cases} h_{intramembranous}(\psi, t) & \text{if} \quad \psi_{\lim} < \psi < \psi_{bone} \quad \text{and} \quad t > t_m^b \\ g_{diff}(\psi, t) & \text{if} \quad \psi_{bone} < \psi < \psi_{cartilage} \quad \text{and} \quad t > t_m^c \\ l_{diff}(\psi, t) & \text{if} \quad \psi_{cartilage} < \psi < \psi_{fibrous} \quad \text{and} \quad t > t_m^f \end{cases} \tag{16}$$

This means that MSCs can differentiate into bone cell ($h_{intramembranous}$), chondrocytes (g_{diff}), or into fibroblasts (l_{diff}) depending on the mechanical stimulus value and time.

The time limits are defining for each differentiation path as follows,

$$t_m^b = t_{m\_lim}^c \cdot \frac{\psi}{\psi_{bone}} \tag{17a}$$

$$t_m^c = t_{m\_lim}^c \tag{17b}$$

$$t_m^f = \begin{cases} \frac{\psi - \psi_{slope}}{\psi_{cartilage} - \psi_{slope}} t_{m\_lim}^{slope} + t_{m\_lim}^c \\ t_{m\_lim}^c \end{cases} \tag{17c}$$

where $t_{m\_lim}^c$, $t_{m\_lim}^{slope}$, ψ_{slope}, ψ_{bone} and $\psi_{cartilage}$ are constants.

Each differentiation function on the right hand side of Eq. (16) is defined differently. So the differentiation in bone cells is ruled by Eq. (18).

$$h_{intramembranous} = \begin{cases} D_b \nabla^2 c_b + D_g \nabla^2 g \;, & \psi_{lim} < \psi < \psi_{bone} \;\text{ and }\; t > t_m^b \;\text{ and }\; c_b < c_b^{\min} \\ c_s \;, & \psi_{lim} < \psi < \psi_{bone} \;\text{ and }\; t > t_m^b \;\text{ and }\; c_b > c_b^{\min} \end{cases} \tag{18}$$

Here, the effect of BMP-2 is again taking into account, increasing the cell differentiation when the limit of bone cell is below the threshold value that make all MSCs to differentiate in bone cells. In fact when the number of bone cell is small the differentiation occurs gradually ensuring that intramembranous ossification could only occur next to already existing bone [20].

The differentiation of MSCs into chondrocytes and fibroblasts is given by Eqs. (19) and (20), respectively.

$$g_{diff} = c_s \tag{19}$$

$$l_{diff} = c_s \tag{20}$$

For very high mechanical stimulus, cells die and so the MSCs death is defined as,

$$f_{death} = c_s \quad \text{if} \quad \psi_{death} < \psi \tag{21}$$

Chondrocytes

The concentration of chondrocytes is given by Eq. (22),

$$\frac{Dc_c}{Dt} = g_{diff}(\psi, t) - h_{endochondral}(\psi, t) \tag{22}$$

where g_{diff} is the function described by Eq. 19 and $h_{endochondral}$ is the number of chondrocytes replaced by bone cells during endochondral ossification.

The differentiation of chondrocytes in bone cell is given by Eq. (23),

$$h_{endochondral} = \begin{cases} D(\psi)\nabla^2 c_b & \text{if } \psi < \psi_{bone}, \quad p_{mi} > p_{mi\_\min} \quad \text{and} \quad c_b < c_b^{\min} \\ c_s & \text{if } \psi < \psi_{bone}, \quad p_{mi} > p_{mi\_\min} \quad \text{and} \quad c_b > c_b^{\min} \end{cases} \tag{23}$$

where the first parcel of Eq. (23) describes the gradual advancement of an endochondral ossification front which invades the mineralized cartilage (p_{mi_min}), if the number of bone cells is not enough to promote the differentiation of all chondrocytes cell. Importantly, the referred diffusion coefficient (ψ) is considered to be dependent on the mechanical stimulus and is described in Eq. (24),

$$D(\psi) = D_b \frac{\psi_{bone} - \psi}{2\ \psi_{bone}} \tag{24}$$

where D_b and ψ_{bone} are constants.

Fibroblasts

The fibroblast only appeared from MSCs differentiation (Eq. 25),

$$\frac{D c_f}{D t} = l_{diff} \tag{25}$$

where l_{diff} is given by Eq. (20).

Bone Cells

The concentration of bone cell is given by Eq. (26),

$$\frac{D c_b}{D t} = h_{\text{intramembranous}}(\psi, t) + h_{endochondral}(\psi, t) \tag{26}$$

with $h_{intramembranous}$ and $h_{endochondral}$ already defined above (Eqs. 18 and 23, respectively).

ECM Production and Replacement

Although this the model is essential based on cells, the tissues where cells are embedded are necessary to evaluate the mechanical behaviour. Thus, each cell is considered to produce a specific extracellular matrix (ECM).

MSCs is associated to granulation tissue, chondrocytes to cartilage, fibroblasts to fibrous tissue and bone cells to bone tissue. Each ECM is considered to be proportionally to the cell concentration responsible by its production (Eq. 27) where Q_i is the proportionality constant for the i type of cell and c_i is the respective concentration.

$$\frac{\partial V^i_{matrix}}{\partial t} = c_i \cdot Q_i \tag{27}$$

Because bone formation is influenced by the BMP-2 the concentration for the particular case of bone tissue is given by Eq. (28),

$$\frac{\partial V^b_{matrix}}{\partial t} = c_b \cdot Q_b(g) \tag{28}$$

where the index b stands for bone and the proportionality constant $Q_b(g)$ depends on the BMP-2 concentration g and it is affected by the correspondent fold value.

References

1. Fu Q, Saiz E, Rahaman MN, Tomsia AP (2011) Bioactive glass scaffolds for bone tissue engineering: state of the art and future perspectives. Mater Sci Eng C 31(7):1245–1256
2. Hollister SJ, Lin CY (2007) Computational design of tissue engineering scaffold. Comput Methods Appl Mech Eng 196:31–32
3. Dias MR, Guedes JM, Flanagan CL, Hollister SJ, Fernandes PR (2014) Optimization of scaffold design for bone tissue engineering: a computational and experimental study. Med Eng Phys 36(4):448–457
4. Castilho M, Dias M, Gbureck U, Groll J, Fernandes P, Pires I, Gouveia B, Rodrigues J, Vorndran E (2013) Fabrication of computationally designed scaffolds by low temperature 3D printing. Biofabrication 5:035012
5. Chao G, Xiaobo S, Chenglin C, Yinsheng D, Yuepu P, Pinghua L (2009) A cellular automaton simulation of the degradation of porous polylactide scaffold: I. Effect of porosity. Mater Sci Eng C 29(6):1950–1958
6. Göpferich A, Langer R (1993) Modeling of polymer erosion. Macromolecules 26(16):4105–4112
7. Göpferich A (1997) Polymer bulk erosion. Macromolecules 30(9):2598–2604
8. Mohammadi Y, Jabbari E (2006) Monte Carlo simulation of degradation of porous poly (lactide) scaffolds, 1. Macromol Theory Simul 15(9):643–653
9. Chen Y, Zhou S, Li Q (2011) Mathematical modeling of degradation for bulkerosive polymers: applications in tissue engineering scaffolds and drug delivery systems. Acta Biomater 7(3):1140–1149
10. Sanz-Herrera J, Garcia-Aznar J, Doblare M (2007) A mathematical approach for tissue regeneration inside a specific type of scaffold. Biomech Model Mechanobiol 7:355–366
11. Adachi T, Osako Y, Tanaka M, Hojo M, Hollister SJ (2006) Framework for optimal design of porous scaffold microstructure by computational simulation of bone regeneration. Biomaterials 27:3964–3972
12. Gorriz C, Ribeiro F, Guedes JM, Fernandes PR (2015) A biomechanical approach for bone regeneration inside scaffolds. Procedia Eng 110:82–89
13. Schindeler A, McDonald MM, Bokko P, Little DG (2008) Bone remodeling during fracture repair: the cellular picture. Semin Cell Dev Biol 19(5):459–466
14. Gerhart TN, Kirker-Head CA, Kriz MJ, Holtrop ME, Hennig GE, Hipp J, Schelling SH, Wang E (1993) Healing segmental femoral defects in sheep using recombinant human bone morphogenetic protein. Clin Orthop Relat Res 293:317–326
15. Boyne P, Marx RE, Nevins M, Lazaro E, Le Lilly AM, Nummikoski P (1997) A feasibility study evaluating rhbmp-2/absorbable collagen sponge for maxillary sinus floor augmentation. Int J Period Restor Dent 17:11–25
16. Wang X, Nyman JS, Dong X, Leng H, Reyes M (2010) Fundamental biomechanics in bone tissue engineering. Synth Lect Tissue Eng 2(1):1–225
17. Ribeiro FO, Gomez-Benito MJ, Folgado J, Fernandes PR, Garcia-Aznar JM (2015) In silico mechano-chemical model of bone healing for regeneration of critical defects: the effect of BMP-2. PLoS ONE 10(6):e0127722
18. Guedes JM, Kikuchi N (1990) Preprocessing and postprocessing for materials based on the homogenization method with adaptive finite element methods. Comput Methods Appl Mech Eng 83:143–198
19. Chen Y, Zhou S, Li Q (2011) Mathematical modeling of degradation for bulk-erosive polymers: applications in tissue engineering scaffolds and drug delivery systems. Acta Biomater 7(3):1140–1149
20. Gómez-Benito MJ, García-Aznar JM, Kuiper JH, Doblaré M (2005) Influence of fracture gap size on the pattern of long bone healing: a computational study. J Theor Biol 235(1):105–119
21. Dias MR, Fernandes PR, Guedes JM, Hollister SJ (2012) Permeability analysis of scaffolds for bone tissue engineering. J Biomech 45(6):938–944

22. Wu XS, Wang N (2001) Synthesis, characterization, biodegradation, and drug delivery application of biodegradable lactic/glycolic acid polymers. Part II: Biodegradation. J Biomater Sci Polym Ed 12(1):21–34
23. Oh SH, Kang SG, Lee JH (2006) Degradation behavior of hydrophilized PLGA scaffolds prepared by melt-molding particulate-leaching method: comparison with control hydrophobic one. J Mater Sci Mater Med 17(2):131–137
24. Rahman CV, Ben-David D, Dhillon A, Kuhn G, Gould TW, Müller R, Rose FR, Shakesheff KM, Livne E (2014) Controlled release of BMP-2 from a sintered polymer scaffold enhances bone repair in a mouse calvarial defect model. J Tissue Eng Regen Med 8(1):59–66
25. Cowan CM, Aghaloo T, Chou YF, Walder B, Zhang X, Soo C, Wu B (2007) MicroCT evaluation of three-dimensional mineralization in response to BMP-2 doses in vitro and in critical sized rat calvarial defects. Tissue Eng 13(3):501–512
26. Byrne DP, Lacroix D, Planell JA, Kelly DJ, Prendergast PJ (2007) Simulation of tissue differentiation in a scaffold as a function of porosity, young's modulus and dissolution rate: application of mechanobiological models in tissue engineering. Biomaterials 28(36):5544–5554
27. Sanz-Herrera J, Doblaré M, GarcíaAznar J (2010) Scaffold microarchitecture determines internal bone directional growth structure: a numerical study. J Biomech 43(13):2480–2486
28. Schofer MD, Roessler PP, Schaefer J, Theisen C, Schlimme S, Heverhagen JT, Paletta JR (2011) Electrospun PLLA nanofiber scaffolds and their use in combination with BMP-2 for reconstruction of bone defects. PLoS ONE 6(9):e25462